STUDY OF PARTICLE MULTIPLICITY AND RESONANCE PRODUCTION AT RHIC

A THESIS SUBMITTED TO THE

UTKAL UNIVERSITY

FOR THE DEGREE OF

DOCTOR OF PHILOSOPHY IN SCIENCE

(PHYSICS)

AUGUST, 2005

By

DIPAK KUMAR MISHRA

INSTITUTE OF PHYSICS, BHUBANESWAR 751 005, INDIA

CERTIFICATE

This is to certify that the thesis entitled **" Study of particle multiplicity and resonance production at RHIC"** which is being submitted by **Mr. DIPAK KUMAR MISHRA** towards partial fulfillment for the degree of **Doctor of Philosophy in Science (Physics) of Utkal University, Bhubaneswar** is a record of his own research work carried out by him. He has carried out his investigations for the last five years on the subject matter of the thesis under my guidance at the **Institute of Physics, Bhubaneswar**. To the best of my knowledge, the matter embodied in the thesis has not been submitted for the award of any other degree by him or by anybody else.

Prof. D. P. Mahapatra
Institute of Physics
Bhubaneswar

Acknowledgments

It is my pleasure to thank many people who made this thesis possible. This thesis would not have beeen possible without the support, encouragement, advice and friendship of many people.

First, I express my deep sense of gratitude to my thesis supervisor Prof. D. P. Mahapatra for his continuous guidance, inspiration and his constant support throughout my research period at the institute. His constructive criticisms at every stage during my thesis work guided me to have a better understanding of the subject.

I would like to express my sincere thanks to Dr. Y. P. Viyogi, for his constant support, advice and useful suggestions whenever approached. I am especially thankful to him for his patient replies of my queries. I also thank to Prof. S. C. Phatak for his kind support, encouragement and many useful discussions.

My sincere thank to Dr.Tapan K. Nayak for his support and encouragement throughout my research period. It is a unique experience in working with him during data taking time at BNL. His never-say-die attitude gives lots of encouragement during my thesis work. I would like to thank to Dr. Subhasis Chattopadhyay for his invaluable help, advice and encouragement during my research period. I have learned many things especially the STAR software from him, which helped quite a lot in STAR data analysis.

I would like to thank to Dr. Bedangdas Mohanty for his help and encouragement starting from the first day of my research career till the end of my Ph.D. thesis. It is my pleasure that I have spent quite a bit of time and learned many things from

him. It was a great learning experience to work with him. I also must thank to Dr. P.K. Sahu for his kind support and many useful discussions.

I also would like to thank to Dr. Zhangbu Xu for his help and encouragement for getting into my thesis work. I also express my sincere thank to Dr. Haibin Zhang for his invaluable help and his patient replies to many of my queries. He guided me through the detailed analysis in my research work. It is a unique experience to work with him. He is not only my collaborator but also my good friend.

I would also like to thank Mr. G. S. N. Murthy- our detector man, Mr. R. N. Singaraju - our "electronics expert", Mr. Sushant Pal- our "DAQ expert" for the useful discussion with them in their respective fields, especially during the installation and data taking time at BNL. My sincere thank to Dr. B. K. Nandi, Dr. S. K. Nayak, Dr. G. C. Mishra, Dr. Zubayer Ahmed, Dr. Premomoy Ghosh. I thank them all for sharing their knowledge and experiences.

I express my hearty thanks to my collaborators and scholar friends Dr. Anand K. Dubey and Mr. Raghunath Sahoo at the institute. It was a great experiences in sharing the happy moment with them both in academic and non-academic. I would also like to thank to Ms. Sadhana Dash for her support, help and encouragement. I enjoyed the time spent in company of these people.

It also has been a nice experience working with many scholar friends in the collaboration, Mr. Supriya Das and Mr. Debasis Das and Pawan Kumar of VECC, Mr. Ajay Thakur, Ms. Monika Sharma of Panjab University, Mr. Sudhir Bhardwaj and Pawan of Rajsthan University, Dr. Taseen Saha, Ms. Ramni Gupta, Mr. Sunil Dogra, Ms. Anita Sharma of Jammu University, I thank them all for their help and cooperation.

It is a pleasure to thank my collaborators at VECC, Mr. M. R. Dutta Mazumdar, Mr. Partho Ghosh and Mr. M. D. Trivedi. I have also gained from my collaborators from other institutes and would like to thank Dr. M. M. Aggarwal and Dr. A. K. Bhati, from Panjab University, Chandigarh, Dr. L. K. Mangotra, Dr. S. K. Badyal, Dr. Anju Bhasin, Dr. P. V. K. S. Baba and Mr. Anik Gupta, of Jammu University, Jammu,

Dr. R. Raniwala and Dr. S. Raniwala, of Rajsthan university, Jaipur. I thank them all for their help and encouragement.

I would like to express my sincere thanks and gratitude to Dr. Patricia Fachini and Dr. An Tai and Dr. Ruan Lijuan for their help and useful discussions.
I would like to thank to Dr. R. K. Choudhury, Director of IOP for his help and support during my research career. I take this opportunity to thank all the faculty of this institute particularly, my predoctoral teachers from whom I have gained immensely. I would also like to thank all my college and school teachers who taught me, especially my school teachers Mr. Pradip K. Pradhan and Mr. Biswanath Pradhan, who encouraged me to pursue research.

I would like to thank my seniors, scholar friends and others, they include, Prasanta bhai, Kamila bhai, Sandip dada, Rajarshi da, Debasis da, Soma, Venkatesh, Kamal bhai, Zashmir bhai, Jhasa bhai, Dipak da, Anindya, Biswarup, Biswanath, Satchi, Chandra, Colin, Satyabrata, Milind, Rashmi nani, Sanjukta, Hara, Sinu, Kuntala, Sambhu, Rajeev, Bharat, Soumen, Niraj, Tanay, Sumalaya, Amulya, Prabir, Manas, Jay, Prabodh, Dipakpk, Anupam, Umanand, Srikumar, Somanath, Gayatri, Binata, Sunil, Jim, Nabyendu, Sobin. Special thanks to Ananta, Ajay and Mamata for spending their valuable time with me at the time of loneliness. I must thank to Boby for going through my thesis draft and helping me in correction. I thank them all for their help and goodwill for the many moments of fun and togetherness during the festivals, picnics etc. They have made my stay in the beautiful campus of IOP a memorable and pleasing one.

I am also thankful to all the library, administrative, laboratory and computer centre staff of this institute for their kind and prompt support at every stage. I also thank the hostel mess staff for providing excellent food during my stay in the hostel.

Lastly, but most importantly, I express my due respects and thanks to my parents

for their immense patience and encouragement. I am indebted to them for giving me the freedom to choose my career and for constantly providing me the much needed moral and emotional support at every stage. It is only because of their love, affection and blessings that I could complete this thesis.

Date: **Dipak Kumar Mishra**

Contents

CERTIFICATE **ii**

Acknowledgments **iii**

1 The Physics of Relativistic Heavy Ion Collisions **11**

1.1 Introduction 11

1.1.1 Deconfinement and Phase Diagram 11

1.1.2 Chemical and Kinetic Freeze-out 14

1.2 Estimation of Initial Energy Density in High-Energy Nucleus-Nucleus Collisions 16

1.3 Relativistic Heavy Ion Physics Programs: past, present and future . . 18

1.4 Some Suggested Signatures of QCD Phase Transition 21

1.4.1 Thermodynamic Variables 22

1.4.2 Flow 24

1.4.3 Strangeness Enhancement 26

1.4.4 Thermal Photons and Dileptons 26

1.4.5 J/Ψ suppression 29

1.4.6 Jet Quenching 31

1.4.7 Resonances and Their In-Medium Effects in Hot and Dense Matter 33

1.4.8 Rescattering and Regeneration Effect 33

1.4.9 Measuring the Time Scale between Chemical and Kinetic Freeze-outs . . . 34
1.5 Event Generator: (HIJING) . . . 35
1.6 Thesis Organization . . . 36

2 The STAR Experiment **38**
2.1 The RHIC Accelerator Complex . . . 38
2.1.1 The Detectors at RHIC . . . 39
2.2 The STAR Experiment . . . 41
2.2.1 The Time Projection Chamber (TPC) . . . 45
2.2.2 Trigger Detectors . . . 47
2.2.3 Forward Time Projection Chamber (FTPC) . . . 49
2.2.4 Silicon Vertex Tracker (SVT) . . . 50
2.2.5 Silicon Strip Detector (SSD) . . . 51
2.2.6 Time Of Flight (TOF) . . . 51
2.2.7 Forward Pion Detector (FPD) . . . 52
2.2.8 Beam Beam Counter (BBC) . . . 53
2.2.9 Barrel Electromagnetic Calorimeter (BEMC) . . . 54
2.2.10 Endcap Electromagnetic Calorimeter (EEMC) . . . 55
2.2.11 Photon Multiplicity Detector (PMD) . . . 57
2.2.12 Particle Identification (PID) using dE/dx . . . 58
2.2.13 Centrality and trigger conditions . . . 60

3 The Photon Multiplicity Detector (PMD) **61**
3.1 Introduction . . . 61
3.2 Physics goals . . . 61
3.3 Photon Detection in a preshower PMD . . . 62
3.3.1 Preshower Part . . . 63
3.3.2 Charge Particle Veto Part . . . 64
3.4 STAR Photon Multiplicity Detector . . . 64

3.4.1 Mechanical Description 65
3.4.2 Honeycomb Chambers 66
3.4.3 Assembly of Supermodule 71
3.4.4 Support Structure and Converter Plates 73
3.5 Front-End Electronics (FEE) 74
3.6 Readout for PMD 75
3.6.1 Pre-trigger and Timing Diagram of the PMD 75
3.6.2 C-RAMS Scheme 76
3.7 Gas Flow Control for PMD 77
3.8 Some Physical Parameters of PMD 79
3.8.1 Converter Thickness and Cell Size 79
3.8.2 Acceptance 79
3.8.3 Photon Conversion Efficiency 80
3.8.4 Test Results/ Performance of the PMD 82
3.9 Clustering in PMD and Finding Photon Hits 85
3.10 Procedure For Generating Simulated Data 88
3.10.1 PMD in GSTAR and Big Full Chain (BFC) 89
3.10.2 Occupancy and Multihit Probability 91
3.10.3 Effect of Upstream Material on Photons 92
3.10.4 Photon counting 93

4 The $\Delta(1232)$ and $K^*(892)$ Resonance Production in d+Au Collisions 99
4.1 Introduction 99
4.2 Analysis Methods 100
4.2.1 Trigger 100
4.2.2 Centrality Selection 101
4.2.3 Track Selection 101
4.2.4 Constructing the $\Delta(1232)$ and $K^*(892)$ Signal 103
4.3 Residual Background 107

4.3.1 Elliptic Flow Effect . . . 107
4.3.2 Correlated Real Pairs . . . 108
4.3.3 Mis-identified Pairs . . . 108
4.4 Invariant Yield, Mass and Width Determination for Δ and K^* . . . 109
4.4.1 Fitting Function used for $\Delta^{++}(1232)$ . . . 109
4.4.2 Fitting Function Used For $K^*(892)$ . . . 112
4.5 Efficiency Correction . . . 116
4.5.1 Correction for Branching Ratio . . . 118
4.6 Transverse momentum spectra for $\Delta(1232)$ and $K^*(892)$ in d+Au Collisions . . . 123
4.7 Mass and Width Distribution for Δ and K^* . . . 142
4.8 $\langle p_T \rangle$ Distributions of Δ and K^* . . . 146
4.9 Systematic Uncertainties for Yield and Inverse Slope Parameter (or $\langle p_T \rangle$) for Δ and K^* . . . 149
4.9.1 Fit Functions . . . 150
4.9.2 Residual Background Functions . . . 150
4.9.3 Dynamical Cut Effects . . . 151
4.9.4 Track Types . . . 152
4.9.5 Detector Effects . . . 152
4.9.6 Different Freeze-out Parameter . . . 153
4.9.7 Fit Function Used to Fit the p_T Spectra . . . 154
4.9.8 Total Systematic Errors . . . 155
4.10 Particle Ratios . . . 155
4.11 Nuclear Modification Factor . . . 157

5 Conclusion **160**

List of Figures

1.1 Phase diagram of hadronic and partonic matter, showing hadron gas and quark gluon plasma regions. The temperature T and the baryochemical potential μ_B data are derived from the particle yield ratios. The solid curve through the data points represents the chemical freeze-out of hadronic matter. This figure is taken from [5]. 12

1.2 Space-time diagram of longitudinal evolution of the quark-gluon plasma. 14

1.3 (a) The configuration of two nuclei A and B before collision. (b) The configuration after collision with energy deposited in the region around $z \sim 0$. 16

1.4 $v_2(p_T)$ for minimum-bias events (circles) for Au+Au collisions at $\sqrt{s_{NN}}$ = 200 GeV. The error bars represent the statistical error and the caps show the systematic uncertainty. The data are compared with hydro-pQCD calculations [20] assuming the initial gluon density dN^g/dy = 1000 (dashed line), 500 (dotted line, and 200 (dashed-dotted line). Also shown as pure hydrodynamical calculations [21] (solid line). This figure has been taken from [17]. 25

1.5 Mid-rapidity K/π ratios versus $\sqrt{s_{NN}}$. The error bars show the statistical errors. The systematic errors are on the STAR data are indicated by caps. This figure has been taken from [25]. 27

1.6 The invariant direct-photon multiplicity as a function of the transverse momentum p_T in central Pb+Pb collisions at $\sqrt{s_{NN}} = 17.2$ GeV. The error bars indicate the combined statistical and systematic uncertainties. The data points with downward arrows indicate unbounded 90% CL limits on the direct photon yield. The WA98 data points are compared with scaled p+p, p+C results, pQCD calculation and scaled parametrization of direct-photon yields in p+p collisions. This figure has been taken from [26]. 29
1.7 $B_{\mu\mu}\sigma(J/\psi)/\sigma(DY)$ as a function of E_T; the absorption curve is fit to the NA38 $p-A$ and S-U data [35]. 30
1.8 $R_{AA}(p_T)$ for various centrality bins, for Au+Au relative to an N+N reference spectrum. This figure has been taken from [43]. 32

2.1 The Relativistic Heavy Ion Collider (RHIC) accelerator complex at Brookhaven National Laboratory. Nuclear beams are accelerated from the tandem Van de Graaff, through the transfer line into the AGS Booster and AGS prior to injection into RHIC. Details of the characteristics of proton and Au beams are also indicated after acceleration in each phase 40
2.2 Perspective view of the STAR detector, with a cutaway for viewing inner detector systems [81]. 42
2.3 Cutway side view of the STAR detector. 43
2.4 The STAR TPC surrounds a beam-beam interaction region at RHIC. The collisions take place at the center of the TPC [84]. 46
2.5 Beam's eye view of a central event in the STAR Time Projection Chamber. This event was drawn by the STAR level-3 online display [81]. . 48

2.6 The energy loss distribution for primary and secondary particles in the STAR TPC as a function of the p_T of the primary particle [84]. The curves are the Bethe-Bloch function shown in equation 2.1 for different particle species. 60

3.1 Basic principle of a preshower detector 63
3.2 A cross-sectional view of PMD showing the veto plane, lead converter and the preshower plane 65
3.3 Suspension mechanism of the PMD showing movement. The two halves of the PMD are shown separated. 67
3.4 Unit module having an array 24 × 24 hexagonal cells. 68
3.5 Schematic view of components of unit module 69
3.6 Unit module components with electronics board mounted onto the connector 70
3.7 Layout of the detector super modules. The black dots in each super module indicates the corner position of the super modules, where the cell numbering starts. 72
3.8 Layout of the top layer of the four-chip FEE board 75
3.9 Timing diagram for pre-trigger and L0 validation 77
3.10 Schematic diagram of PMD gas flow system 78
3.11 Azimuthal acceptance (ϕ) of PMD as a function of pseudorapidity (η) 80
3.12 Photon conversion efficiency as a function of photon incident energy. . 81
3.13 (left) Typical MIP spectra for cells with -1500 V, fitted with Landau distribution and (right) distribution of number of cells hit by MIP. . . 82
3.14 Distribution of (top) gain and (bottom) efficiency for randomly selected 40 cells from the prototype chamber. 84

3.15 (left) Typical cluster size for preshower expressed in terms of the cells affected by electron, (right panel) filled circles represent energy deposition (in terms of cluster ADC) spectra for electrons with three energies, (right panel) open circles represent the simulated energy deposition (in keV) for electrons with corresponding energies. Width of simulated spectra is smaller compared to test data. 85
3.16 (left) Readout width (%) shown for various energy deposition expressed in terms of cluster ADC (right) Calibration plot, showing the relation between the energy deposition obtained from simulation and the cluster ADC obtained from test data. 86
3.17 Flow chart showing the steps in generating simulated events. 89
3.18 Layout of PMD in GSTAR framework. 90
3.19 (a). Occupancy and (b). multihit probability as a function of pseudorapidity (η) for different impact parameter for all detector and PMD only in air cases. 92
3.20 $\delta\eta$ and $\delta\phi$ distribution (the difference between the original η, ϕ of the corresponding cluster position) for photons for PMD alone (dotted lines), PMD with upstream material (solid line). 93
3.21 η-dependence of photon counting efficiency ϵ_{gamma}, (left) and purity, f_p, (right) for different centralities. 95
3.22 Typical event display in preshower plane of PMD in Au+Au collisions at $\sqrt{s_{NN}}$ = 200 GeV. 97
3.23 Pseudorapidity distribution of photons in Au+Au collisions at $\sqrt{s_{NN}}$ = 200 GeV, for different centralities. 98

4.1 (a) $p\pi$ invariant mass distribution. (b) $K\pi$ invariant mass distribution. The symbols represent the same-event pair and the solid curve represent mixed-event pair. 105

4.2 (a)The $p\pi$ pair invariant mass spectrum. (b) The $K\pi$ pair invariant mass spectrum after mixed-event background subtraction. 106
4.3 The $p\pi$ invariant mass distributions for different p_T bins, each having bin width 0.2 GeV/c for minimum bias trigger. The solid curves stand for the fit function using eqn. 4.12 and the dashed lines stand for the Gaussian residual background. 110
4.4 Schematic diagram showing the production and re-generation of Δ and K^* by re-scattering and re-generation effects inside the medium (a) Δ and (b) K^*. 111
4.5 The $K\pi$ invariant mass distribution fitted to eqn. 4.17 to extract the $K^{*0}(892)$ yield in $d+Au$ collisions at $\sqrt{s_{NN}}$=200 GeV. The solid curve represents the Breit-Wigner fit to the data points with a linear background as given by the dashed line (eqn. 4.17). 114
4.6 The $K^0_S\pi^{\pm}$ invariant mass distribution fitted to eqn. 4.17 to extract the $K^{*\pm}(892)$ yield in $d+Au$ collisions at $\sqrt{s_{NN}}$=200 GeV. The solid curve represents the Breit-Wigner fit to the data points with a linear background as given by the dashed line (eqn. 4.17). 115
4.7 The total reconstruction efficiency as a function of p_T for K^{*0} and $K^{*\pm}$ for minimum bias as well as for different centralities of $d+Au$ collisions. The filled symbols are for neutral K^* and the open symbols are for charged K^*. 118
4.8 The total reconstruction efficiency as a function of invariant mass for different p_T bins. The solid line represents a fourth order polynomial fitting function. 119
4.9 The $p\pi$ invariant mass distribution fitted to eqn. 4.18 to extract the $\Delta(1232)$ yield in $d+Au$ collisions at $\sqrt{s_{NN}}$=200 GeV. The solid curve represents the Breit-Wigner fit to the data points with a Gaussian background as shown by the dashed line (eqn. 4.11). 120

4.10 The $p\pi$ invariant mass distributions for different p_T bins, each having bin width 0.2 GeV/c for minimum bias trigger. The solid curves stand for the fit function using eqn. 4.18 and the dashed lines stand for the Gaussian residual background. 122
4.11 The $p\pi$ invariant mass distributions for different p_T bins, each having bin width 0.2 GeV/c for (0-20)% $d+Au$ collision centrality. The solid curves stand for the fit function using eqn. 4.18 and the dashed lines stand for the Gaussian residual background. 124
4.12 The $p\pi$ invariant mass distributions for different p_T bins, each having bin width 0.2 GeV/c for (20-40)% $d+Au$ collision centrality. The solid curves stand for the fit function using eqn. 4.18 and the dashed lines stand for the Gaussian residual background. 125
4.13 The $p\pi$ invariant mass distributions for different p_T bins, each having bin width 0.2 GeV/c for (40-100)% $d+Au$ collision centrality. The solid curves stand for the fit function using eqn. 4.18 and the dashed lines stand for the Gaussian residual background. 126
4.14 The $K\pi$ invariant mass distributions for different p_T bins, each having bin width 0.2 GeV/c for minimum bias trigger. The solid curves stand for the fit function using eqn. 4.17 and the dashed lines stand for the linear residual background. 127
4.15 The $K^0_S\pi^\pm$ invariant mass distributions for different p_T bins, each having bin width 0.7 GeV/c for (0-20)% centrality. The solid curves stand for the fit function using eqn. 4.17 and the dashed lines stand for the linear residual background. 128
4.16 The $K\pi$ invariant mass distributions for different p_T bins, each having bin width 0.2 GeV/c for (0-20)% centrality. The solid curves stand for the fit function using eqn. 4.17 and the dashed lines stand for the linear residual background. 129

4.17 The $K^0_S\pi^\pm$ invariant mass distributions for different p_T bins, each having bin width 0.7 GeV/c for (20-40)% centrality. The solid curves stand for the fit function using eqn. 4.17 and the dashed lines stand for the linear residual background. 130
4.18 The $K\pi$ invariant mass distributions for different p_T bins, each having bin width 0.2 GeV/c for (20-40)% centrality. The solid curves stand for the fit function using eqn. 4.17 and the dashed lines stand for the linear residual background. 131
4.19 The $K^0_S\pi^\pm$ invariant mass distributions for different p_T bins, each having bin width 0.7 GeV/c for (20-40)% centrality. The solid curves stand for the fit function using eqn. 4.17 and the dashed lines stand for the linear residual background. 132
4.20 The $K\pi$ invariant mass distributions for different p_T bins, each having bin width 0.2 GeV/c for (40-100)% centrality. The solid curves stand for the fit function using eqn. 4.17 and the dashed lines stand for the linear residual background. 133
4.21 The $K^0_S\pi^\pm$ invariant mass distributions for different p_T bins, each having bin width 0.7 GeV/c for (40-100)% centrality. The solid curves stand for the fit function using eqn. 4.17 and the dashed lines stand for the linear residual background. 134
4.22 The raw yield $d^2N_{raw}/(2\pi p_T dp_T dy)$ for the average of the K^{*0} and $\overline{K^{*0}}$ yields and the average of K^{*+} and K^{*-} raw yields as a function of p_T at $|y| < 0.5$ in d+Au collisions for minimum bias as well as for different centralities. Filled symbols are for neutral K^* and open symbols are for charged K^*. 135
4.23 The corrected yield for average of Δ^{++} and $\overline{\Delta}^{--}$ as a function of p_T at $|y| < 0.5$ in $d + Au$ collisions for minimum bias as well as for different centralities. The spectra are fitted with exponential function as defined in eqn. 4.24. 138

4.24 The corrected invariant yield for both $(K^{*0}+\overline{K}^{*0})/2$ and $(K^{*+}+K^{*-})/2$ as a function of p_T at $|y| < 0.5$ in $d+Au$ collisions for minimum bias as well as for different centralities. Filled symbols are for neutral K^* and open symbols are for charged K^*. The spectra are fitted with Levy function as defined in eqn. 4.27 141

4.25 (a) Left panel of the figure shows the K^* mass as a function of p_T. The dashed line and the dotted line represent the K^{*0} and $K^{*\pm}$ mass values from Particle Data Book [56]. The solid symbols are for neutral K^* and the open symbols are for charged $K^{*\pm}$ with their stat. uncertainties. (b) Right panel shows the Δ mass from real data (filled symbols) and the Δ mass obtained from the Monte Carlo (MC) simulation (open symbols) as a function of p_T with their statistical uncertainties. The dashed line represents the Δ mass values from Particle Data Book. The shaded region show the systematic uncertainties on the obtained values. 143

4.26 (a) Left panel of the figure shows the K^* width as a function of p_T. The dashed line and the dotted line represent the standard K^{*0} and $K^{*\pm}$ width values from Particle Data Book [56]. The solid symbols are for neutral K^* and the open symbols are for charged $K^{*\pm}$. (b) Right panel shows the Δ mass from real data (filled symbols) and the Δ mass obtained from the Monte Carlo (MC) simulation (open symbols) as a function of p_T. The dashed line represents the Δ mass values from Particle Data Book. The errors are statistical. The shaded region show the systematic uncertainties on the measured value. 144

4.27 The Δ and K^* $\langle p_T \rangle$ as a function of charged hadrons compared to π^-, K^- and $\overline{p}$ in p+p, d+Au and Au+Au collisions. 148

4.28 The K^*/K and Δ/p ratios as a function of charged hadrons 156

4.29 The Δ and K^* nuclear modification factor as function of p_T. 159

List of Tables

4.1 The measured resonances with their decay channels, branching ratios, widths and lifetimes. 100

4.2 Centrality definitions for different uncorrected FTPC east reference multiplicity ranges. Uncorrected N_{charge} stands for the average value of uncorrected reference multiplicity in certain centrality bin. In the last column N_{bin} represents the number of binary collisions calculated from Glauber model. 101

4.3 Number of events from different centralities used for the present Δ and K^* analysis. 103

4.4 The average values of Δ^{++} and $\overline{\Delta}^{--}$ invariant yields $d^2N/(2\pi p_T dp_T dy)$ in each p_T bin for minimum bias and different collision centralities. . 137

4.5 The average yield of Δ^{++} and $\overline{\Delta}^{--}$ at $|y| < 0.5$ and the inverse slope parameter T for minimum bias and and different collision centralities with their stat. uncertainties and sys. uncertainties 137

4.6 The average of K^{*0} and $\overline{K}^{*0}$ invariant yields $d^2N/(2\pi p_T dp_T dy)$ in each p_T bin for minimum bias and different collision centralities. 140

4.7 The average of K^{*+} and K^{*-} invariant yields $d^2N/(2\pi p_T dp_T dy)$ in each p_T bin for minimum bias and different collision centralities. 140

4.8 The average of K^{*0} and $\overline{K}^{*0}$ and average of K^{*+} and K^{*-} yields at $|y| < 0.5$, the inverse slope parameter T and the exponent n for minimum bias and different collision centralities with their stat. uncertainties and sys. uncertainties. 142

4.9 The $\langle p_T \rangle$values for Δ and K^* and Δ/p and K^*/K ratio for centralities of d+Au collisions with their stat. and sys. uncertainties. 147

4.10 The systematic uncertainties in percentages for Δ and K^* at midrapidity ($|y|$ <0.5) on dN/dy and $\langle p_T \rangle$ in minimum bias $d + Au$ collisions. 154

Chapter 1

The Physics of Relativistic Heavy Ion Collisions

1.1 Introduction

1.1.1 Deconfinement and Phase Diagram

The nucleus of an atom is a composite of many-nucleon system. The force which binds the nucleons together inside the atomic nuclei is the strong force. The physics of strong interaction is described by the theory of *quantum chromodynamics* (QCD) [1]. In this theory the relevant fields are quark and gluon fields with the associated particles which are quarks and gluons. There is an internal degree of freedom *viz.* the color degree of freedom, which provides the arena for the interaction of these particles. The dynamics of this *color* degree of freedom gives rise to the term *'chromodynamics'* for the strong interaction.

In phenomenological quark models, mesons can be described as quark-antiquark bound states, and baryons can be considered as three-quark bound states. Till now, it is found that all the hadronic states which can be observed in isolation are color

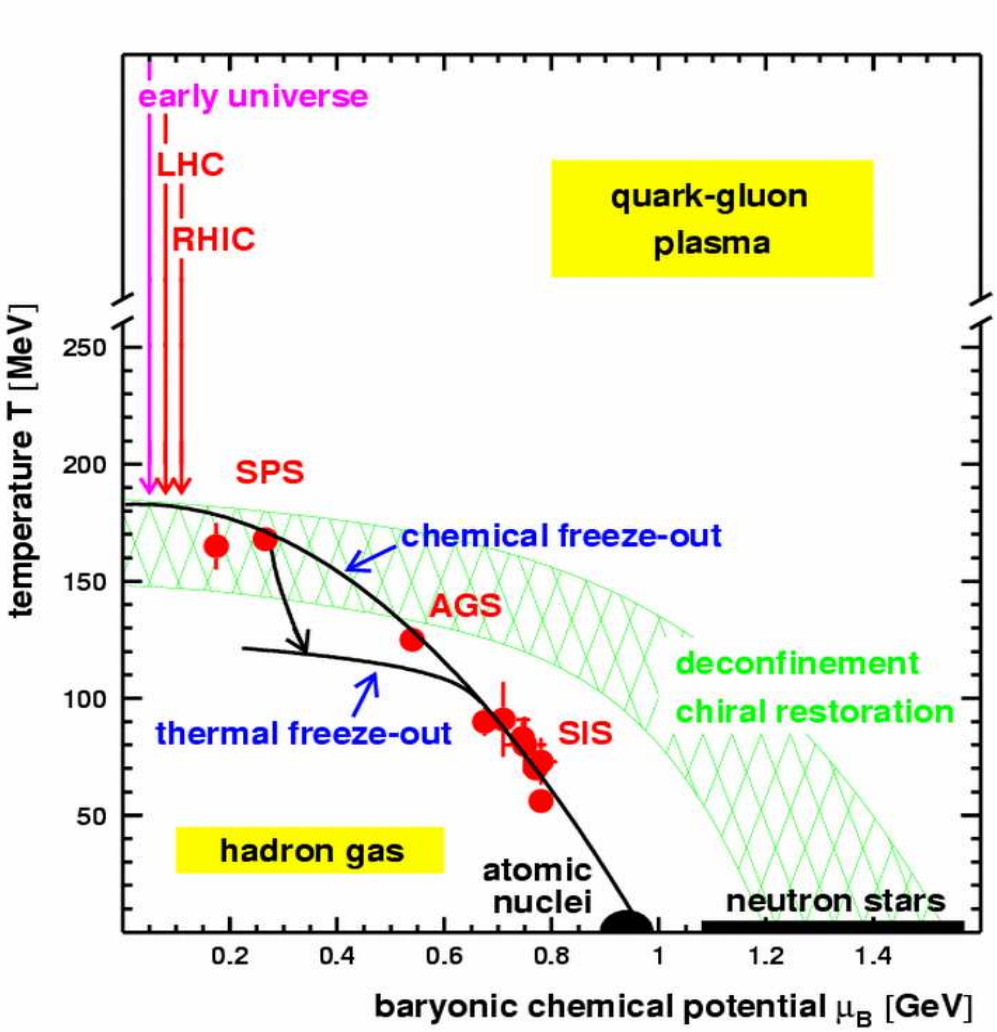

Figure 1.1: Phase diagram of hadronic and partonic matter, showing hadron gas and quark gluon plasma regions. The temperature T and the baryochemical potential μ_B data are derived from the particle yield ratios. The solid curve through the data points represents the chemical freeze-out of hadronic matter. This figure is taken from [5].

singlet states, which are completely antisymmetric with respect to the exchange of any two quarks. Experimentally, no single quark, which is described by a color triplet state, has ever been observed. Therefore, it is held that only hadrons in the color singlet state can be isolated and observed. The non-observation of a single quark in isolation also suggests that the interaction between quarks and gluons must be strong on large distance scales. On the other hand, the nature of the interaction between quarks and gluons on short distance scales, as provided by deep-inelastic scattering experiments is quite different. In these experiments, an incident electron interacts with a quark within a hadron with a transfer of momentum from the electron to the quark. The measurement of momentum of the electron before and after the collision allows a probe of the momentum distribution of quarks (or partons) inside the nucleon. It was found that with very large momentum transfers, the quarks inside the hadron behave as if they are almost free [2]. The strong coupling between quarks and gluons at large distances and the asymptotic freedom at short distances are the two remarkable features of QCD.

At very high energy density and very high temperature, a deconfinement of quarks and gluons is expected. In such a case the hadrons should undergo a phase transition from the confined hadronic matter to the deconfined phase of quarks and gluons known as the quark-gluon plasma (QGP). If a nucleus, which normally has a nucleon density $\rho_0 \approx 0.14$ nucleons/fm^3 and an energy density $\varepsilon_A \approx 0.13$ GeV/fm^3 is put into a state in which the nucleon density becomes $\rho \approx$ (10 to 15) ρ_0 and the energy density becomes $\varepsilon \approx$ (15 to 25) $\varepsilon_A \approx$ (2 to 3) GeV/fm^3, or into a state where the temperature is higher than a critical value, T_C approximately 160 MeV [3], then a phase transition to a QGP state with deconfined quarks and gluons should occur. Fig. 1.1 shows the phase diagram of the hadronic and partonic matter.

1.1.2 Chemical and Kinetic Freeze-out

In head-on relativistic heavy ion collisions, two nuclei approach one another at 99.95% of speed of light. The two nuclei appear as flat "pancakes" because of the Lorentz contraction. During the initial stage of the collision, the energy density is higher than the critical value of 0.13 GeV/fm^3 at which lattice QCD calculations predict a deconfinement of quarks and gluons in the system. In this stage, the high transverse momentum (p_T) jets and $c\overline{c}$ pairs will be produced due to the large momentum transfer scattering processes on the parton level.

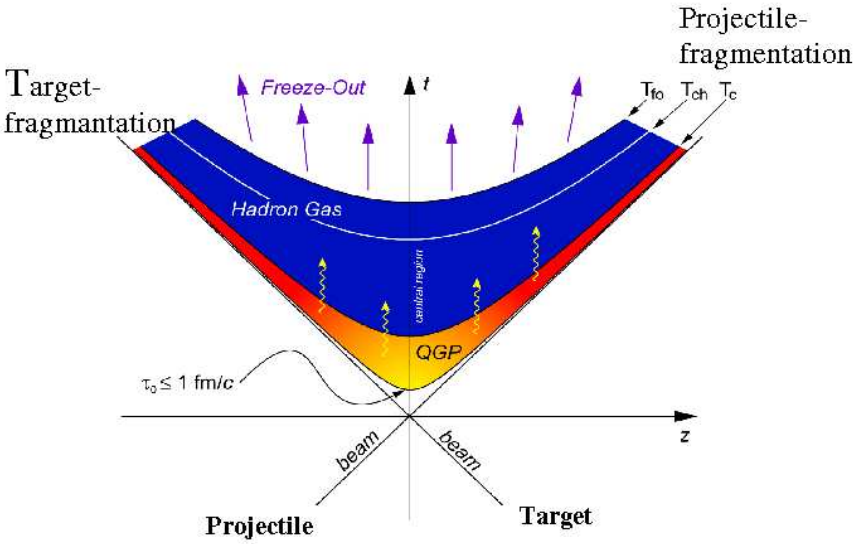

Figure 1.2: Space-time diagram of longitudinal evolution of the quark-gluon plasma.

An important question in relativistic heavy ion physics is whether the matter

reaches equilibrium during the collision process or not. If the system is in equilibrium state with QGP formed, then thermodynamics can be used to describe the system. In this case, the particle yields and their spectra will reflect the equilibrium condition. However, there may be two different types of equilibrium which are commonly discussed- *chemical* and *thermal*. The chemical equilibrium occurs when the creation and annihilation of the particles, reach their equilibrium values. The resulting particle abundances no longer change on average. The thermal equilibrium occurs when the whole system reaches the same temperature after which the particle spectra no longer change. More precisely, when the system starts expanding the mean distance between the particles and the time between interactions increase. When the interaction cease, this leads to freeze-out because probability of further interaction is small. The inelastic cross section determines when the chemical freeze-out would occur while the total cross section determines the time for thermal freeze-out. Since inelastic cross sections are always smaller than the total cross section, the inelastic reactions that change the particle species cease leading to a chemical freeze-out at an earlier time than the change in kinematics and temperature resulting in a thermal freeze-out.

After the initial hadronization, the system may evolve as an interacting hadron gas. The elastic interactions between hadrons will change the p_T distribution of the particles. At a certain point (which can vary according to the particle species), the hadrons will stop interacting and freeze out. This is known as the kinetic freeze-out. In order to determine whether a system has reached equilibrium, particle yields and spectra are compared with models that assume equilibrium. The particle ratios provide information for chemical equilibrium, whereas particle spectra provides information about thermal equilibrium [52]. Final state interactions between the produced particles determine the dynamical evolution of the system. In e^+e^- and $hadron - hadron$ collisions only few particles are produced. It is unlikely that many final state interactions occur. The particles decouple ("$freeze - out$") from the system soon after production. However, in case of nucleus-nucleus (AA) collisions the

density of produced particles are sufficiently large over an extended region in space and time. In that case, the mean free path of the produced particles becomes small and many final state interactions occur. These interactions drive the system towards *thermodynamic* equilibrium. Fig. 1.2 shows the space-time diagram of longitudinal evolution of the quark-gluon plasma.

1.2 Estimation of Initial Energy Density in High-Energy Nucleus-Nucleus Collisions

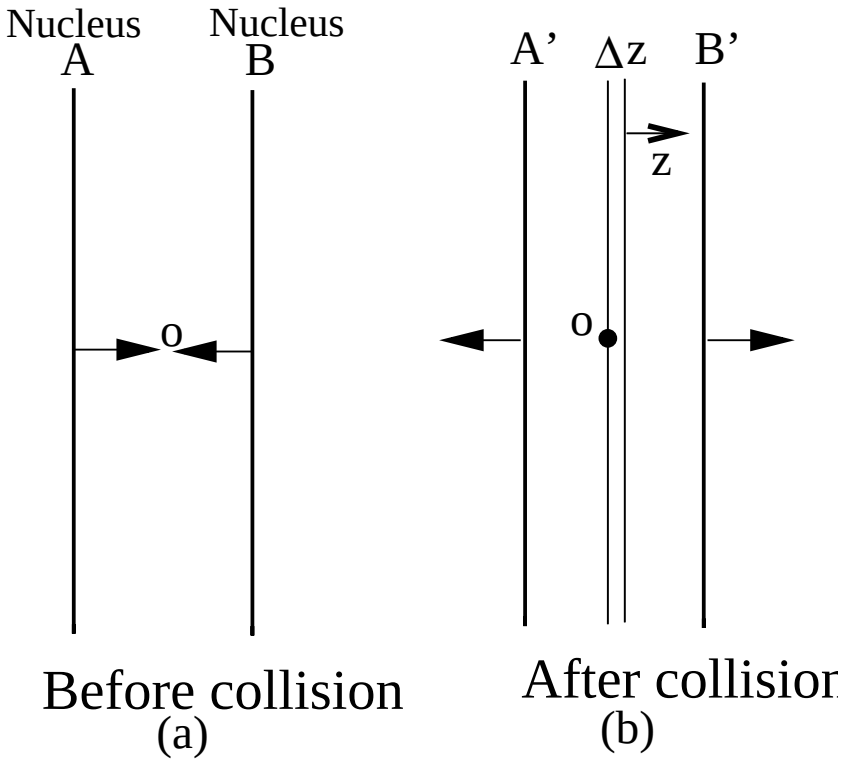

Figure 1.3: (a) The configuration of two nuclei A and B before collision. (b) The configuration after collision with energy deposited in the region around $z \sim 0$.

Bjorken has introduced a relation to estimate the energy density achieved in the high energy nuclear experiments [6]. In the high energy Heavy Ion (HI) collision,

we can represent the two colliding heavy nuclei by two thin discs because of Lorentz contraction. To estimate the initial energy density ε_0 before the hydrodynamical evolution, we need to find out the content of the energy deposited in the collision region and the relevant volume. The energy deposited in the collision region eventually manifests itself in the form of produced hadrons coming out from the collision region. As shown in Fig 1.2, the particles produced stream out from the collision point (z, t) = (0,0) and the volume they occupy depends on time. The produced particles are characterized by their rapidity distribution or rapidity density, dN/dy as a function of rapidity, y. In the center-of-mass frame, the matter is at rest *i.e.* at z = 0. As shown in Fig 1.3, let us take a longitudinal length of thickness Δz at z = 0. The volume formed by Δz is $A_T \Delta z$, where A_T is the transverse area of overlapping region in the collision. The number density in this volume at z = 0 and at $\tau = \tau_0$ is

$$\frac{\Delta N}{A_T \Delta z} = \frac{1}{A_T} \frac{dN}{dy} \frac{dy}{dz} \mid_{y=0} \tag{1.1}$$

The initial energy density can then be written as

$$\varepsilon_0 = \frac{m_T}{\tau_0 A_T} \frac{dN}{dy} \mid_{y=0} \tag{1.2}$$

where τ_0 is the *proper time*. It is normally interpreted as the parton *formation time*, i.e. the time needed to pass from the initial hadronic environment to the partonic degrees of freedom. Usually, this time is taken as 1 fm/c for Pb+Pb collisions at center-of-mass energy $\sqrt{s_{NN}}$=17 GeV carried out in the late nineties at the European Centre for Nuclear and Particle Research (CERN), Geneva. However, there is no real consensus as to what is the appropriate formation time τ to be used at much higher centre-of mass energy like what is available at the Relativistic Heavy Ion Collider (RHIC) at Brookhaven National Laboratory, USA. But there are arguments that it should be smaller than 1 fm/c at higher energies as it takes less time to equilibrate the system. It can be estimated from theoretical arguments while A_T can be estimated from nuclear geometry [7]. The other two variables namely the multiplicity distribution and the "transverse mass" can be obtained from experimental data.

1.3 Relativistic Heavy Ion Physics Programs: past, present and future

The most useful experimental approach to study QCD at high temperature and the related phase transition is to collide two heavy ions at very high energies. In such collisions at relativistic velocities there is both a *compression of baryonic matter* in the nuclei and a release of a large amount of energy within a small volume from simultaneous collisions of many nucleons. Both of these consequences of interactions have the potential to produce new phases of QCD matter.

Over the last two decades an enormous amount of work, on both experimental and theoretical fronts, has been carried out to look for signatures of a possible phase transition to QGP phase through heavy ion collisions. The various signatures of a QCD phase transition to a QGP state include strangeness enhancement, anomalous charmonium suppression, enhanced dilepton production and observation of direct photons together with a large value of elliptic flow. Heavy ion collision experiments carried out so far have aimed at the observation of one or more of the above signatures. A discussion on each of these is given in the following sections.

The experimental programs in relativistic heavy ions started in 1986 using the Alternating Gradient Synchrotron (AGS) facility at Brookhaven National Laboratory (BNL), USA and the Super Proton Synchrotron (SPS) at the European Centre for Nuclear Research (CERN), Geneva. At CERN, there have been approximately 15 heavy ion experiments utilizing beams of O at 60 and 200 GeV/c per nucleon, S at 200 GeV/c per nucleon and Pb at 158 GeV/c per nucleon [3]. As can be seen the idea behind using heavier and heavier targets together with an increase in the beam energy was mainly to reach the higher energy density and temperature which could result in QGP formation. Finally, with Pb+Pb collisions at $\sqrt{s_{NN}}$= 17.2 GeV, results from seven large experiments at CERN viz NA44, NA45, NA49, NA50, NA52, NA57/WA97 and WA98 showed indications regarding a possible phase transition which everybody had been looking for. More than 20 different hadron species have been measured by

these seven experiments. The experiments NA44 and NA45 looked for two particle correlations which gave information regarding the fire ball source. In addition, NA45 also looked at the dilepton production showing an excess of these to be produced within a mass window between 250 and 700 MeV. NA49, NA50 and WA97 showed an enhancement in strange particle production at SPS. At the same time WA98 experiment reported on the observation of direct photons with NA50 reporting an anomalous suppression of J/ψ. Based on a compilation of the above data taken at SPS there has been a formal announcement regarding the observation of QGP at CERN SPS. However, with alternate explanations for some of the observations there was a need to go higher up in energy density where the life time of the deconfined phase is expected to be higher.

At AGS in BNL, ion beams of S and Au, accelerated to momenta of 14 and 11 GeV/c per nucleon, respectively, have been utilized in about 10 fixed-target experiments. The experimental data did suggest the formation of high density matter without any signature regarding QGP formation. The Relativistic Heavy Ion Collider (RHIC) at BNL which came after the SPS running period, has been designed for head on Au+Au collisions at $\sqrt{s_{NN}} = 200$ GeV. Here the total energy in the center-of-mass in central collisions is almost 40 TeV, the largest energy so far achieved in nucleus-nucleus collisions. The idea was to achieve an energy density where QGP formation would take place easily in a central collision.

At RHIC, at the moment there are four experiments, which can be classified into two groups: "large" experiments (STAR and PHENIX) and "small" experiments (PHOBOS and BRAHMS). The first two have large-volume and large-acceptance detectors, while the other two are of limited acceptance covering certain aspects of the collisions not addressed by the former ones. All the above four experiments have one common goal which is to study the formation of a new state of QCD matter by measuring different observables in different experiments.

Since the beginning of the RHIC run in 2000 till date these experiments have

studied the collisions of $p + p$, $d + Au$, $Au + Au$ and $Cu + Cu$ at different center-of-mass energies, $\sqrt{s_{NN}}$ ranging from 19.6 to 200 GeV (per nucleon pair). Based on a compilation of the RHIC data taken by the four experiments, there is a consensus that a strongly interacting medium is created with extremely high energy densities achieved in central Au+Au collisions at the highest collision energy. From the study of various observables as a function of collision energy and the system size, it appears that the transition to this new state is a cross-over.

Recently, the accelerator program at CERN is being upgraded with the construction of a Large Hadron Collider (LHC) which has a primary goal of discovering the much eluding Higgs Boson whose existence is very much essential regarding the successful experimental verification of the Standard Model. At LHC it would be possible to look at pp collisions at a centre-of-mass energy of 14 TeV. In addition to proton it would be used to accelerate Pb ions to an energy of 5.5 TeV per nucleon with a total energy of about 1250 TeV which is thirty times that available at RHIC at present. With a much higher life time of the deconfined state it would be possible to not only detect the state but also to study some more of its properties. Five major experiments have been approved for LHC which are CMS (Compact Muon Spectrometer), ALICE (A Large Ion Collider Experiment), ATLAS (A Toroidal LHC Apparatus), LHCb (Large Hadron Collider beauty experiment), and TOTEM (Total Cross Section, Elastic Scattering and Diffraction Dissociation at the LHC). The heavy ion experiment with the ALICE detector is supposed to take data in 2007.

Apart from LHC, also there are other facilities coming up to study the deconfined state of the strongly interacting matter. One of such proposed experiments is the Compressed Baryonic Matter (CBM) experiment at GSI [4]. This will use heavy ion beams upto Uranium at beam energies ranging from 2-45 AGeV (for Z/A = 0.5) and upto 35 AGeV (for Z/A = 0.4). The maximum proton beam energy will be about 90 GeV. Using the proton beams with energies up to 90 GeV, CBM experiment can carry out study on heavy quark production in p+p and p+A collisions. The production mechanism of heavy quarks in this energy range are sensitive to the quark

and gluon distributions in the nucleon. So far there is no data existing below proton beam energies of 400 GeV, so it will be interesting to see the results of CBM. Also the data on the production of charm, strangeness and low-mass vector mesons in p+p and p+Au collisions are absolutely needed as a reference for the results obtained from the A+A collisions. The CBM detector will be well suited for the measurement of heavy resonances and exotic particles like pentaquarks produced in p+p and p+A collisions. In the nucleus-nucleus collisions CBM will focus on the search for: (i) in-medium modifications of hadrons in super-dense matter as a signal for the onset of chiral symmetry restoration; (ii) a deconfined phase at high baryon densities; and (iii) the critical endpoint of the deconfined phase transition. The experiment aims at a comprehensive study of relevant observables by systematically scanning the parameters like beam energy, system size and the collision centrality.

1.4 Some Suggested Signatures of QCD Phase Transition

In relativistic heavy ion collisions, at sufficiently high energy densities, we expect the formation of a deconfined phase of strongly interacting quarks and gulons in the form of a QGP. Subsequent cooling of the QGP state would result in the formation of hadrons. During the time when the matter is in the QGP phase, the particles which arise from the interactions between the constituents of the plasma will provide information about the state of the plasma. The detection of the products of their interactions is useful as a plasma diagnostic tool. It is generally recognized that, there is not a single unique signal which gives the complete identification of the QGP state. One approach is to look for primordial remnants in the observed hadron features: the discontinuities in the momentum distribution of the secondaries reflecting a first order phase transition. Another suggestion is to look for signals produced at early times and not affected by subsequent hadronization, signals such as direct (thermal)

photons and dilepton pairs, which are emitted by the plasma.

Since direct photons and dileptons originate during the early times, it is interesting to see if they are disturbed by the final hadronic state. The difficulty in studying such signals is that they typically have much smaller cross section compared to hadronic observables. One may also study the effect of the produced dense medium on the observed production of heavy quark bound states, like J/Ψ or hard jets. There are also other observables that are thought to be sensitive to the early times. One of them is the azimuthal anisotropy in the emission of particles. In the following section, we will discuss some of the proposed signatures of QGP like:

- Thermodynamic variables measuring the equation of state,
- Flow,
- Strangeness enhancement,
- Thermal photons and dileptons,
- J/Ψ suppression,
- Jet quenching,
- Medium effects on resonance properties.

1.4.1 Thermodynamic Variables

Global observables like multiplicity, transverse energy and momentum spectra of the emitted particles give insight into the 'kinetic freeze-out' stage of the system. At this stage hadrons are no longer interacting and their momenta do not change. The experimentally measured spectra of hadronic particles thus reflect the state of the system at freeze-out. This gives the information, whether the QGP, *i.e.* an equilibrated state of quarks and gluons, was created at some stage during the evolution of the system [8]. It has been suggested that, the correlation between mean transverse momentum

($\langle p_T \rangle$) and multiplicity of the produced particles may serve as a probe for the equation of state of the hot hadronic matter. Using these two variables one can look into the structure of the Temperature - Energy (T - ε) diagram [9]. According to the Landau's hydrodynamical model [10], the rapidity density (dN/dy), reflects the entropy, whereas the mean transverse momentum ($\langle p_T \rangle$) reflects the temperature. The rapidity density linearly scales with the $\langle p_T \rangle$, except at the phase transition points. If the phase transition is of first order, then the temperature remains constant at the point of phase transition from hadron gas to QGP phase thereby increasing the entropy density. So the $\langle p_T \rangle$ will show a plateau while entropy will go on increasing. The observables like dN/dy and $< p_T >$ of charged particles will give some indication about the QGP phase and also the order of phase transition.

In an experiment it is not possible to directly measure the impact parameter of the collision. So, one has to use an indirect method to find out the centrality of the collision. The event multiplicity (N) is one of the observables that is correlated to the impact parameter. Multiplicity distribution gives the information on both the impact parameter and the energy density of the collision. From geometry, for every impact parameter b, one can calculate the average number of nucleons that participate in the collision (N_{part}). One can obtain a statistical mapping of $< N > \rightarrow < N_{part} > \rightarrow < b >$. The number of participants (N_{part}) is also called the number of *wounded nucleons* [11]. The scaling of multiplicity (N) with the number of participants (N_{part}) is a reflection of the particle production due to low momentum transfer ($soft$) processes. It is expected that, at high energy there will be an increased particle production from large momentum transfer ($hard$) processes. In case of hard processes, the multiplicity of produced particles, N, has been found to be proportional to the number of elementary nucleon-nucleon collisions. This we call as the *number of binary collisions* (N_{coll}). Some recent models [12] suggest that the particle production can be understood in terms of contributions from both soft and hard processes with N being a linear combination of N_{part} and N_{coll}. However, as has been mentioned earlier, the rapidity density of N as a function of $\langle p_T \rangle$ is expected to

show a plateau for a first order phase transition to QGP phase.

1.4.2 Flow

The measurement of an azimuthal anisotropy in the emission of particles (with respect to the *reaction plane*, [13] *i.e.* the plane formed by the beam direction and the direction of vector connecting the center of the two colliding nuclei) is sensitive to the early times. When one approaches the phase transition region the equation of state (EOS) becomes very soft and only a small increase of the transverse flow velocity is expected. When the energy density significantly exceeds that needed for QGP formation, the collective flow is expected to increase again [14]. Calculations of hydrodynamic expansion with a bag model type EOS predicts three stages with rapid, modest and again rapid increase in transverse flow with the increase in beam or internal energy. The existence of some 'plateau' in the middle is the consequence of softness of EOS in the 'mixed phase'. Detailed numerical studies in context of the hydrodynamical model have shown that this characteristic feature is rather weak in realistic models which do not include a rehadronization process [15, 16].

In non-central Nucleus-Nucleus collisions, the event in the plane perpendicular to the beam axis exhibits an azimuthally anisotropic shape. This results, because of the pressure gradients which drive the emission of particles. The azimuthal distribution of particles in momentum space can be expanded in a form of Fourier series

$$E\frac{d^3N}{d^3p} = \frac{1}{2\pi}\frac{d^2N}{p_T dp_T dy}(1 + \sum_{n=1}^{\infty} 2v_n cos[n(\phi - \Psi_r)]) \tag{1.3}$$

where Ψ_r denotes the reaction plane angle. The Fourier expansion coefficients v_n, stand for the nth harmonic of the event azimuthal anisotropy. The first harmonic coefficient is called the *directed flow*, the second harmonic coefficient representing what is called the *elliptic flow*. Since v_2 comes from the azimuthal asymmetry of pressure gradients, it's a good probe of the initial stage of the interactions.

Among the first results from RHIC were measurements of v_2 for charged hadrons as a function of p_T for different collision centralities and for different particle species

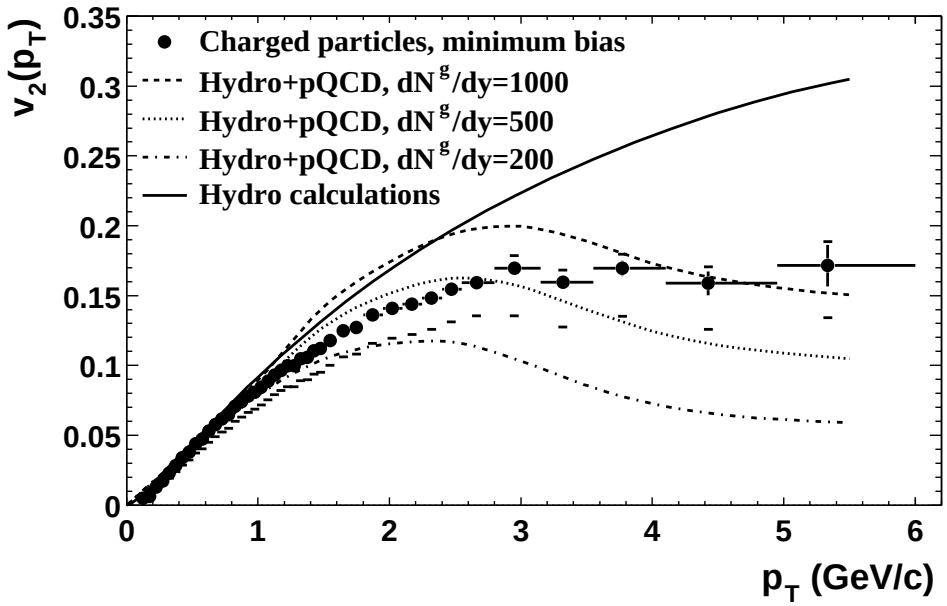

Figure 1.4: $v_2(p_T)$ for minimum-bias events (circles) for Au+Au collisions at $\sqrt{s_{NN}}$ = 200 GeV. The error bars represent the statistical error and the caps show the systematic uncertainty. The data are compared with hydro-pQCD calculations [20] assuming the initial gluon density dN^g/dy = 1000 (dashed line), 500 (dotted line, and 200 (dashed-dotted line). Also shown as pure hydrodynamical calculations [21] (solid line). This figure has been taken from [17].

[17, 18]. Fig. 1.4 compares the minimum-bias differential elliptic flow coefficient $v_2(p_T)$ with the same obtained from hydrodynamic calculations [21] for all charged particles taken as a whole. For p_T < 2 GeV/c the hydrodynamic model has been found to provide a good description of the data. But for p_T > 2 GeV/c, the role of hard scattering of partons become prominent with the hydrodynamic model failing to explain the data. These results may be explained assuming a high initial gluon density and energy loss in the early partonic stage. The observed saturation of v_2 at $p_T \sim$ 2 - 3 GeV/c can be reproduced in the parton cascade model with only elastic scatterings, but higher initial gluon densities, ($dN^g/d\eta \sim$ 15,000) or larger elastic parton cross sections, $\sim$ 45 mb [17, 22]. RHIC data also show that, combined with the observations of transverse radial flow, the measurement of elliptic flow for multiply

strange baryons (e.g. Ξ and Ω) may provide some key and definitive insights into a state of matter and possible partonic collectivity in the early stage of the collision.

1.4.3 Strangeness Enhancement

Another prediction for a QCD phase transition is the enhancement in the production of strange hadrons. The argument behind the strangeness enhancement is as follows. In hadronic reactions, the production of particles containing strange quarks are normally suppressed due to the higher mass of the strange quark ($m_s \simeq 60-170 MeV/c^2$) as compared to u and d quarks. In the QGP phase, the temperature is of the order of the s-quark mass and rapid filling of the phase space available for u and d quark should favor the production of $s\bar{s}$ pairs in interactions of two gluons [23, 24]. This should be reflected in an enhancement of the production of multi-strange baryons and strange antibaryons if a QGP is formed when compared to a purely hadronic scenario at the same temperature. Since strange hadrons interact strongly, their final-state interactions can be modeled in details and comparison of strange particle yields can be carried out.

Strangeness enhancement has been studied at the AGS, SPS and RHIC energies. The ratio of kaon to pion production is often used to quantify the strangeness enhancement. STAR has currently measured the K/π ratio at mid-rapidity. Fig. 1.5 shows the K/π ratio at mid-rapidity versus collision energy in p+p and A+A collisions. There is a rapid increase in K^+/π^+ ratio from AGS to SPS energy. Then the ratio saturates and practically remains constant from $\sqrt{s_{NN}} \sim 10$ GeV to 130 GeV. The ratios are large in A+A collisions compared to p+p collisions at similar energies, which shows the strangeness enhancement.

1.4.4 Thermal Photons and Dileptons

The detection of radiation from a high temperature QGP would be an ideal signal to detect, as black body radiation is one of the most directly accessible probes of the

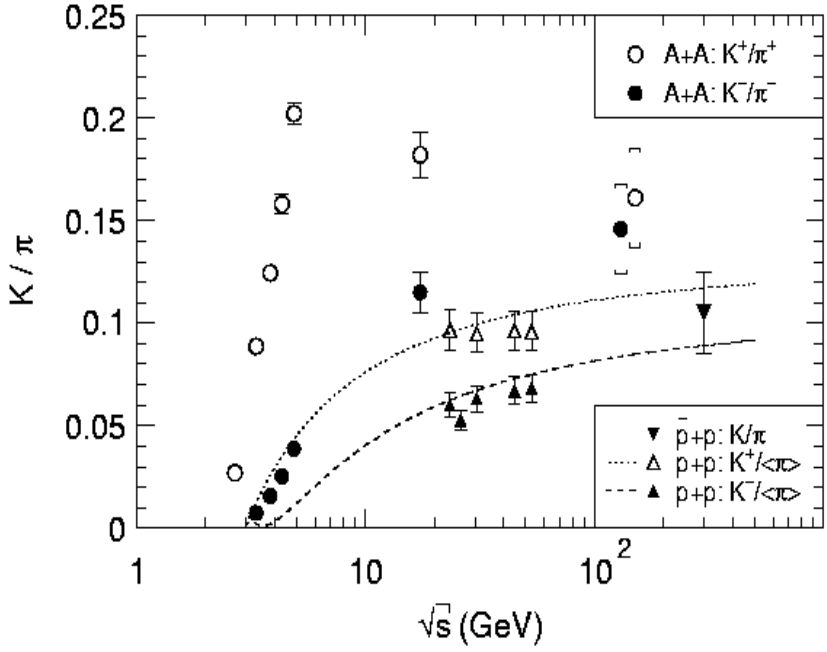

Figure 1.5: Mid-rapidity K/π ratios versus $\sqrt{s_{NN}}$. The error bars show the statistical errors. The systematic errors are on the STAR data are indicated by caps. This figure has been taken from [25].

temperature of a given system. The thermal photons are produced by the annihilation of quark, anti-quark pairs ($q\overline{q} \rightarrow \gamma g$) and Compton scattering of quark and anti-quark with gluons ($gq \rightarrow \gamma q$, $g\overline{q} \rightarrow \gamma \overline{q}$) in the QGP. The photon interacts with the particles in the collision region only through the electromagnetic interaction. Consequently, the mean-free path of the photon is expected to be quite large and therefore it may not suffer a collision after it is produced. On the other hand, the photon production rate and the photon momentum distribution depends on the momentum distributions of the quarks, anti-quarks, and gluons in the plasma. Therefore, photon produced in the QGP carry information on the thermodynamical state of the medium at the moment of their production. It must also be mentioned that a lot of photons are also produced from pion and eta meson decay making it very difficult to detect direct

photons coming from the QGP.

The WA98 experiment carried out at CERN has reported the observation of direct photon signals in Pb + Pb collisions at SPS [26]. Fig. 1.6 shows the invariant direct-photon yield as a function of transverse momentum (p_T) in central Pb+Pb collisions at $\sqrt{s_{NN}} = 17.2$ GeV. In the same plot, the WA98 data have been compared with the p+p and p+C results obtained from the other experiments, scaled by the average number of inelastic nucleon-nucleon collisions. Results of a perturbative QCD (pQCD) calculation are also shown in the figure for comparison. Comparing the results to pA data, one can see that there is an enhancement in photon yield in central collisions. The data also suggest a modification of the photon production mechanism. The above data had indicated the possibility of a clear signal of direct photons from a very hot QGP possibly formed at RHIC [27, 28].

In addition, dileptons can also carry similar information as thermal photons on the thermodynamic state of the medium. Dileptons produced in the QGP phase are essentially unaffected by the passage through the high-density matter because of the associated small scattering cross section. However, dilepton pair from vector meson decays are very difficult to detect due to the small branching ratios and the large combinatorial background. These backgrounds come from pion annihilation, resonance decays, $\pi - \rho$ interactions at lower mass region, whereas at higher mass region, the background is dominated by the Drell-Yan process. At RHIC energies there is an additional charm contribution above 2 GeV/c^2. Theoretical studies predict that there exists a window in the invariant mass of the produced dileptons, i.e. $2m_l \leq M \leq 2m_\pi$, where the contribution is predominantly from the QGP phase [29]. Thus looking for dilepton signature has proved to be a difficult experimental observable, but there is a continued effort to improve the sensitivity of the measurements. A study of the p_T dependence in various mass windows might help to disentangle the different contributions to the spectrum.

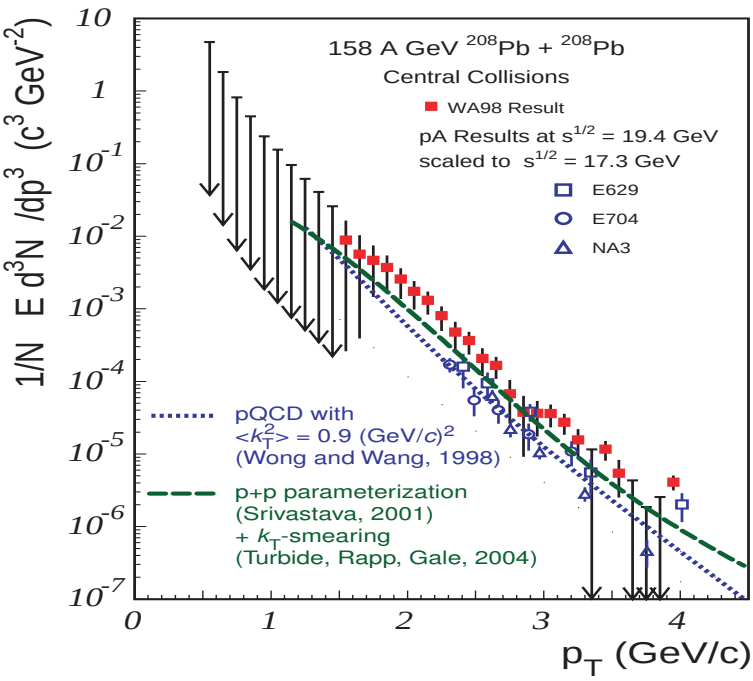

Figure 1.6: The invariant direct-photon multiplicity as a function of the transverse momentum p_T in central Pb+Pb collisions at $\sqrt{s_{NN}}$ = 17.2 GeV. The error bars indicate the combined statistical and systematic uncertainties. The data points with downward arrows indicate unbounded 90% CL limits on the direct photon yield. The WA98 data points are compared with scaled p+p, p+C results, pQCD calculation and scaled parametrization of direct-photon yields in p+p collisions. This figure has been taken from [26].

1.4.5 J/Ψ suppression

Another proposed signal for the QCD phase transition is that, the production of J/ψ is suppressed when there is a phase transition from confined to the deconfined phase of quarks and gluons. In a QGP the color charge of a quark is subject to screening due to the presence of quarks, anti-quarks and gluons in the plasma. This phenomenon is called the "*Debye screening*". If we place a J/Ψ particle, which is the bound state of a charm quark $'c'$ and a charm anti-quark $'\overline{c}'$, the Debye screening will weaken the interaction between c and $\overline{c}$ in the plasma. Because of this effect, a J/Ψ particle placed in the QGP at high temperatures will dissociate. Therefore J/Ψ production

in a QGP will be suppressed [30].

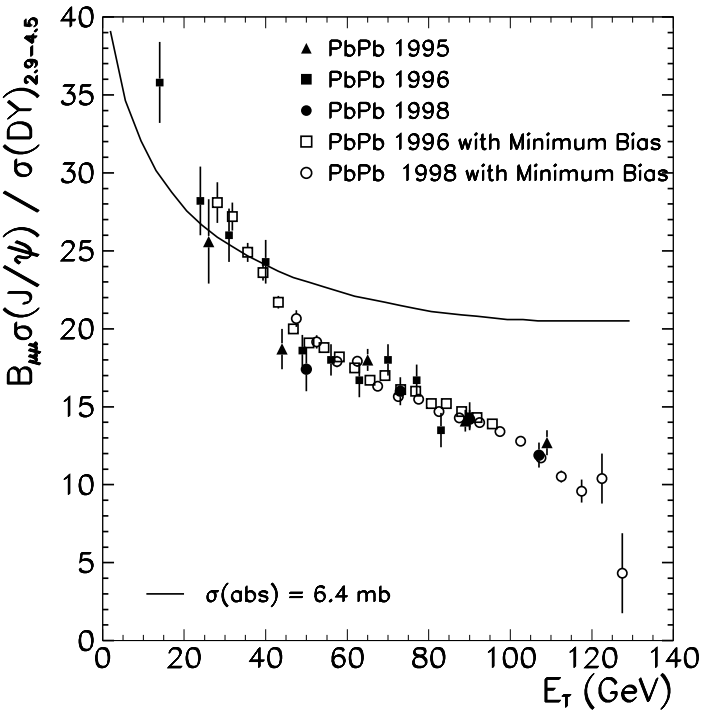

Figure 1.7: $B_{\mu\mu}\sigma(J/\psi)/\sigma(DY)$ as a function of E_T; the absorption curve is fit to the NA38 $p-A$ and S-U data [35].

"Anomalous" J/ψ suppression has been reported by the NA50 collaboration for central Pb + Pb collisions at SPS which has given evidence for QGP formation [31, 32, 33]. Fig. 1.7 shows the ratio $B_{\mu\mu}\sigma(J/\psi)/\sigma(DY)$ as a function of E_T, for the Pb+Pb data taken in different years by the NA50 experiment at SPS. The continuous line stands for normal absorption of J/ψ in nuclear matter. From the curve we see that, the J/ψ production follows the normal nuclear absorption pattern for peripheral collisions. But there is a clear deviation for the central collisions suggesting the onset of another J/ψ suppression mechanism.

This extra suppression observed at higher E_T can also be explained by taking the effect of E_T fluctuation [37]. In addition, there are nuclear effects, such as the breakup of the J/ψ by hadronic comovers, which also can result in a suppression in

the measured cross section [34].

1.4.6 Jet Quenching

Another predicted signature [38, 39, 40] regarding the formation of a deconfined state of high energy density is the suppression of partonic jets and their high p_T hadronic debris due to energy loss of the jets in the medium. High p_T quark and gluon jets, materialize very early during the collision. While propagating through the dense medium these partons will experience the strong interaction with the medium in the process loosing energy through gluon radiation. This energy loss is supposed to be larger in a medium of deconfined color charges than in normal hadronic matter. This effect, known as "Jet quenching", could show up as a depletion in the yield of high p_T hadrons making it a potential probe for the study of a high density deconfined phase [41, 42, 43]. In order to measure the high p_T hadron suppression in relativistic heavy ion collisions, a comparison of the hadron p_T spectrum (obtained from nucleus-nucleus collisions) with reference data from pp or $p\overline{p}$ collisions at the same energy is needed. A properly defined ratio of the two gives what is called the nuclear modification factor, R_{AA}, as defined below.

$$R_{AA}(p_T) = \frac{d^2N^{AA}/dp_Td\eta}{T_{AA}d^2\sigma^{NN}/dp_Td\eta} \tag{1.4}$$

Here $T_{AA} = < N_{bin} > /\sigma_{inel}^{NN}$ accounts for the collision geometry, averaged over the event centrality class. $< N_{bin} >$ corresponds to the equivalent number of binary NN collisions calculated using the Glauber model [7]. At low p_T the value of $R_{AA}(p_T)$ is less than unity. But the yield for hard process scales as $< N_{bin} >$ in the absence of nuclear modification effects [$R_{AA}(p_T) = 1$].

Fig. 1.8 shows RHIC results on $R_{AA}(p_T)$ of inclusive charged hadron for various centrality bins in Au+Au collisions with $\sqrt{s_{NN}} = 200$ GeV, relative to the nucleon-nucleon reference spectrum. From the figure $R_{AA}(p_T)$ is seen to increase monotonically for $p_T < 2$ GeV/c at all centralities. It saturates to unity for $p_T > 2$ GeV/c for

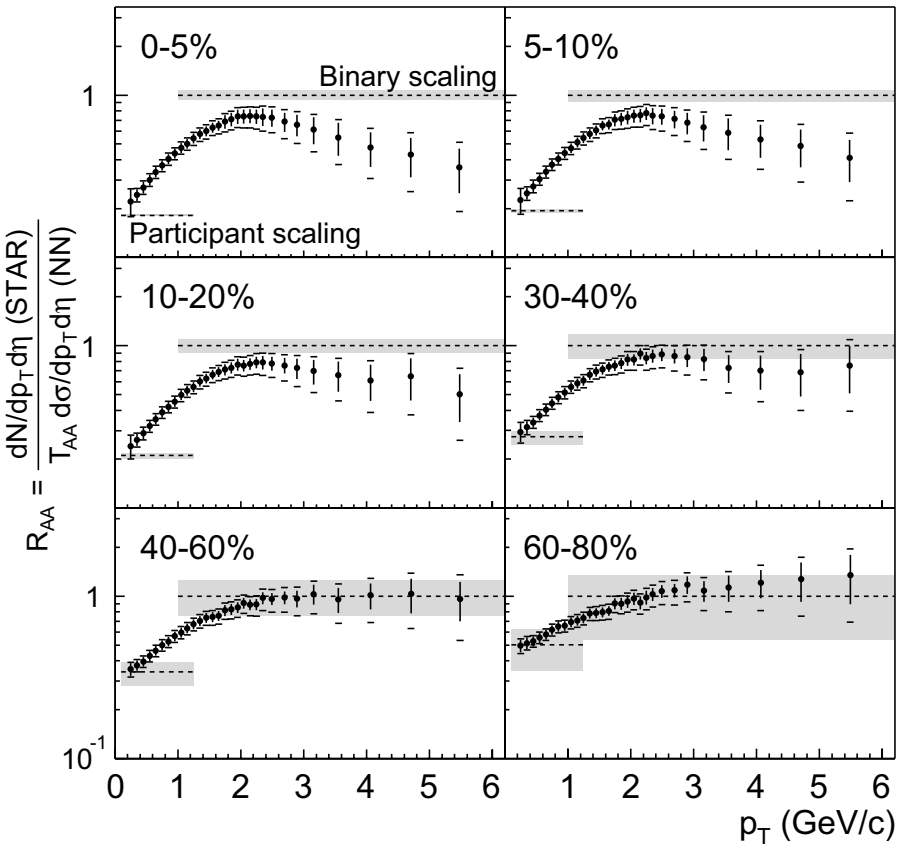

Figure 1.8: $R_{AA}(p_T)$ for various centrality bins, for Au+Au relative to an N+N reference spectrum. This figure has been taken from [43].

the most peripheral bins. In contrast, $R_{AA}(p_T)$ for the central bins reaches a maximum and then decreases strongly above $p_T > 2$ GeV/c. This shows the suppression of the charged hadron yield relative the nucleon-nucleon reference.

The high p_T hadron suppression in central Au+Au collisions can also be investigated by comparing the hadron spectra in central and peripheral Au+Au collisions. That's what we call R_{CP}. It is defined as

$$R_{CP} = \frac{< N_{bin}^{peripheral} > d^2N^{central}/dp_T d\eta}{< N_{bin}^{central} > d^2N^{peripheral}/dp_T d\eta} \tag{1.5}$$

1.4.7 Resonances and Their In-Medium Effects in Hot and Dense Matter

The strongly decaying particles having lifetimes (τ) about 10^{-23} sec (similar to the time taken for a light signal to cross a proton) are called '*resonances*'. The modifications of the resonance production rates and their in-medium properties are among the proposed signals of phase transitions in hot and dense matter [57]. The widths and masses of the ρ, ω and ϕ resonances in the dilepton pair invariant mass spectrum are sensitive to the medium-induced changes, especially to possible drop of vector meson masses preceding the chiral symmetry restoration. The results from CERES experiment with the S+Au and Pb+Au collisions at SPS energy showed an excess of dileptons in the low-mass region $0.2 < M < 1.5$ GeV/c^2, relative to pp and pA collisions [59, 60]. These go in line with microscopic hadronic transport models that incorporate downward mass shifts of vector mesons. When the resonance lifetime is comparable to the evolution time scales of the phase transition, the measured properties associated with the resonance (such as *mass*, *width*, *branching ratio*, *yield*, and *transverse momentum* (p_T) *spectra*) will depend upon the collision dynamics and chiral properties of the medium at high temperature and high energy density [61]. Resonances with extremely short lifetimes can decay inside the medium before all the accumulated in-medium effects might be erased. Hence, by measuring the resonance production, one can access information about how the resonances encounter the hot and dense medium. It has been argued that, there is significant effect on the reconstructed resonance mass due to the phase space [62, 63], interference [64], re-scattering [65] and dynamical effects [62].

1.4.8 Rescattering and Regeneration Effect

Since the resonances have very short lifetimes ($\sim$ few fm/c), a fraction of them decay inside the medium. The decayed daughters again undergo a period of re-interaction in the hadron gas phase [57, 67]. A portion of the resonances may decay before

the kinetic freeze-out stage and their hadronic decay daughter particles might be re-scattered by other particles in the hadron gas. This is called the $re-scattering\ effect$ of resonance daughter particles. This effect may destroy a part of the resonance signals. On the other hand, the hadronic particles in the medium can interact with each other generating new resonances contributing to signals. This is called the $re-generation\ effect$ of resonances. This can compensate in part the resonance signals which are lost due to the re-scattering.

Due to the resonance daughter particles' re-scattering and the re-generation effect, resonances are good candidates to probe the various properties of the hot-dense matter in relativistic heavy ion collisions. In particular, the fireball evolution properties between chemical and kinetic freeze-outs and the time scale between these two can be studied looking at the resonances [69, 70].

1.4.9 Measuring the Time Scale between Chemical and Kinetic Freeze-outs

It is important to study the resonance production in heavy ion collisions to infer about the time scale between chemical and thermal freeze-outs [71]. There are different views regarding the time scale between chemical and kinetic freeze-outs and whether the two freeze-out temperatures are nearly coincident [69]. The QGP signals should be visible in hadronic particles if there is zero time between the chemical and kinetic freeze-outs. However, the newly-formed hadrons could undergo a period of re-interaction in hadronic phase. In that case, the time scale between the two freeze-outs are hadron-specific. This could significantly alter any considered QGP signal.

For calculating the hadron abundances and hadron spectra, the distinction between the two freeze-outs are not necessary [72]. However, theoretical calculations taking resonance decays at a temperature of 165 MeV (close to the transition temperature for QGP as obtained from Lattice QCD), result in an inverse slope parameter

for the hadronic p_T spectrum which is 30-40 MeV lower. This shows that the temperatures for the two freeze-outs are different [73]. STAR data on $K^{*0}(892)$ production [77] in Au+Au collisions at $\sqrt{s_{NN}} = 200$ GeV at RHIC, do show that the kinetic and the chemical freeze-out temperatures are different [78]. This suggests a picture with a short expansion time between the two freeze-outs. Such picture is natural if the production of particles occur in such conditions where neither elastic or inelastic processes are effective. Both re-generation and re-scattering effects take place between the chemical and kinetic freeze-outs.

In order to estimate the time scale, the resonance particle should fulfill one of the following two conditions: (1) resonance signals destroyed by the re-scattering are much more than the signal produced by the re-generation effect; (2) the signal produced by the re-generation effect are much more than the signal destroyed by the re-scattering effect. If there is no significant difference between the amount of signals destroyed and produced, we can't measure the time scale between the chemical and thermal freeze-outs. In view of this, ρ^0 is a good candidate, which satisfies the second condition where as $K^*(892)$ satisfies the first condition. The resonances like: ρ^0, Δ, f_0, K^*, Σ^* have very small lifetimes $\tau < 2$ fm while that of the fireball source at RHIC is ~ 10 fm. Because of their short life times the above resonances are quite useful regarding the study of dense and deconfined matter produced at RHIC.

1.5 Event Generator: (HIJING)

In order to understand the data in heavy ion collisions it is necessary to compare the experimental data with the corresponding results from some models. Starting from the particle production till the particle gets detected, we have to simulate all possible interactions taking place in the experiment. There are various models (event generators) which are used to study the particle production and their final properties. Every event generator has its own physics goal and suitable for different energies. Below we have described one of the event generator which we have used in the present

analysis.

HIJING (Heavy Ion Jet INteraction Generator) is a Monte-Carlo event generator for parton and particle production in high energy hadronic and nuclear collisions [75]. In high energy heavy ion collisions, it is expected that hard or semihard parton scatterings with transverse momenta of a few GeV/c will dominate. HIJING is based on QCD-inspired models for multiple jet production with Lund model [76] for jet fragmentation, in particular, to study the jet and mini-jet production together with associated particle in high energy pp, pA and AA collisions. This model incorporates mechanisms such as multiple minijet production, soft excitation, nuclear shadowing of parton distribution functions and jet interactions in dense hadronic matter. HIJING reproduces many inclusive spectra, two particle correlations, and can explain the observed flavor and multiplicity dependence of the average transverse momentum at RHIC energies. But this event generator doesn't include the secondary interaction. The results presented in this thesis have been obtained using HIJING version 1.38.

1.6 Thesis Organization

The work presented in the thesis revolves around some studies of photon and resonance production at RHIC. The central issue has been related to the studies of their multiplicities and some related issues. For the photon multiplicity measurement a preshower multiplicity detector (PMD) has been fabricated and installed by the Indian team at STAR. This detector took data for the first time in RHIC Run4 (2003-2004) corresponding to Au+Au collisions at $\sqrt{s_{NN}}$=200 GeV. The design, fabrication and installation of the PMD and analysis of PMD data constitute a full chapter (Chapter 3) in the thesis. The other major part of the thesis revolves around the study of resonance production at RHIC. Here data regarding Δ and K^* production in d+Au collisions at $\sqrt{s_{NN}}$=200 GeV are looked at. The details of the above analysis constitute another chapter in the thesis.

The thesis is organized as follows. In Chapter 1, an overview of Heavy ion collisions experiments with main results obtained so far are presented in the form of an introduction of the subject. Chapter 2 deals with the STAR experiment at RHIC. Discussions on the PMD and photon multiplicity results are presented in Chapter 3. The analysis of resonance data and results are presented in Chapter 4. The conclusion on the work presented in the thesis is presented in Chapter 5.

Chapter 2

The STAR Experiment

2.1 The RHIC Accelerator Complex

The Relativistic Heavy Ion Collider (RHIC) at Brookhaven National Laboratory (BNL), USA, has been setup to accelerate two counter rotating Au beams and make them collide at a centre-of-mass energy of 200 GeV/nucleon pair. It is capable of accelerating and colliding different combination of ion species such as: $p+p$, $d+Au$, $Au+Au$ over a range of energies (upto 250 GeV for protons and 100 GeV/nucleon for heavy ions). Each ion can be accelerated to nearly the speed of light ($\sim 99.995\%$ of speed of light). RHIC consists of two rings of superconducting magnets, each with a circumference of 3.8 km, which focus and guide the beams. The main components of the magnet system are 288 arc dipoles, 108 insertion dipoles, 276 arc quadruples and 216 insertion quadruples. In addition to the dipoles and quadruples, an inventory of 72 trim quadruples, 288 sextupoles and 492 corrector magnets exists. The arc dipoles with a physical length of 9.728 m are bent with a 4.85 cm sagitta and have a coil aperture of 8 cm in order to accommodate intra-beam scattering. The beam tubes in the magnets are at liquid helium temperatures, with the beams in the arcs separated by 90 cm. The magnets are cooled to a temperature < 4.6 K by circulating super-critical helium supplied by 24.8 kW refrigerators. In order to minimize the

beam losses and the radiation background, an extremely good vacuums of $\sim 10^{-11}$ mbar in the cold bore and $\sim 7 \times 10^{-10}$ mbar in the warm beam tube sections is achieved. RHIC is designed for a Au+ Au luminosity (Ł) of about $2 \times 10^{26} cm^{-2} sec^{-1}$ at the highest energy, while maintaining the potential for future upgrades by an order of magnitude. The luminosity for lighter ions is much higher. For $p + p$ collisions Ł $\sim 10^{31} cm^{-2} sec^{-1}$. Optimal collider performance is achieved by utilization of short bunches colliding head-on to enhance the luminosity while keeping the average current and stored beam energy low. Formation of bunches occurs prior to injection, using the previously existing accelerator (AGS) complex at BNL.

A schematic diagram of the RHIC accelerator complex at BNL including the accelerators used to bring the gold ions upto the RHIC injection energy are displayed in Fig. 2.1. First, the gold ions are accelerated to 15 MeV/nucleon from the Tandem Van de Graaff accelerator. Then the beam is transferred to the Booster Synchrotron and accelerated to 95 MeV/nucleon through the Tandem-to-Booster line. Then the gold ions are transferred to the Alternating Gradient Synchrotron (AGS) and accelerated to 10.8 GeV/nucleon. Finally the gold beams are injected to the RHIC ring. AGS serves as the injector for the RHIC. Once the gold beam is injected to the two counter-rotating rings of RHIC, the bunches of gold ions are accelerated to a maximum energy of 100 GeV/nucleon. The ring with a clock-wise rotating beam is called the Blue ring and the ring with an anti-clock-wise rotating beam is called Yellow ring [80]. The two beams collide at six interaction points inside the RHIC ring. Out of the six interaction points, only four have detectors for carrying out experiments.

2.1.1 The Detectors at RHIC

Near head-on collisions of two Au nuclei at RHIC produce around 1000 particles per unit pseudorapidity (at $|\eta| < 1$). This presents a formidable environment to detect the products of these reactions. The four experiments *viz.* STAR, PHENIX, BRAHMS and PHOBOS, set up at RHIC take various approaches to search for QGP [80].

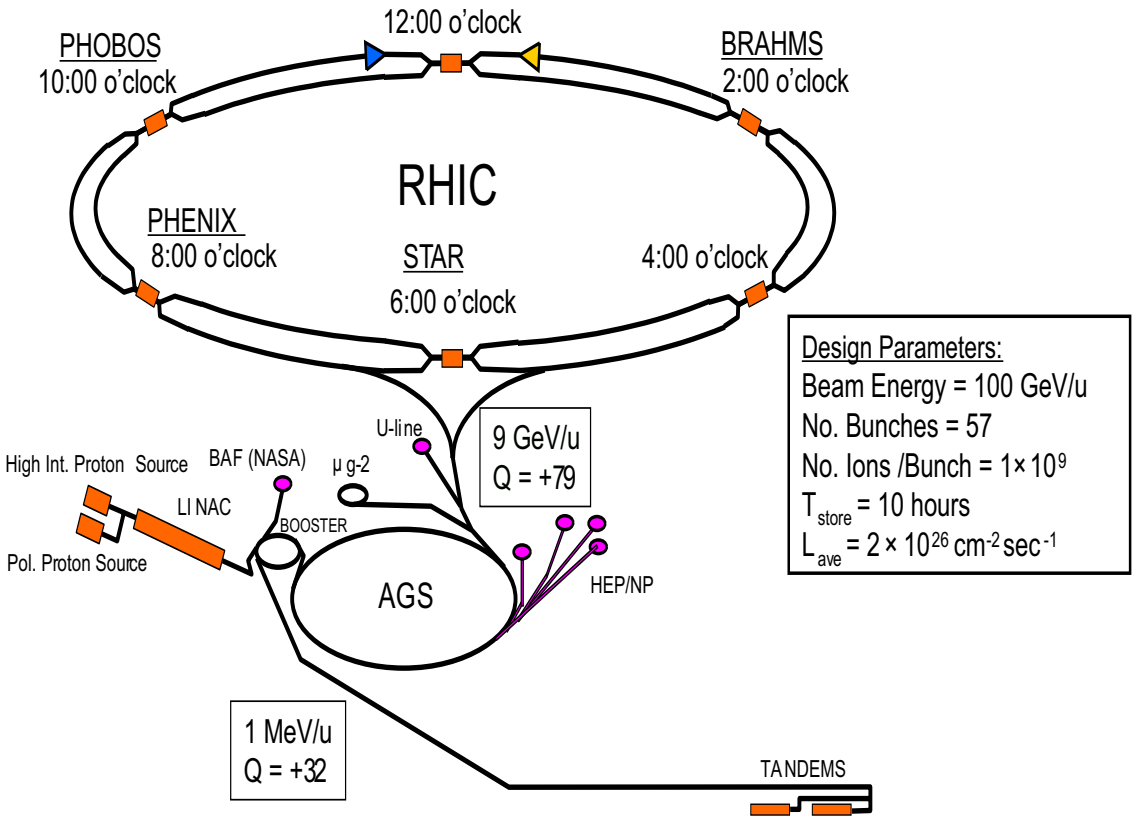

Figure 2.1: The Relativistic Heavy Ion Collider (RHIC) accelerator complex at Brookhaven National Laboratory. Nuclear beams are accelerated from the tandem Van de Graaff, through the transfer line into the AGS Booster and AGS prior to injection into RHIC. Details of the characteristics of proton and Au beams are also indicated after acceleration in each phase

The STAR detector stands for the Solenoidal Tracker At RHIC. The detector has a solenoidal geometry with a large cylindrical Time Projection Chamber (TPC) installed inside a large solenoidal magnet, providing a close to 4π solid angle tracking capability for charged particles from the collision vertex. With three dimensional tracking capability, STAR can identify various charge particle with information on their momenta. Equipped with Calorimeters on both barrel and end cap sections, it is capable of measuring energy of photons and electrons on an $event - by - event$ basis.

"Pioneering High Energy Nuclear Interaction eXperiment", (PHENIX), is designed to measure direct probes of the collisions such as electrons, muons and photons with good momentum and energy resolution. It consists of a large acceptance charged particle detector and four spectrometer arms - a pair of which is used for detecting electrons, photons and hadrons at mid-rapidity, the other pair of spectrometers detecting muons at forward rapidity. There are also additional sub detectors for event characterization, which provide the information about the collision. There is a beam-beam counter which consists of two arrays of quartz Cherenkov telescopes surrounding the beam. There is a multiplicity and vertex detector composed of concentric barrels of silicon strip detectors together with end-caps of Si pad detectors. The last three sets of detectors are used for information regarding event characterization. PHENIX has also electromagnetic calorimeters mounted outside each of the two central arms.

The "Broad RAnge Hadron Magnetic Spectrometers" (BRAHMS) detector consists of a two-arm magnetic spectrometer, one in forward direction for detecting high momentum particles but with small solid angle and other on the side of the collision point at mid-rapidity. Both the arms are movable to variable settings to cover a wide ranges of kinematical regions. BRAHMS is designed to detect charged hadrons over a wide range of rapidity and transverse momentum to study the reaction mechanism. The PHOBOS, smaller of the four detectors (named after a moon of Mars) consists of a two-arm magnetic spectrometer as its central detecting system and a series of silicon detectors surrounding the interaction region. The PHOBOS detector is capable of counting the total number of produced charged particles and study their angular distributions.

2.2 The STAR Experiment

The STAR detector is set up with the aim of measuring many experimental observables in order to study signatures of the QGP phase transition as well as the space-time evolution of the fireball source over a variety of colliding nuclear systems.

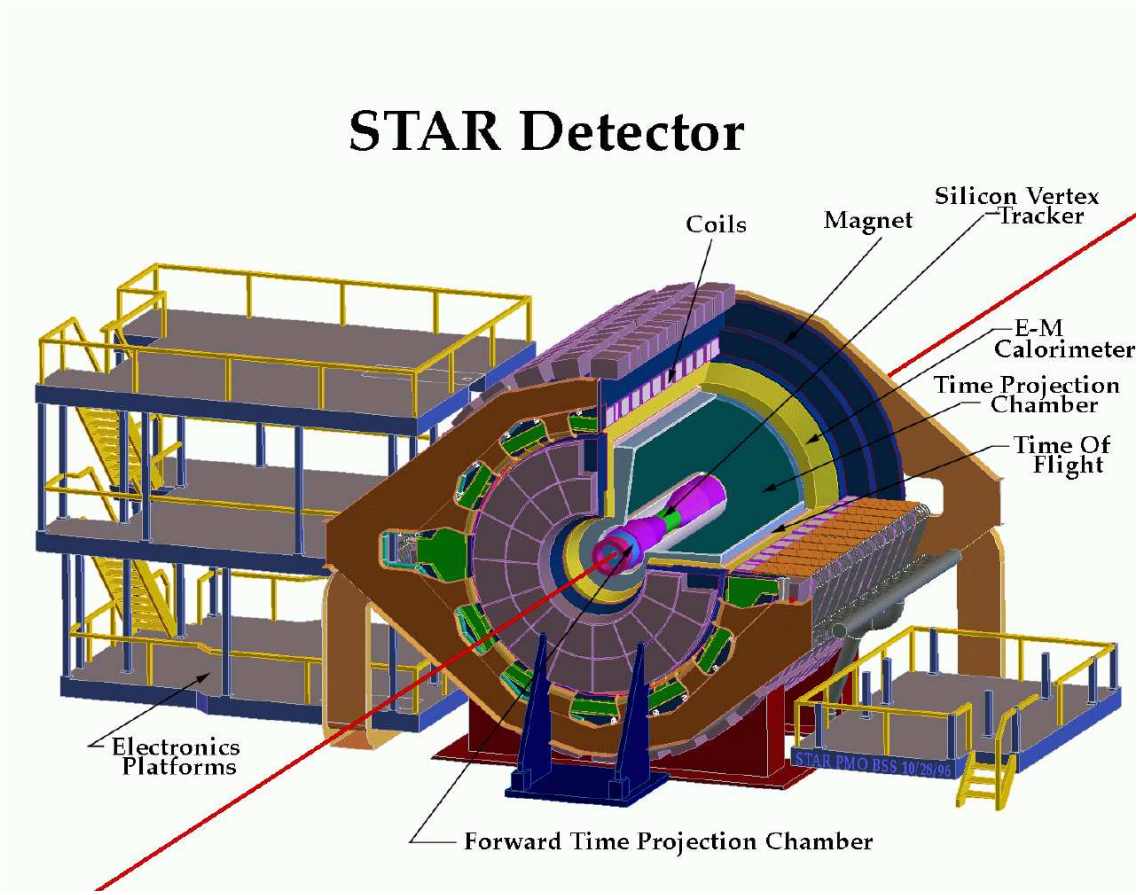

Figure 2.2: Perspective view of the STAR detector, with a cutaway for viewing inner detector systems [81].

More specifically, its primary goal is to obtain a fundamental understanding of the microscopic structure of the hadronic interactions at high densities. In order to accomplish this, STAR was designed primarily for measurement of hadron production over a large solid angle, featuring detector systems for high precision tracking, momentum analysis, and particle identification at the center-of-mass rapidity. The large acceptance of STAR makes it particularly well suited for event-by-event characterizations of heavy ion collisions and for the detection of hadron jets [81]. In addition, STAR is capable of investigating extreme peripheral collisions of nuclei at relativistic energies to study photon and pomeron interactions, which result from the intense

electromagnetic fields of colliding ions and colorless strong interactions, respectively [52].

The layout of the STAR detector [82] is shown in Fig 2.2. It is a large acceptance cylindrical detector system with a complete azimuthal coverage over a central rapidity region. The entire detector system is located within a 0.5 Tesla solenoidal analysing magnet. The solenoidal magnet [83] provides uniform magnetic field for charged particle momentum analysis. A cutaway side view of the STAR detector as configured for the RHIC 2001 run is displayed in Fig. 2.3.

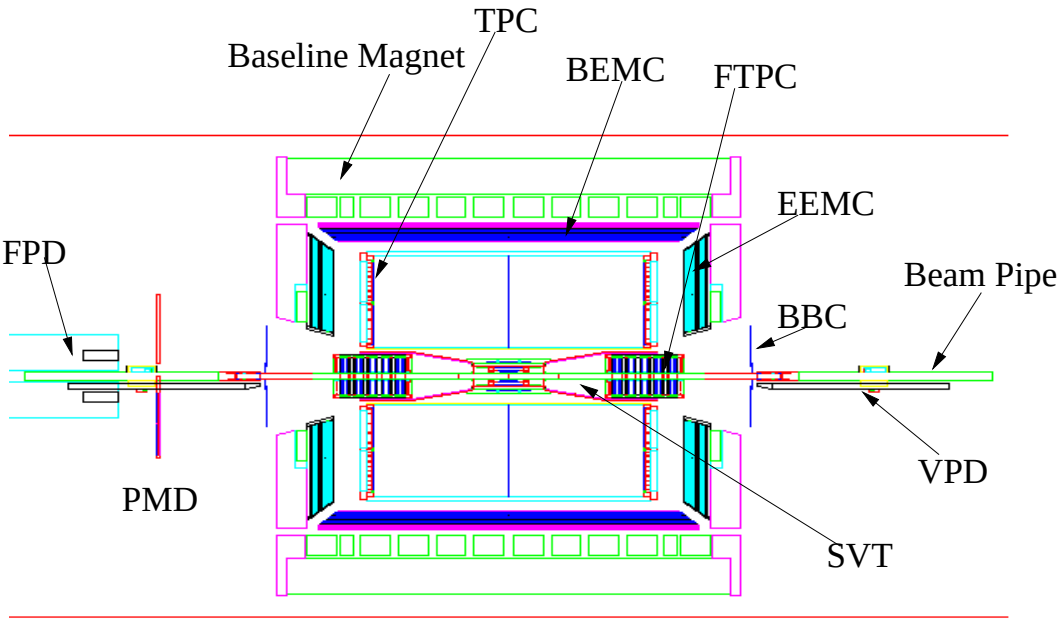

Figure 2.3: Cutway side view of the STAR detector.

STAR consists of several detectors around the main tracking chamber, the Time Projection Chamber (TPC) [84]. The TPC covers the pseudo-rapidity range $|\eta| \leq 1.8$ for tracking of charged particles with full azimuthal coverage ($\Delta\phi = 2\pi$). Charged

particle tracking close to the interaction region is accomplished by a Silicon Vertex Tracker (SVT) [85]. This consists of 216 Silicon Drift Detectors (SDD) arranged in three cylindrical layers at distances of approximately 7, 11 and 15 cm from the beam axis. A fourth layer of SDDs has been installed after 2001 RHIC run for inner tracking. The silicon detectors cover a pseudo-rapidity range $|\eta| \leq 1$ with complete azimuthal symmetry. Silicon tracking close to the interaction allows precision localization of the primary interaction vertex. Also, it enables the reconstruction of very short-lived particles (primarily strange and multi-strange baryons and potentially D-mesons) through secondary vertexing close to the interaction zone. Both the Silicon Vertex Tracker (SVT) and TPC contribute to particle identification using ionization energy loss, with an anticipated combined energy loss resolution (dE/dx) of 7% (σ). The momentum resolution of the SVT and TPC reach a value of δp/p = 0.02 for a majority of the tracks in the TPC. The δp/p resolution improves as the number of hit points along the track increase with drop in the particle momentum because of energy loss [81]. To extend the tracking to the forward region, a radial-drift TPC (Forward Time Projection Chamber) FTPC [86] is installed. It covers $2.5 < |\eta| < 4.0$, with full azimuthal coverage and symmetry on both sides of STAR. To extend the particle identification in STAR to larger momenta over a small solid angle, for identified single-particle spectra at mid-rapidity, a ring imaging Cherenkov detector (RICH) [87] covering $|\eta| < 0.3$ and $\Delta\phi = 0.11\ \pi$ is used. In order to extend the particle identification to higher momentum region, a time-of-flight patch (TOFp) [89], covering $-1 < \eta < 0$ and $\Delta\phi = 0.11\pi$ has also been installed. In addition to the tracking detectors, the Barrel Electromagnetic Calorimeter (BEMC) [91] and End-cap Electromagnetic Calorimeter (EEMC) are used to detect high transverse momentum photons through energy deposition. The EMC's also provide prompt charged particle signals essential to discriminate against pileup tracks in the TPC arising from the other beam crossings.

In the forward region of the STAR experiment, there is another detector, *viz.* the Photon Multiplicity Detector (PMD). The PMD has been installed at a distance of

540 cm from the vertex on the east side of the Wide angle Hall [93]. It covers the pseudorapidity -3.8 $\leq \eta \leq$ -2.4 with full azimuthal coverage ($\Delta\phi = 2\pi$). It measures the multiplicity and spatial distribution of photons on an event-by-event basis. By combining the information from FTPC, the PMD expected to address the following broad topics of physics like: azimuthal anisotropy, fluctuations in multiplicity and eta, and charge to neutral fluctuations (DCC).

The fast detectors that provide input to the trigger system are the Central Trigger Barrel (CTB) at $|\eta| < 1$ and two Zero-Degree Calorimeters (ZDC) located in the forward directions at $\theta < 2$ mrad. The CTB surrounds the outer cylinder of the TPC, and triggers on the flux of charged particles in the mid-rapidity region. The ZDCs are used for determining the energy in neutral particles remaining in the forward directions [81]. A minimum bias trigger was obtained by selecting events with a pulse height larger than that of one neutron in each of the Forward ZDCs, which corresponds to 95 percent of the geometrical cross section.

2.2.1 The Time Projection Chamber (TPC)

The main tracking detector for STAR is a large TPC with complete azimuthal acceptance [82]. The TPC records the tracks of particles, measures their momenta, and identifies the particles by measuring their ionization energy loss (dE/dx). Its acceptance covers $\pm$1.8 units of pseudo-rapidity through the full azimuthal angle. With a magnetic field of 0.5 T, the particles are identified over a momentum range from 100 MeV/c to greater than 1 GeV/c. Particle momenta are measured over a range of 100 MeV/c to 30 GeV/c.

The STAR TPC is shown schematically in Fig. 2.4. It is an empty volume of gas in a well defined uniform electric field of $\sim$ 135 V/cm. The uniform electric field which is required to drift the electrons is defined by a thin conductive Central Membrane (CM) at the center of the TPC with identical concentric field cage cylinders and readout end caps on both sides. The TPC is a fully pixelized drift chamber with

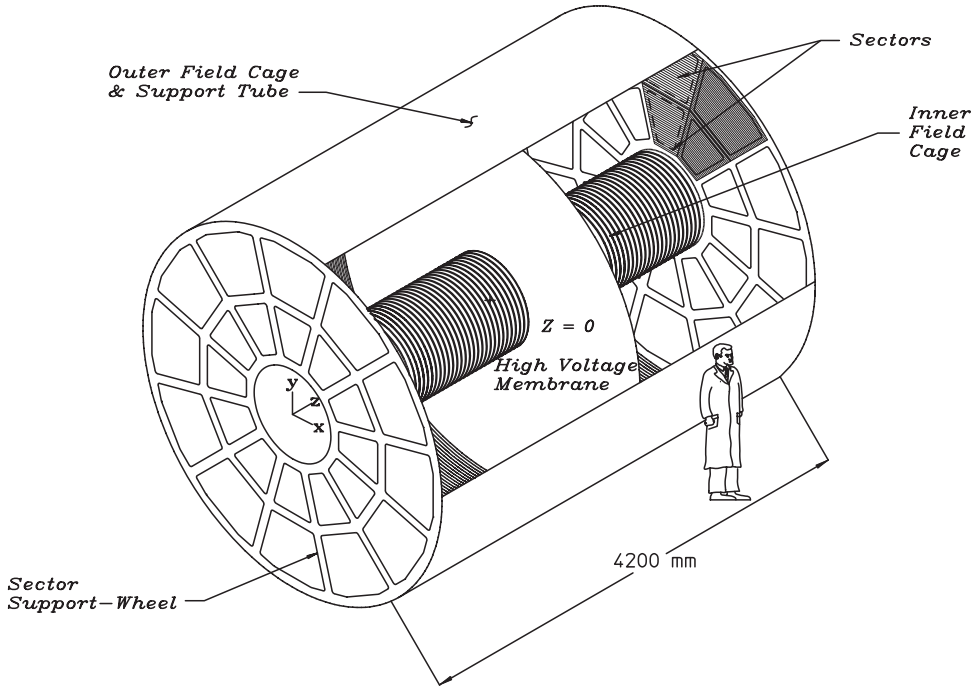

Figure 2.4: The STAR TPC surrounds a beam-beam interaction region at RHIC. The collisions take place at the center of the TPC [84].

Multi-Wire Proportional Chambers (MWPC) at both ends for readout. There are 144,000 readout pads. These give $x - y$ coordinate information and upto 512 time buckets which provide z-position information for each hit. The TPC is filled with P10 gas (10% methane and 90% argon) regulated at 2 mbar above atmospheric pressure. It's primary attribute is a fast drift velocity which peaks at a low electric field [84].

Charged particles can be detected in drift chambers because they ionize the gas along their flight path. The energy required for ionization is very small, typically few keV per cm. When a charged particle traverses the TPC volume, it ionizes gas atoms and molecules in every few tenths of a millimeter along its path and leaving behind a cluster of electrons. Under the influence of an externally applied electric field, the electron clusters drift at a constant average velocity to the readout electronics where

their time of arrival and location are recorded.

The STAR trigger system [96] is a 10 MHz pipelined system which is based on input from the fast detectors to control the event selection for the much slower tracking detectors. The trigger system is functionally divided into different layers, Level 0 being the fastest. Level 1 and Level 2 are slower but they apply more sophisticated constraints on the event selection. STAR has a third level trigger [97] which performs complete online reconstruction of events in a dedicated CPU farm. The level 3 trigger can process central Au+Au collisions at a rate of 50 Hz including simple analysis of physics observables such as particle momentum and rate of energy loss. It includes an online display so that individual events can be visually inspected in real time [81].

At the Data Acquisition (DAQ) stage, raw events containing millions of ADC values are recorded to tapes. Raw data are then reconstructed into physical observables like: hits, tracks, vertices, etc. In the event reconstruction stage, starting from hits with the lowest track density at the outer wall of the TPC, the Kalman Fit method is used to fit the hits in a uniform magnetic field to form a global track. After the reconstruction of global tracks in an event, the trajectories of selected global tracks are extrapolated to the beam axis to be at $x = y = 0$ and thus the z-position of the primary collision vertex of this event is found. Then the global tracks, with a distance of closest approach (DCA) (with respect to the primary vertex), less than 3 cm are chosen for a re-fit by forcing a new track helix ending at the primary vertex. These newly reconstructed helices are called primary tracks [98]. Fig 2.5 shows the beam's eye view of a central Au+Au collision event in the STAR TPC.

2.2.2 Trigger Detectors

The trigger detectors in STAR consist of a Central Trigger Barrel (CTB) and two hadronic calorimeters, at ±18 m from the detector center, close to zero degrees relative to the beam axis. The CTB is an array of scintillator slats arranged in a barrel at the outer diameter of the TPC. Each of the two Zero degree clorimeters (ZDC) subtend

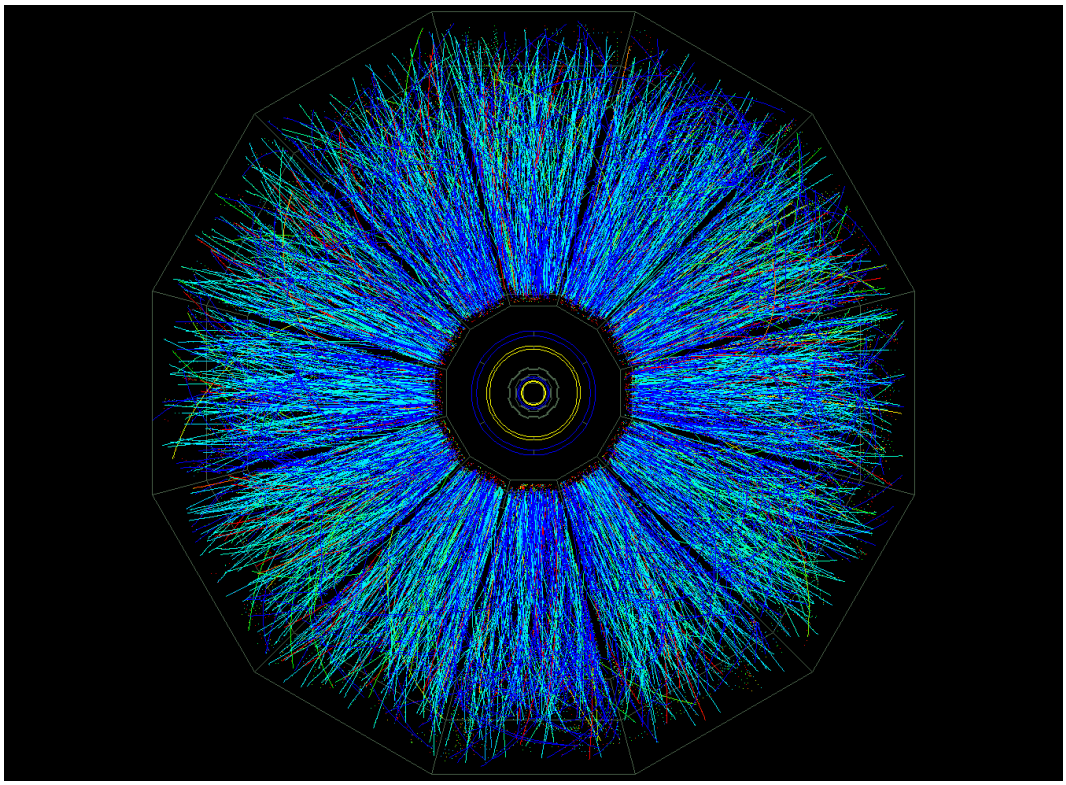

Figure 2.5: Beam's eye view of a central event in the STAR Time Projection Chamber. This event was drawn by the STAR level-3 online display [81].

an angle of $\sim$ 2.5 mrad at the interaction point. These calorimeters are designed to measure energies of neutrons emitted from the nuclear fragments of the spectator matter. In contrast to fixed target experiments, where one can measure energies of all spectator nucleons in the forward direction, at RHIC protons and charged fragments get deflected away from the ZDCs by the dipole magnets in the beamline meant to steer the hadron beams towards the collision point. Thus the ZDC signal is mainly produced by neutrons. Nevertheless, they still provide possibly the best determination of the collision centrality at RHIC, and are used for triggering along with some other observable based on multiplicity.

2.2.3 Forward Time Projection Chamber (FTPC)

In addition to TPC, there are two forward time projection chambers (FTPCs) on both sides of STAR for tracking the charged particles at higher pseudorapidity region. The FTPC is a high resolution radial Time Projection Chamber with circular readout for tracking charged particles within the range of $2.5 < |\eta| < 4.0$ with complete azimuthal coverage. The placement of FTPCs inside the STAR solenoid allows for the determination of the charge of the particles as well as the measurement of their momenta to an accuracy of about 12%. The FTPC has a cylindrical structure, 75 cm in diameter and 120 cm long, with a radial drift field and readout chambers located in five rings on the outer cylinder surface. Each ring has two padrows and is subdivided azimuthally into six readout chambers. The radial drift configuration was chosen to improve the two-track separation in the region close to the beam pipe where the particle density are very high. The field cage is formed by the inner HV-electrode, a thin metalized plastic tube, and the outer cylinder wall at ground potential. The field region at both ends is closed by a planer structure of concentric rings, made of thin aluminum pipes. The Front End Electronics (FEE), which amplifies and digitizes the signals, is mounted on the back of the readout chambers. Each particle trajectory is sampled upto 10 times. The ionization electrons drift to the anode sense wires and the induced signals on the adjacent cathode surface are read out by 9600 pads (each of area $1.6 \times 20\ mm^2$). The FTPCs use a mixture Ar and CO_2 with $Ar : CO_2$::50:50. The reconstruction of the track in FTPCs is done by calculating the track points from the charged distribution measured by the readout electronics. The obtained track points are then grouped to form a track. Using the magnetic field map, upto 10 position measurements per track are then used to fit the momentum [86]. The FTPCs give an almost complete event characterization at forward pseudorapidity region.

2.2.4 Silicon Vertex Tracker (SVT)

The main purpose of the Silicon Vertex Tracker (SVT) is to enhance the primary vertexing, the two-track separation resolution, and the energy loss measurement of the STAR TPC. Apart from this, it also enables the reconstruction of very short-lived particles through secondary vertexing close to the interaction zone. The SVT covers the pseudorapidity range of $|\eta| \leq 1$ with full azimuthal coverage. It is a micro-vertex detector implemented in the novel drift detector technology.

The SVT consists of 216 Silicon Drift Detectors (SDD) containing over 13 million pixels multiplexed onto just 1300 readout channels. The SDDs are arranged in three cylindrical layers at distances of about 7, 11 and 15 cm from the beam axis. For inner tracking a fourth layer has been installed after 2001 RHIC run. A 'pixel' in a drift detector is defined by the anode segmentation in one coordinate and the drift velocity divided by the sampling frequency in the drift direction coordinate. There are 240 anodes for each drift direction. The pixel-like readout of the SDD makes it a good choice for the high multiplicity environment in heavy ion reaction at RHIC. Since there are three layers of SDDs a minimum of three space points are required to determine track parameters when the track is in a uniform magnetic field. Pions having lower transverse momenta ($\sim$ 50 MeV/c) can be detected in the SVT. The TPC has a lower momentum cut off which is about 150 MeV/c. Therefore the 50 MeV/c lower limit of SVT gives a significant enhancement to STAR's capabilities.

There are 24 SVT readout electronics (RDO) boxes mounted, 12 on each side of STAR [85]. The RDO system is split into three functional blocks: (i) a monitoring, power, trigger and slow control interface block (PTB) (ii) an analog-to-digital converter and the data storage block (AMB) and (iii) a fiber optic transfer block (FOB). Each RDO box has 54 analog inputs. Data acquisition is performed at 8/3 of the RHIC strobe frequency (25 MHz). The readout electronics is able to process and send digitized data to DAQ at 100 events/sec.

2.2.5 Silicon Strip Detector (SSD)

The Silicon Strip Detector (SSD) constitutes the fourth layer of the inner tracking system. It has been installed between the SVT and the TPC. The SSD by measuring accurately the two-dimensional hit position and energy loss of charged particles, enhances the tracking capabilities of the STAR detector. Specifically, it helps in improving the extrapolation of TPC tracks through SVT hits and increasing the average number of space points measured near the collision thus increasing the detection efficiency of long-lived meta-stable particles.

The SSD is built into two half barrels allowing a clamshell structure of the ensemble [101]. The total number of readout channels is 4,91,520 which is divided into four sectors, two clamshells shared in two (the p-side and the n-side) of the SSD. The SSD is placed at a distance of 23 cm from the beam axis covering a pseudorapidity range of $|\eta| < 1.2$, which leads to a total required silicon surface close to 1 m^2 [100]. The SSD has 20 space frame carbon beams (ladders) each supporting 16 detection modules. Each module is composed of one double-sided SDD and two hybrid circuits equipped with analogue readout electronics. Two electronics boards, on both ends of each ladder, control the modules sending the analog signals to readout boards located on the TPC wheel.

At the arrival of a trigger, the readout board freezes the data in the Front-End electronics. It then reads all the Front-End channels and sends the data via an optical fiber to the DAQ Receiver board. When the slow control needs to access the Front-End boards, it reconfigures the readout board such that that no trigger is accepted.

2.2.6 Time Of Flight (TOF)

For the direct identification of hadrons produced in the heavy ion collisions at RHIC, a Time Of Flight (TOF) detector has been installed in the STAR experiment. The TOF consists of two separate detector subsystems, one is called Pseudo Vertex Position Detector (pVPD) (the 'start' detector) and other one is called Time of Flight Patch

(TOFp) (the 'stop' detector). The TOFp covers a pseudorapidity range of -1 $< \eta <$ 0 and $\Delta\phi = 0.11\pi$. It extends particle identification up to $p_T \sim 3$ GeV/c for p and $\overline{p}$. The pVPD consists of two identical detector assemblies that are positioned very close to the beam pipe, outside the STAR magnet on both sides. The TOFp sits inside the STAR magnet just outside the TPC. The location of the collision vertex along the beam pipe can be measured by measuring the arrival time of the forward particle pulses at pVPD and TOFp. The average of these two arrival times is the event start time, which with the TOFp stop time, provides time interval measurements. The design of pVPD is based on plastic scintillator readout using photomultiplier tubes with CAMAC-based digitization. There are three pVPD detector elements on each side of STAR at a distance of about 5 m from the intersection region [89]. The start resolution attained by the pVPD is around 24 ps, implying a pVPD single detector resolution of 58 ps. The total time resolution of the system averaged over all detector channels is about 87 ps. This allows a direct $\pi/K/p$ discrimination for momenta up to $\sim$ 1.8 GeV/c and direct $(\pi + K)/p$ discrimination up to $\sim$ 3 GeV/c.

A time-of-flight tray (TOFr) based on multi-gap resistive plate chamber (MRPC) technology has been installed in STAR detector. It consists of a highly segmented cylindrical detector immediately surrounding the TPC. It covers, pseudorapidity range of -1$< \eta <$0 and $\Delta\phi = \pi/30$. For full time-of-flight coverage at STAR, there are 120 trays, 60 each on east and west side. Each individual tray is 2.4 m long, 21.3 cm wide and 8.5 cm deep. Each tray corresponds to 33 MRPCs having 6 readout channels [90].

2.2.7 Forward Pion Detector (FPD)

A Forward Pion Detector (FPD) has been placed at about 7.5 m along z-direction from the interaction region and at a radial distance of about 50 cm from the beam. The FPD consists of a prototype of the Endcap Electromagnetic Calorimeter (pEMC)

together with a Pb-glass detector array. It sits in the east side of the STAR experiment. FPD measures single-spin transverse asymmetry for leading π^0 coming from p+p collisions. It can confirm that, the colliding beams are polarized and can lead to information on the polarization vector at the STAR collision point.

The pEEMC part of the FPD is a lead sampling calorimeter comprised of 21 layers of 5 mm thick Vulcan lead sheets interleaved with 24 layers of 5 mm thick Kururay SCSN-81 plastic scintillator sheets. Total material is approximately of 21 radiation length. The layers are machined into 12 optically isolated tiles in a 3×4 pattern, and thus forming 12 towers. The collection and transportation of the scintillation light is done using 0.83 mm diameter wavelength shifting fibres inserted into "sigma grooves" machined in the scintillator. The other part of the FPD, called the shower maximum detector (SMD), sits behind the sixth layer of pEEMC with about 5 radiation length of pEEMC material in front of it. It is comprised of two orthogonal planes of finely segmented scintillator strips. There are 60 horizontal and 100 vertical strips.

Each strip having a transverse profile approximating an equilateral triangle with an apex-to-base height of 5 mm. Optical isolation was achieved by wrapping individual triangular strips with 50 μm of aluminized mylar. Two adjacent strips have their apexes pointing to the opposite direction [102].

2.2.8 Beam Beam Counter (BBC)

The Beam Beam Counter (BBC) in the STAR experiment provides a crucial p+p collision trigger. It is also a good local luminosity and polarization detector. The BBC is made of 2 sets of 18 small and 18 large, 1 cm thick, hexagonal plastic scintillator tiles. One set is positioned on the STAR east magnetic pole-tip with the other set placed on the west pole-tip. The larger tiles have a diameter four times that of the smaller ones. Aluminized mylar sheets are attached to the front and back surfaces of the hexagonal scintillators to serve as mirrors. Wavelength shifting fibers, inserted in them in the form of loops, collect the scintillation light. The timing difference

between the two counters is used to locate the primary vertex position.

2.2.9 Barrel Electromagnetic Calorimeter (BEMC)

For studying high p_T processes like: jets, leading hadrons, direct photons, heavy quarks etc. a Barrel Electromagnetic Calorimeter (BEMC) has been installed in the STAR experiment. The calorimeter permits the reconstruction of the π^0's from their decay photons at relatively high $p_T \approx$ 25-30 GeV/c. Further, it is capable of identifying single electrons and electron pairs in intense hadron backgrounds from heavy vector mesons, W and Z decays. All these measurements require precise electromagnetic shower reconstruction with high spatial resolution.

The BEMC is a sampling calorimeter using lead and plastic scintillators. The front face of the calorimeter is at a radius of $\approx$ 220 cm from and parallel to the beam axis. The full BEMC includes a total of 120 calorimeter modules, each subtending 6^o in $\Delta\phi$ ($\sim$ 0.1 rad.) and 1.0 unit in $\Delta\eta$. Each module is roughly 26 cm wide and 293 cm long with an active depth of 23.5 cm plus about 6.6 cm structural plates (of which $\sim$ 1.9 cm lies infront of the detector). They are segmented into 40 towers, 2 in ϕ and 20 in η with each tower subtending 0.05 rad in $\Delta\phi$ and 0.05 unit in $\Delta\eta$. The full Calorimeter is physically segmented into a total of 4,800 towers, each of which a projective, pointing back to the center of the interaction diamond. The core of each of the 120 modules consists of a lead-scintillator stack and shower maximum detectors (SMD) situated approximately 5 radiation lengths from the front of the stack. There are 20 layers of 5 mm thick lead, 19 layers of 5 mm thick scintillator and 2 layers of 6 mm thick scintillator. The later thicker scintillator layers are used in the preshower portion of the detector. The SMD is used to provide fine spatial resolution in a calorimeter which has segmentation (towers) significantly larger than an electromagnetic shower size. The total area covered by the BEMC, outside the STAR TPC, is over 60 m^2 with a pseudorapidity range of $|\eta| < 1$. It has a full azimuthal coverage. The calorimeter has a total depth of about 20 radiation length

at $\eta = 0$.

The BEMC electronics includes trigger, readout of phototubes and SMD, high voltage system for phototubes, low voltage power, slow controls functions, calibration controls, and interfaces to the STAR trigger. The BEMC tower data are processed as follows. The phototube signals from the towers are integrated and digitized in the front-end cards on every RHIC crossing. These data are pipelined until Level-0 trigger time, and if a trigger occurs they are transferred to a token-addressable memory in the tower data collector located on the STAR electronics platform to await readout. The signals from the pads of the SMD are amplified with a simple transimpedance amplifier and driver on the front end processing cards before entering an analog pipeline composed of switched capacitor arrays to await the Level-0 trigger. Upon arrival of the Level-0 trigger, the SMD analog signals are queued with multiplexing ratio 80:1 to the 10 bit SMD digitizer. The SMD digitized signals are first available in STAR's level-2 trigger processors in ~ 200 μs, still well ahead of digital information from the TPC [91].

2.2.10 Endcap Electromagnetic Calorimeter (EEMC)

In addition to the BEMC, there is another calorimeter detector *viz* the Endcap Electromagnetic Calorimeter (EEMC) in the STAR experiment. It sits on the west poletip of the STAR detector covering a pseudorapidity range $1.086 \leq \eta \leq 2$, with full azimuthal coverage. Within this acceptance, which is different from that of the BEMC it enhances STAR's capability to detect photons and electromagnetically decaying mesons (π^0, η). It can detect electrons and positrons as well. The EEMC includes a shower maximum detector to discriminate between photons and π^0 or η mesons over a 10-40 GeV energy region. The preshower layers are intended for electron and hadron discrimination.

The EEMC also enhance the triggering capabilities of STAR for jets. Because of the triggering capabilities and with different pseudorapidity coverage as compared to

the BEMC, it is very much useful for the spin physics in polarized p+p collisions. One of the most important goal of this detector is to determine the helicity preference for gluons [$\Delta G(x_g)$] inside a polarized proton, as a function of the fraction x_g of the proton's momentum carried by the gluon.

The EEMC is an annular detector with the full annulus divided into two halves. A standard layer of EEMC consists of Pb/stainless steel laminate followed by a 4 mm thick (Kuraray SCSN-82) plastic scintillator. Each radiator sheet comprises 4.57 mm thick calcium loaded Pb sheets laminated on each face with 0.5 mm stainless steel for a total of $\sim$0.85 radiation length. There are also four specially configured layers providing preshower, postshower and the SMD functions. The tower segmentation of EEMC has been made using megatile construction. Each megatile spans either 6^o or 12^o in azimuthal angle with machined isolation grooves separating each into 12 or 24 trapezoidal tiles respectively. Each 30^o sector of a calorimeter layer contains two 12^o megatiles, aligned flush against tie-rods on each side, and a 6^o "keystone" megatile. A scintillator strip SMD with high position resolution is located at a depth of about five radiation length inside the EEMC. The SMD has been designed to provide the fine granularity, to distinguish the transverse shower profiles characteristic of single photons vs. the close-lying photon pairs coming from π^0 and η^0 decay.

The whole assembly represents 21.4 radiation length at normal incidence and provides a shower energy sampling fraction of 5%. Light from the towers and the scintillator strip SMD is carried through optical fibers to photomultiplier tubes which are mounted on the rear of poletip, outside the STAR magnet.

The EEMC trigger electronics and tower readout are similar to BEMC. Pulse height information from the EEMC towers are digitized in 12-bit flash ADCs for every RHIC beam crossing and stored in digital pipelines for further processing. The STAR Level 0 trigger can compare individual tower ADC values and multi-tower sums to various thresholds and search for simply correlated information from other subdetectors. The primary trigger for high-p_T direct photon and $W^{\pm}$ production correspond to the recording of a very high E_T in a single tower. For events that

pass the trigger, recording of the full ADC information for individual towers provides an adequate energy resolution and dynamic range to include both single Minimum Ionization Particle (MIPs) and electrons upto 150 GeV [92].

2.2.11 Photon Multiplicity Detector (PMD)

A Photon Multiplicity Detector (PMD) has been installed to measure the photon multiplicity in the forward rapidity region of the STAR experiment. It is at a distance of 5.4 m from the vertex on the east side of the STAR. The PMD covers a pseudorapidity range of -3.7 $\leq \eta \leq$ -2.4 with full azimuthal coverage. It measures the multiplicity and spatial distribution of the photons on an event-by-event basis. Using these information on photons together with similar data on charged particle from FTPC, one can study physics, issues related to flow, formation of Disoriented Chiral Condensate (DCC) together with multiplicity fluctuations and pseudorapidity distributions.

The PMD consists of a preshower and a charge particle veto (CPV) plane. Both the planes consist of a large array of hexagonal cells (41,472 in each plane) each in the form of a tiny gas proportional counter. The cells are physically isolated from each other by thin metallic (copper) walls to contain δ-electrons. A honeycomb of 24 $\times$ 24 cells forms a unit module in the form of a rhombus ($\approx$ 254 mm on each side). A set of unit modules are enclosed in a gas-tight chamber called supermodule. The number of unit modules varies from 4 to 9 within a supermodule. The complete detector consists of 24 supermodules (12 in each plane). A 5 mm thick steel support plate and a 15 mm thick lead plate together form a converter of thickness $3X_0$ which is sandwiched between the CPV and the pre-shower planes. The detector uses a mixture of Ar and CO_2 as the sensitive medium in a 70:30 ratio [93]. For a super module, the metallic walls of the honeycomb form a common cathode kept at a large negative potential. The individual anode wires in the cells are kept in the ground potential and are connected to the readout electronics. The GASSIPLEX chip has been used

in the front end electronics (FEE) of the PMD with C-RAMS based readout.

2.2.12 Particle Identification (PID) using dE/dx

The details of the particle production and spectra are best understood when experiments provide results sorted by particle type. In order to provide particle identification, experiments must distinguish between particles with different masses. Charged particles passing through the TPC lose energy via ionization. The total ionized charge collected from each hit on a track is proportional to the energy loss of the particle.

Energy lost in the TPC gas is a valuable tool for identifying particle species. It works especially well for the low momentum particles but as the particle energy rises, the energy loss becomes less mass dependent and it is hard to separate particles with velocities $v > 0.7$c. STAR TPC was designed to be able to separate pions and protons up to 1.2 GeV/c [84]. For a track crossing the entire TPC we obtain 45 dE/dx samples (coming from energy deposition in 45 layers), which are distributed according to the Landau probability distribution. The length over which the particle energy loss is measured is too short to average out ionizations fluctuations. Indeed, the particles lose energy going through the gas in frequent collisions with atoms where a few tens of eV are released [99]. Thus, it is not possible to accurately measure the average dE/dx. Instead, the most probable energy loss is measured. We do this by removing the largest ionization clusters. The truncated mean where a given fraction (about 30%) of the clusters having largest signal are removed. This is an efficient tool to measure the most probable dE/dx. However, fitting the dE/dx distribution including all the clusters associated to a given track has also been found to be more effective. It also allows one to account for the variation of the most probable energy loss with the length of the ionization samples (dx) [84].

For a particle with charge z (in units of e) and speed $\beta = v/c$ passing through a medium with density ρ, the mean energy loss it suffers can be described by the

Bethe-Bloch formula

$$\langle \frac{dE}{dx} \rangle = 2\pi N_0 r_e^2 m_e c^2 \rho \frac{zZ^2}{A\beta^2} [ln \frac{2m_e \gamma^2 v^2 E_M}{I^2} - 2\beta^2] \tag{2.1}$$

where N_0 is Avogadro's number, m_e is mass of the electron, r_e $(= e^2/m_e)$ is the classical electron radius, c is the speed of light, Z is the atomic number of the absorbing material, A is the atomic weight of the absorbing material, $\gamma = 1/\sqrt{1-\beta^2}$, I is the mean excitation energy, and E_M $(= 2m_e c^2 \beta^2/(1-\beta^2))$ is the maximum transferable energy in a single collision.

From the above equation, we can see that different charged particles (electron, pion, kaon, proton and deuteron) with the same momentum p passing through the TPC gas can cause different amount of mean energy loss. Fig. 2.6 shows the energy loss for particles in the TPC as a function of the particle momentum, including both primary and secondary particles. We can see that charged pions and kaons can be identified up to about transverse momentum 0.75 GeV/c and protons and anti-protons can be identified upto 1.1 GeV/c.

In order to precisely identify a particle y, we define the variable $N_{\sigma y}$ (in the case of charged pion we write π in place of y) as

$$N_{\sigma y} = [\frac{dE}{dx}_{meas.} - \langle \frac{dE}{dx} \rangle_y] / [\frac{0.55}{\sqrt{N}} \frac{dE}{dx}_{meas.}] \tag{2.2}$$

in which N is the number of hits for a track in the TPC, $\frac{dE}{dx}_{meas.}$ is the measured energy loss of a track and $\langle \frac{dE}{dx} \rangle_y$ is the mean loss for charged particle as given by y. In order to identify charged pion, kaon, proton and anti-proton, we can have similar definition of $N_{\sigma\pi}, N_{\sigma K}, N_{\sigma p}$and $N_{\sigma \overline{p}}$. One can now apply suitable cuts on the variables $N_{\sigma\pi}$, $N_{\sigma K}$, $N_{\sigma p}$ etc to select different particle species [98].

A specific part of the particle identification is the topological identification of neutral particles, such as the K_s^0 and Λ. These neutral particles can be reconstructed by identifying the secondary vertex, commonly called V_0 vertex, of their charged daughter decay modes, $K_s^0 \rightarrow \pi^+\pi^-$ and $\Lambda \rightarrow p\pi^-$. Similarly, the short lived resonance can be reconstructed through their decay modes.

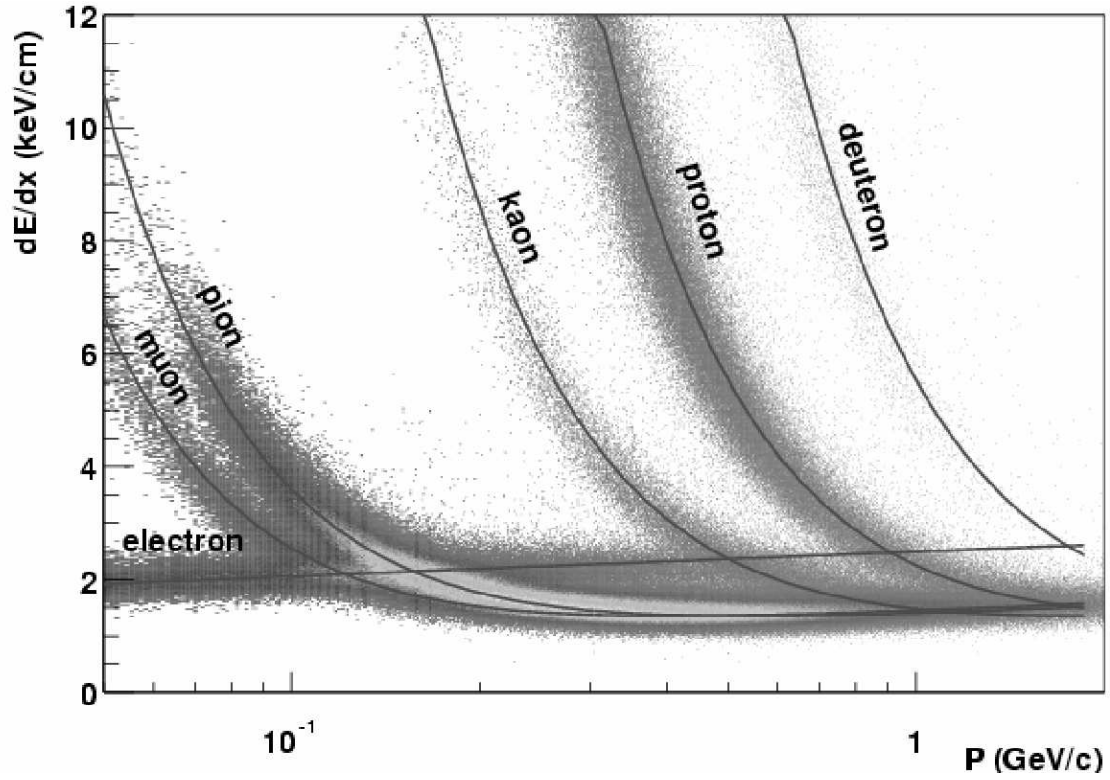

Figure 2.6: The energy loss distribution for primary and secondary particles in the STAR TPC as a function of the p_T of the primary particle [84]. The curves are the Bethe-Bloch function shown in equation 2.1 for different particle species.

2.2.13 Centrality and trigger conditions

The data presented in this analysis are from minimum-bias sample, triggered by a coincidence of signals above threshold in both ZDCs with the RHIC beam crossing. The ZDC threshold was set to ensure efficient detection of single spectator neutrons. The efficiency of the ZDC coincidence trigger for central events was measured using a high-threshold CTB trigger. The CTB was used to trigger on central events, as the signal is correlated to the multiplicity at mid-rapidity. The threshold for the central trigger using the CTB was set to obtain the events with highest CTB signals.

Chapter 3

The Photon Multiplicity Detector (PMD)

3.1 Introduction

The Photon Multiplicity Detector (PMD) has been used to measure the multiplicity of photons in the STAR experiment [93, 103]. It consists of a preshower and a charge particle veto (CPV) plane, both planes separated by a converter consisting of a 15 mm thick Pb plane and a stainless steel support structure in the form of a 5 mm thick plate. The detector has been placed in the forward rapidity (-3.8 $\leq \eta \leq$ -2.4) region, at a distance of 5.4 m from the vertex. In this chapter, a detailed description on the design, fabrication and performance of PMD, using both hadrons and electrons at CERN SPS are presented.

3.2 Physics goals

As has been said earlier, from the measurement of multiplicity and spatial distribution of photons, on an event-by-event basis, together with information obtained from the other detectors, PMD is expected to address the following physics issues:

- determination of the reaction plane and the probes of thermalization via studies of azimuthal anisotropy and flow.
- critical phenomena near the phase boundary leading to fluctuations in global observables like multiplicity (N_γ), and pseudorapidity distributions of photons.
- by measuring the multiplicity of photons (N_γ) and charged particles (N_{ch}) in a common η, ϕ coverage, we can study N_γ to N_{ch} fluctuation and look for signals regarding the formation of disoriented chiral condensates (DCC).

3.3 Photon Detection in a preshower PMD

The basic principle of photon detection using PMD is similar to that of the preshower detectors as used in the WA93 [104] and WA98 [26] experiments at CERN SPS. A schematic diagram showing the basic principle of operation is shown in Fig.3.1. When a high energy photon passes through a converter it produces an electromagnetic shower through the processes of pair production and bremsstrahlung radiation. A sensitive medium consisting of a large honeycomb array of gas proportional counters is placed behind the converter producing signals in one or more honeycomb cells depending on whether a hadron or a photon is incident on the detector.

In addition to the preshower plane, there is a CPV plane with an identical layer of honeycomb detector array placed in front of the converter. The two planes are so arranged that there is an an exact one-to-one correspondence between between individual hexagonal detectors in each plane. As shown in Fig 3.1, when a photon passes through the converter, it produces signals in more than one cell. On the contrary, charged hadrons deposit very little energy producing signals in just about one cell. This is because of their low interaction cross-section with the converter. The signals produce by charged particles are similar to those given by minimum ionizing particles (MIP). Secondly, charged particles produce signals in about one cell in both CPV as well as the preshower planes. On the contrary photons produce

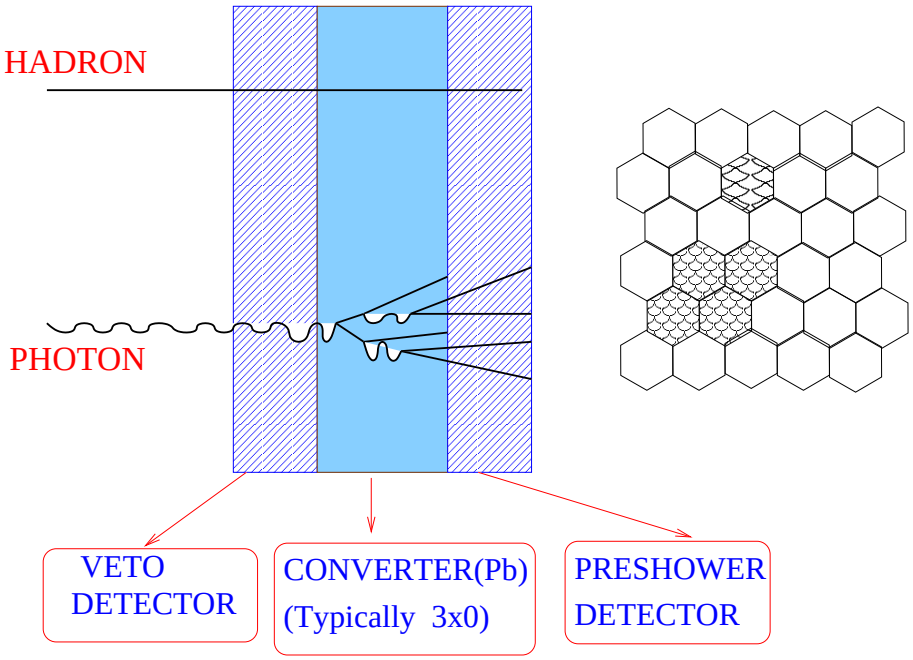

Figure 3.1: Basic principle of a preshower detector

signals in a larger cluster of cells in the preshower plane. These characteristics are used for discriminating between photons and charged particles by using proper energy threshold cut.

The choice of detector technology for use in preshower and veto plane was based on the following considerations:

3.3.1 Preshower Part

- In order to minimize the transverse spread of the shower, the converter should not be too thick and the active volume of the detector should be small and should be placed very close the converter.

- For high granularity the whole detector needed to be segmented into an array of individual cells.

- In oder to avoid cross talks between cells, low energy δ-electrons should be

prevented from traveling from one cell to adjacent cells.

- The technology should be amenable to a modular design with a minimum of dead space at the boundaries between individual detector modules.

- The detecting medium should be insensitive to neutrons. Otherwise, in a hydrogenous medium neutrons produce large signals due to recoil protons, which can mimic a photon signal.

3.3.2 Charge Particle Veto Part

- The charged particles should produce signals confined to one cell so that the occupancy doesn't increase significantly. Spreading of signals to nearby cells would result in a significant probability of vetoing nearby photons and should be avoided.

- The efficiency of charged particle detection should be high (>95 %)so that the same technology can be applied for both preshower and veto planes;

3.4 STAR Photon Multiplicity Detector

The cross-section and layout of the PMD are shown schematically in Fig. 3.2, in which the two detector planes are shown separated by a Pb converter plate, along with corresponding front end electronics (FEE) mounted on the detector planes. As shown in the figure the total cross section of the detector consisting of the two detector planes,two FEE planes, the Pb converter plane and the support SS plane is 110 mm.

The PMD, as mentioned earlier is based on a honeycomb gas proportional chamber design, consisting of a large number of hexagonal cell, each with a wire readout. A great deal of R&D work has been carried out earlier [106] regarding the size of each cell of the honeycomb array and honeycomb material. Good results have been

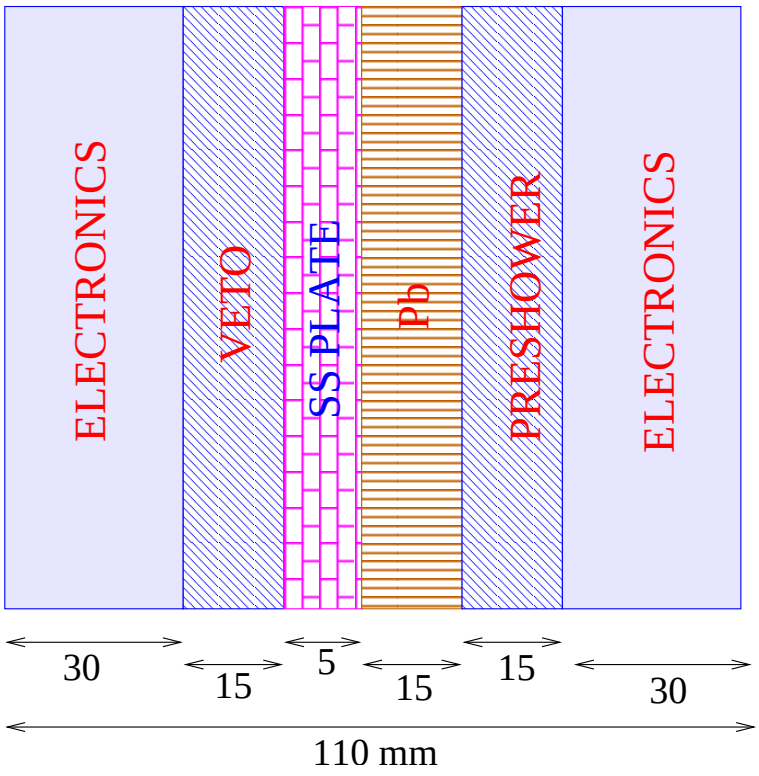

Figure 3.2: A cross-sectional view of PMD showing the veto plane, lead converter and the preshower plane

obtained with a cell size of inner radius 1.06 cm and a gas depth of 8 mm with Cu as the honeycomb material. In the following we present a description on the mechanical design, fabrication and assembly procedures for the detector. This will be followed up by a section on readout. Next we shall be presenting some test beam results obtained with STAR PMD prototypes at CERN SPS. A description on various procedures regarding how to get simulated data in the STAR environment with some simulated results will be presented at the end of the section.

3.4.1 Mechanical Description

The PMD consists the following main mechanical parts:

- modular honeycomb chambers (identical for the preshower and charged particle veto);
- lead converter plates;
- stainless steel support structure

The entire detector has an approximate vertical axis of symmetry, and the two halves can be installed independently. The full PMD, supported on two separate SS plates has been so designed as to enable an independent movement of the two halves which is very essential for service and maintenance of PMD as well as other subdetectors of STAR. The two halves have independent movements to open on two sides of the beam pipe as shown in Fig. 3.3. Regarding mounting, the two halves of the detector are supported on a horizontal girder and hang freely in a vertical position. Each half of the detector can be moved, away from the other, independently, for access in a smooth x-movement on the girder. The girder carrying both halves can move towards or away from the main STAR detector (z-movement), on two further supports mounted on the East side wall of the STAR hall. The support SS plates are isolated from the main girder and movement mechanism. The hanging elements have free swinging pivots, fine adjustments for horizontal motion, and the plane position adjustments for alignment of the detector.

3.4.2 Honeycomb Chambers

The honeycomb is fabricated using 0.2 mm thick ETP grade Cu sheets 8 mm in width. Each cell has been individually made using a die-forming technique. The cells arranged in a matrix of 24×24 in a high precision jig were spot-soldered to form the honeycomb array. The cells were then soldered with a low temperature welding torch at a temperature between 350-400 ^{0}C. The honeycomb array so made was then passed through jig test to check the dimensional tolerances as required. The cells were made with notches at corners for a smooth flow of gas between cells. After the

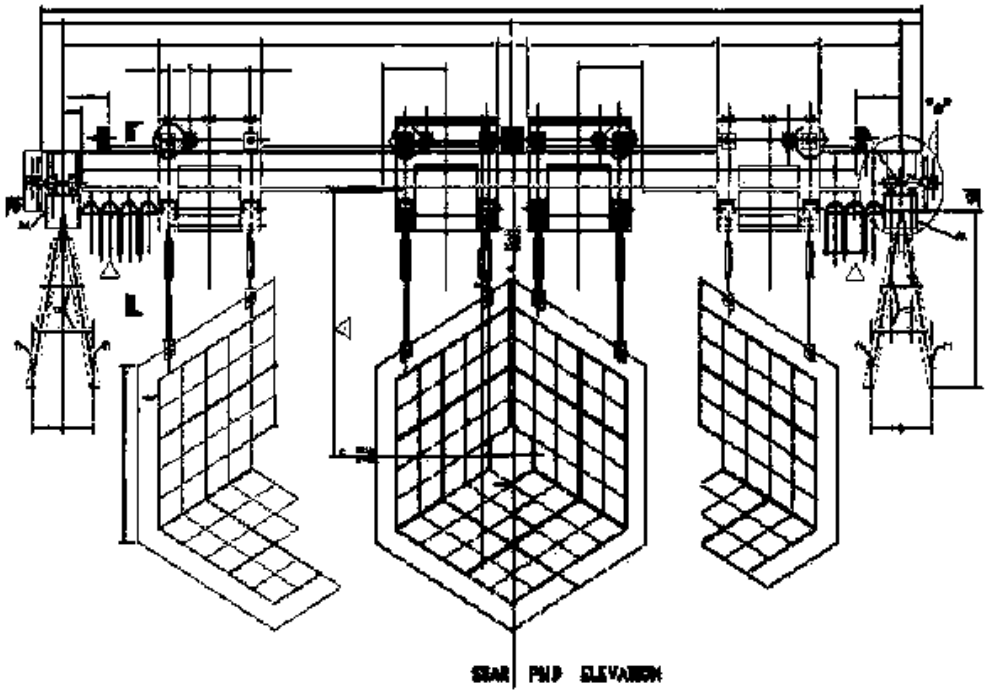

Figure 3.3: Suspension mechanism of the PMD showing movement. The two halves of the PMD are shown separated.

fabrication, the copper honeycombs were cleaned using soap solution and water in an ultrasonic bath. They were then dried in warm air. The dried honeycombs were then coated with high conductivity graphite paint to a thickness of $\sim 10\mu$m. The graphite coating has been done to reduce mainly the after-pulsing which might be generated from delta electrons coming from the honeycomb wall. The schematic of a unit module is shown in Fig. 3.4.

The honeycomb chambers for both preshower and the CPV planes were fabricated in the form of unit modules (UM). Each of the UMs consists of a rhombus of side approx. 260 mm containing a matrix of 24×24 cells as shown in Fig. 3.4. The wall thickness at the boundaries is 0.2 mm which is half that of the walls inside the honeycomb array (0.4 mm). When such arrays are joined together to form a super module (SM), the half-thick boundary walls merge to form a seamless array of hexagonal cells over a the entire area of the SM.

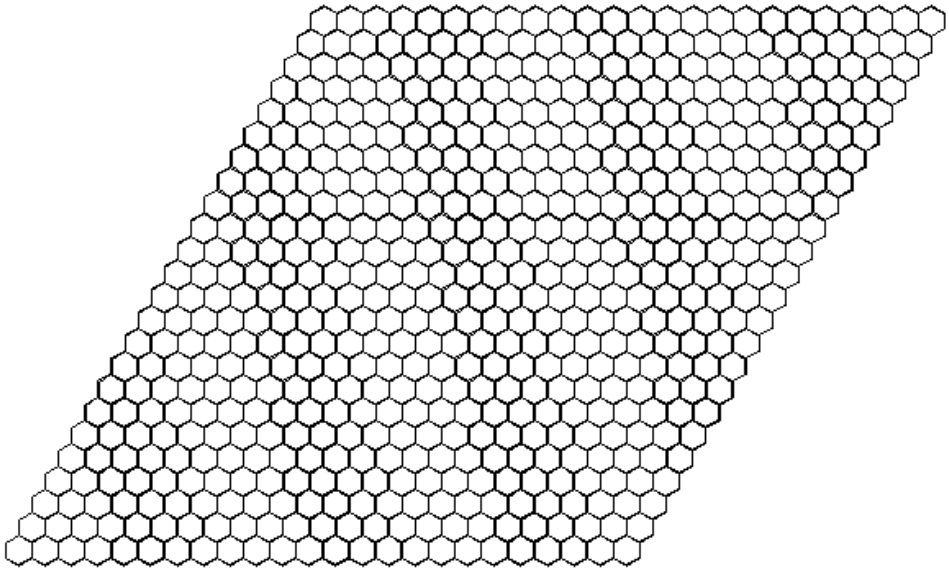

Figure 3.4: Unit module having an array 24 × 24 hexagonal cells.

In order to reduce the dead area due to boundaries and keeping in view the positioning of the PMD as well as other operations as required regarding movement, readout chain combinations etc, different numbers of UMs (4, 5, 6, 8, 9) were combined to form 12 SMs for each plane. Each of the SMs formed a single gas tight enclosure. A photon hit generates a shower resulting in a cluster of cells producing signal in the preshower plane. The number of clusters (in terms of cells fired) corresponds to the number of photons incident on the PMD. Generating larger area SMs from smaller ones helps in reducing the uncertainty in counting of clusters, particularly

those falling at the boundaries of individual UMs.

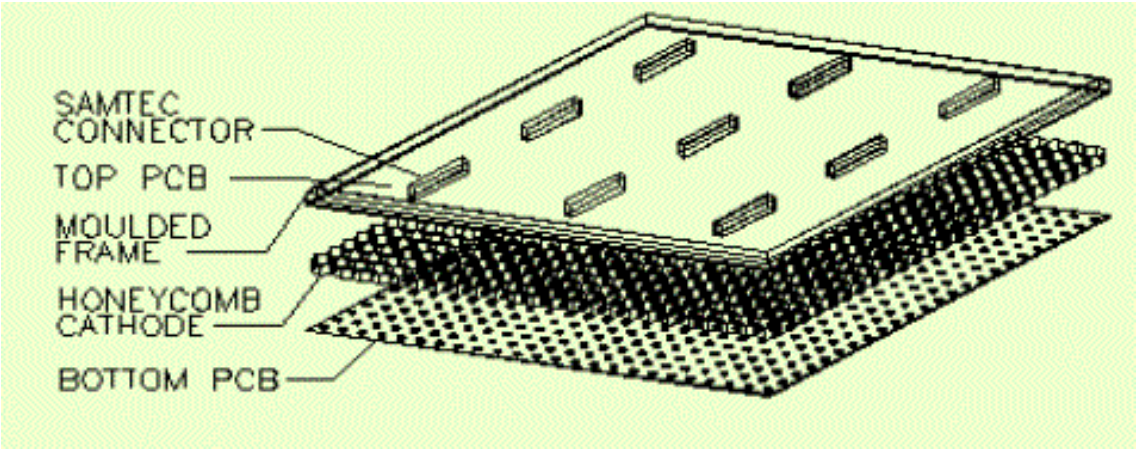

Figure 3.5: Schematic view of components of unit module

Mounting of Front and Back PCBs on a UM

Two Au plated printed circuit boards (PCB) with metalized inner surfaces, having insulation circles of 4 mm diameter formed the front and the back surfaces of the UMs. Each of the solder islands has a Au plated through hole for fixing the anode wire. On the top PCB there are nine sets of signal tracks, each set corresponding to 64 cells. These are grouped to be connected to a 70-pin connector (TFM-135-01-S-D SAMTEC) as shown in Fig. 3.5. The PCB on the bottom side has only soldering islands, for fixing the anode wire.

Each pair of PCBs for a given UM are provided with 24 alignment holes for fixing alignment studs during assembly. A honeycomb is sandwiched between the two PCBs, properly aligned using 24 Cu studs which protrude only 0.5 mm above the PCB surface. A two component Araldite glue was applied at both ends for sealing. The stud heads were then covered with polyamide pads to provide insulation. For a given SM, one of the studs in the whole set of UMs, is used to provide high voltage (HV) connection to the honeycomb walls which act as cathode.

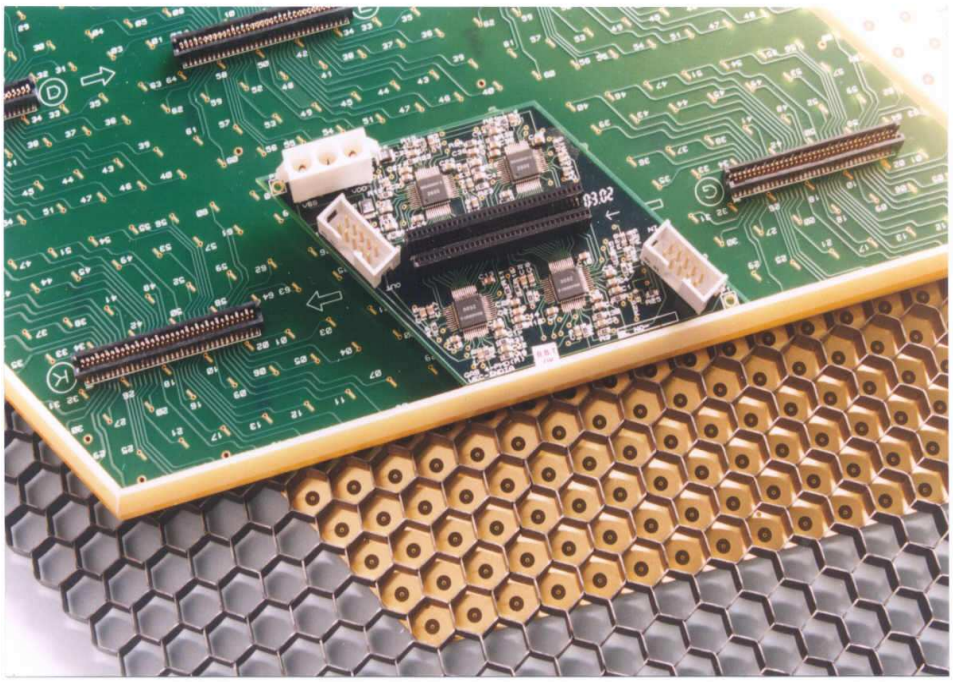

Figure 3.6: Unit module components with electronics board mounted onto the connector

Wire Insertion

Gold plated tungsten wires having 20μm diameter were first cleaned and wound onto a smaller spool. For wiring of the chambers in a given UM, a piece of wire about 0.5 m in length was taken. It was then soldered to one of the solder islands on a given PCB. Using a thin small needle the other end of the wire was inserted through the corresponding holes (for a given cell) to appear on the other side of the chamber. It was not soldered to the solder island immediately. Rather it was again made to go through holes for another nearby cell to appear on the starting side. Now the wire was made to go through a small pulley lifting a 20g weight. This resulted in a tension ($\sim$ 30% of its elestic limit) in the wire. In this condition the wire was soldered on

the soldering islands on the backside. This procedure was repeated till wiring of the whole module was completed.

After completion of wire soldering all the solder joints of the whole UM were inspected using a high resolution video magnifier. In case there were any defects, the soldering was repaired at this stage. After this all the soldered joints were tested for any dry soldering using a milli-ohmmeter. A resistance of 3-4 Ω indicated the soldering to be good. In order to make the chamber gas-tight, the holes, where the wires emerged were sealed with tiny amounts of fast-setting epoxy. The excess wire, between solder islands on difference cells, was cut and removed using a DC HV spark between the sharp edge of a blade and the solder joints. Before cutting the wire an adhesive tape was put on the wire only exposing the ends at solder joints. Removing the adhesive tape, after wire cutting, resulted in a smooth removal of the excess wire.

3.4.3 Assembly of Supermodule

As mentioned earlier, a set of SMs (12 in each plane) were made, each using a set of UMs, the number of UMs being different for different SMs which was dependent upon the SM position and PMD readout. The arrangement of SMs in one of the PMD planes is shown in Fig 3.7. Each SM is seen to have a group of UMs as shown in the figure. The other plane at the back has exactly the same arrangement so that there is a one-to-one correspondence between SMs in both planes.

The UMs in a given SM were bonded in a gas-tight enclosure made of 3 mm thick FR4 grade glass epoxy sheet with a 6 mm thick and 30 mm high aluminum boundary wall. Through holes are provided at the corners of the super module for fixing onto the support plate. The basic steps followed for the assembly of SMs were as follows.

- The SM chamber was prepared by attaching the boundary wall to a G10 bottom plate with screws and epoxy.
- A base frame made of aluminum having a similar size as the super module was

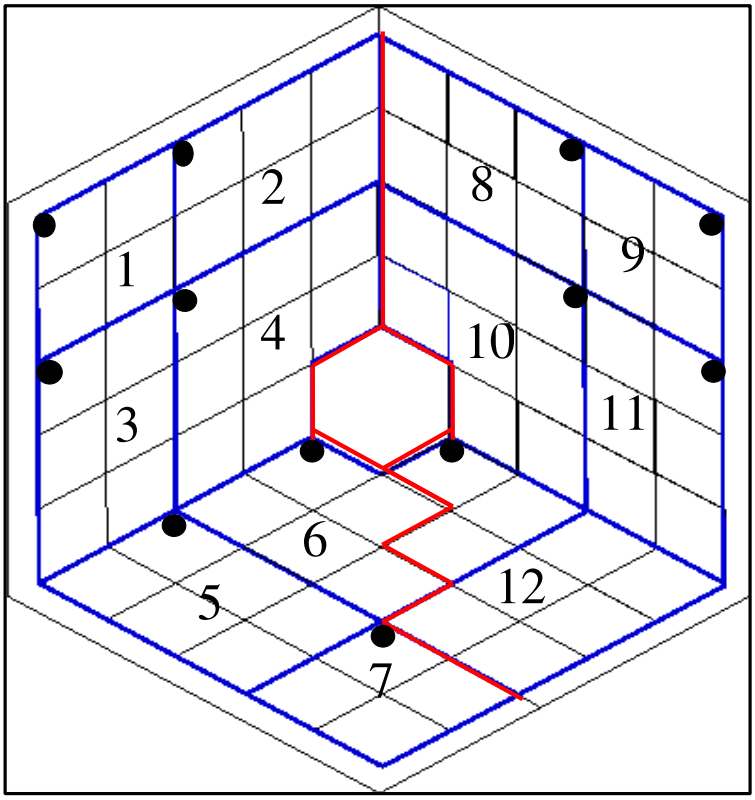

Figure 3.7: Layout of the detector super modules. The black dots in each super module indicates the corner position of the super modules, where the cell numbering starts.

fixed to the bottom plate to retain the planarity of the bottom sheet during further operation.

- The chamber was then placed on a planar granite table. The unit modules were then placed inside the super module enclosure, leaving a 1 mm gap on all sides to accommodate general tolerance. This also provided insulation between the honeycomb cathode and the boundary.

- The contact area between the outermost boundaries of the UMs and the inner boundary wall of the SM enclosure was filled with silicone adhesive.

- A small enclosure containing one SHV connector, an HV limiting resistor (2.2 MΩ) and a decoupling capacitor (2.2 nF) was fixed at one corner of an SM which, closer to the HV tapping point, for applying the required HV.

3.4.4 Support Structure and Converter Plates

The support structure has two parts: (a) the support plates, and (b) the suspension and movement mechanisms. We have already discussed about the suspension mechanism of the PMD which gives one the freedom move and position each half of the PMD in a smooth manner. In view of this we present below only some discussions on the support structure and converter mounting.

support plate

As we had mentioned earlier, PMD has two parts on both sides of the beamline. A 5 mm thick SS plate is used to support the lead converter plates and the SMs in each half of the PMD. The SS plate has tapped holes for screws corresponding to hole positions in the Pb converter plates and in the SMs. The complete support plate has thus two asymmetrical pieces which when joined together form a regular hexagon. The SS plate on the South side has 5 SMs in each plane (10 in total) while the one on North has 7 SMs in each PMD plane (14 SMs in total).

Converter plate

Rhombus shaped Pb converter plates, 265 mm on each side, were machined to be fixed on the SS support plate with four holes at four corners. The holes are used for bolting up the converter plates on the support SS plane. The above size for the Pb plates has been selected because, (a) an integral number of identical lead plates of this size fill the area of an SM, and (b) each piece weighs around 10 kg which is convenient to handle. The Pb plates have been painted to avoid direct physical contact during handling.

3.5 Front-End Electronics (FEE)

The front-end electronics (FEE) used to process the PMD signals are based on the 16-channel GASSIPLEX chips [107]. The FEE system consists of basically three basic units viz a FEE board with four GASSIPLEX chips, a translator board and a buffer board. Discussions on these are given below.

Signals from each cell of the PMD are processed by the analog CMOS VLSI front-end electronics chip GASSIPLEX. It consists of 16 multiplexed channels. Each channel consists of a charge sensitive amplifier, a switchable filter, a shaping amplifier and a Track/Hold stage to store charges in a capacitor. The low-noise amplifier is characterized by an integration time of about 800 ns. The new version of GASSIPLEX, based on 0.7 μm technology, has a peaking time adjustable within 1-1.2 μs. The dynamic range of the new version for negative input signal is 1.1 V which corresponds to about 300 fC of charge which has been found to be adequate for our preshower applications [106].

Corresponding to each UM there are nine FEE boards each with 4-GASSIPLEX chips connected to 64 channels of the detector. A picture of a 4-chip FEE board is shown in Fig. 3.6. The FEE board has also a rhombus shaped to match with the layout of an 8 cells×8 cells block on the PCB. A 70-pin connector at the center of the board connects the FEE board with the chamber PCB. The shape and size of each FEE board are such that when all of them are fixed on the SM/PMD the total surface area is completely covered with no overlap between them.

A set of two diode protection boards is mounted on a 70-pin connector at the center of the FEE board to protect the GASSIPLEX boards from the sparks. There are two sets of 10 pin FRC connectors for daisy-chaining of the control signals and analog output. Another set of AMP 3 pin power connector is there on the board for daisy-chaining of the low voltage bias for the chip. The data signals and the operating low voltages are carried through daisy-chains.

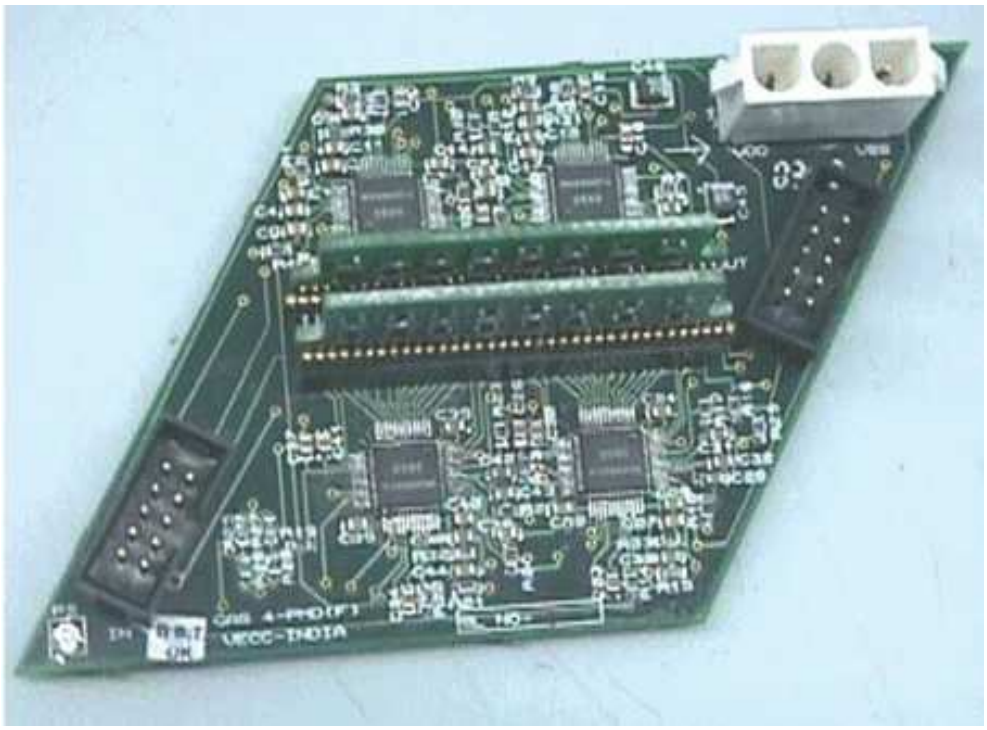

Figure 3.8: Layout of the top layer of the four-chip FEE board

The levels of the fast logic NIM signals as required for readout need to be readjusted to match the requirements of the GASSIPLEX chips. A small translator board is provided to carry out this. A buffer amplifier is required for transmission of analog multiplexed signal trains to the readout modules with provisions for baseline adjustment (for either polarities). The layout of the top layer of the 4-chip FEE board is shown in Fig.3.8.

3.6 Readout for PMD

3.6.1 Pre-trigger and Timing Diagram of the PMD

After the RHIC collision takes place, it is expected that we will get pretrigger after 500 ns and there will be level zero (L0) trigger [96] after 1.1 μs. As soon as the pre-trigger arrives at PMD DAQ, a BUSY signal will be sent and after 814 ns, a

T/H will be sent to the FEE. If L0 does not arrive within the pre-defined time, a clear (CLR) signal is sent to clear both the T/H and BUSY signals. Since the base recovery time of FEE is 4.5 μs, the BUSY has to be cleared after 4.5 μs. If L0 arrives within the pre-defined time then both a T/H and a BUSY signal are sent. For this L0, one needs to check whether pre-trigger exists or not. If it exists, then a trigger is sent to the sequencer which in turn generates the CLOCK (CLK), T/H, CLEAR (CLR), BUSY and CONV signals. The CLK, T/H and CLR are FANed and sent to all readout chains. The CONV signal is passed on, through a delay module, to the C-RAMS. The C-RAMS converts the data and sends a Ready signal to the sequencer after which the readout starts. After the readout a FEE CLR appears when the software BUSY is withdrawn. On the other hand, if pre-trigger doesn't exist by the time L0 arrives, then both T/H and BUSY are cleared. The timing diagram of the generation of pre-trigger and handling of GASSIPLEX signals is shown in Fig. 3.9.

3.6.2 C-RAMS Scheme

The analog signals are read out using C-RAMS modules. This kind of readout already have been used in STAR RICH detector [88]. In the present case there are 82,944 cells (channel) to be readout for PMD. One block of a C-RAM can take at the most 1728 channels which can be connected to a single chain. In such a case 24 C-RAMs are needed. In our case one block of C-RAMs was used to read 24 chains (each chain having 1728 channels) of the preshower plane the other block in the C-RAMs reading an identical number of chains from the CPV plane. The readout chains for both planes of PMD were so arranged that both halves could be independently maneuvered. The total time of digitization and transfer to the buffer memory is about 4 ms at the rate of 0.5 MHz. The 24 C-RAMS used have been put in two VME crates, each crate equipped with a sequencer and Trigger Clock Receiver (TCR) module. Each crate had a MVME2306 Motorola CPU, to read the data from the C-RAMS, buffer them for L2 synchronization. The above CPU is provided with an optical link to the STAR

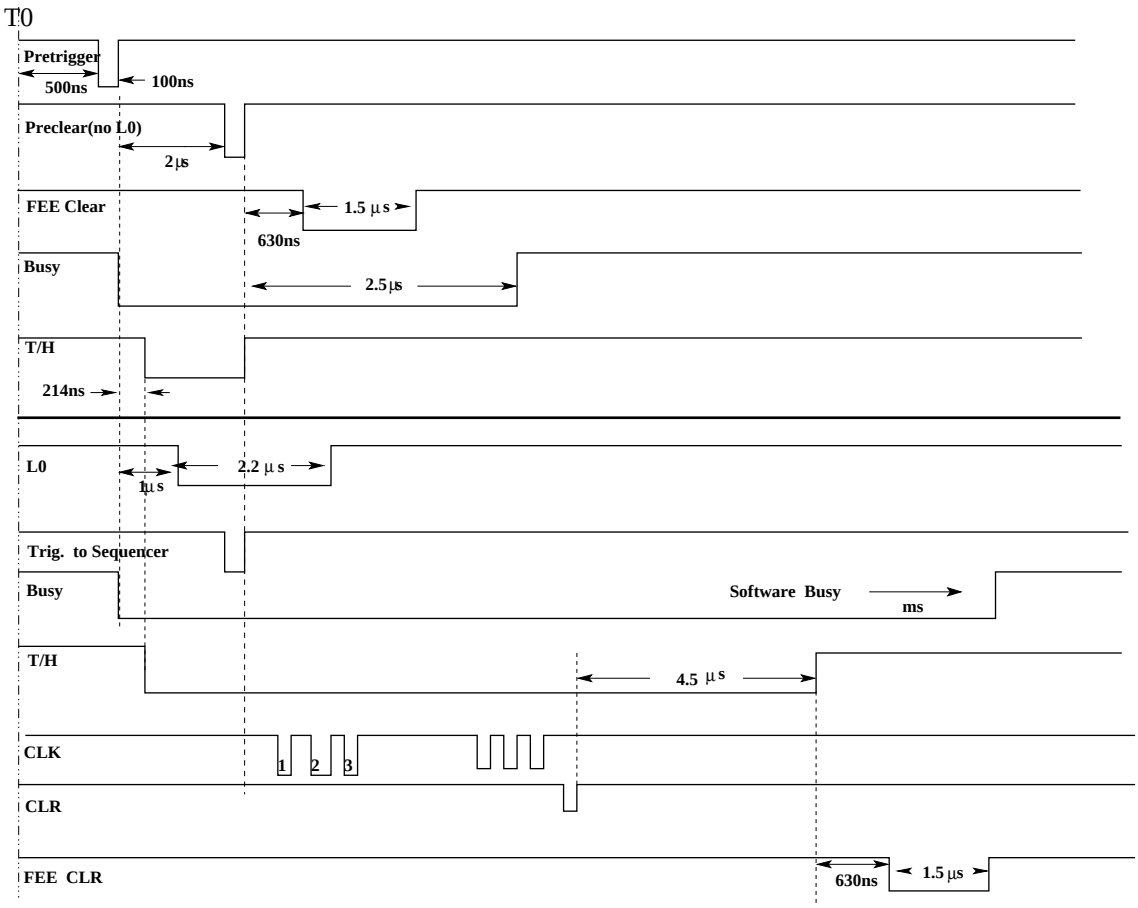

Figure 3.9: Timing diagram for pre-trigger and L0 validation

DAQ system with a similar CPU.

3.7 Gas Flow Control for PMD

Based on earlier test data on PMD at CERN (PS and SPS) it was decided to use a mixture of Ar and CO_2 in the 70:30 ratio at a pressure of 1 bar. With this mixture a good proportionality for charge particle detection was observed at applied voltages between 1400 to 1600 V [106]. In view of this a two component gas-flow and control system has been designed. This gas flow control system, for the PMD, consists of a single pass design that distributes gas to all the super modules. A schematic diagram

of the PMD gas system is shown in Fig. 3.10.

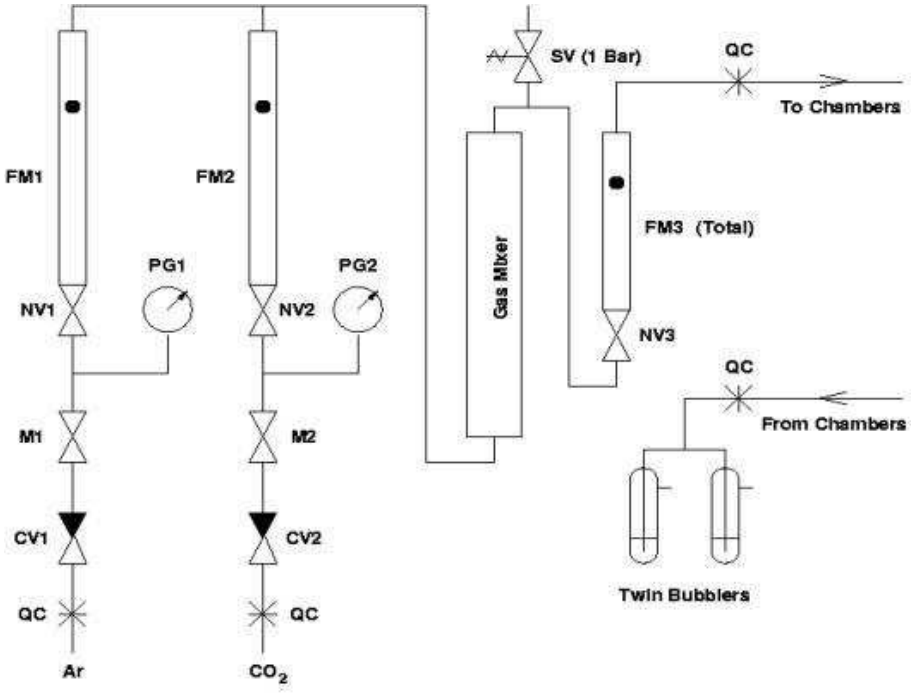

Figure 3.10: Schematic diagram of PMD gas flow system

In the gas flow system, individual gas components (Ar and CO_2) enter the corresponding flow meters through the one way circle seal check valves (CV1, CV2) and manual control valves (M1, M2). Flow rates can be adjusted by the two needle valves (NV1, NV2) located on the bottom part of the flow meter. The gases enter the gas mixing tube and due to a concentric tube arrangement inside the mixer, their flow direction changes thrice for achieving the required mixing. In the case of excess pressure, above 1 bar, in order to protect the chambers, there is a safety valve at the exit of the mixing tube to vent out the excess gas. Flow meter FM3 indicates the total flow of mixed gases into the chambers. The normal flow rates used are about 30 liters/hour. The gas which returns from the chambers is vented out after passing through two bubblers.

3.8 Some Physical Parameters of PMD

For making the PMD, several important parameters like detector acceptance, converter thickness, granularity of the detector, operating voltage range, operating gas mixture, response to hadrons and photons need to be optimized. Out of these, granularity and positioning of the detector are decided by the physics requirements. On the other hand most of the other parameters are fixed based on experimental test beam data with electrons and hadron beams obtained on small prototypes at CERN SPS [106]. These parameters have been optimized for handling the large particle multiplicity at RHIC.

3.8.1 Converter Thickness and Cell Size

In the preshower detector, the converter plays an important role. As we increase the thickness of the converter, there will be an increase in the preshower signal for an electromagnetic particle. But such an increase in converter thickness results in a transverse spread of the shower size which increases the multihit probability. In view of this and based on our earlier experiences in [104, 26], it was decided to use a $3X_0$ thick Pb converter for the preshower plane. This thickness maps to about 1.5 cm of Pb.

The granularity of the STAR PMD was optimized by taking the maximum particle multiplicity in an event. A uniform cell size of 1 cm^2 has been selected for both the preshower and veto plane of the PMD [106].

3.8.2 Acceptance

As mentioned earlier, the PMD covers a pseudorapidity range of -3.7 $\leq \eta \leq$ -2.4 with almost full azimuthal coverage at a distance of 540 cm from the interaction point. The azimuthal (ϕ) coverage of PMD as a function of pseudorapidity (η) is shown in Fig. 3.11. This has been obtained by randomly generating tracks within an η range

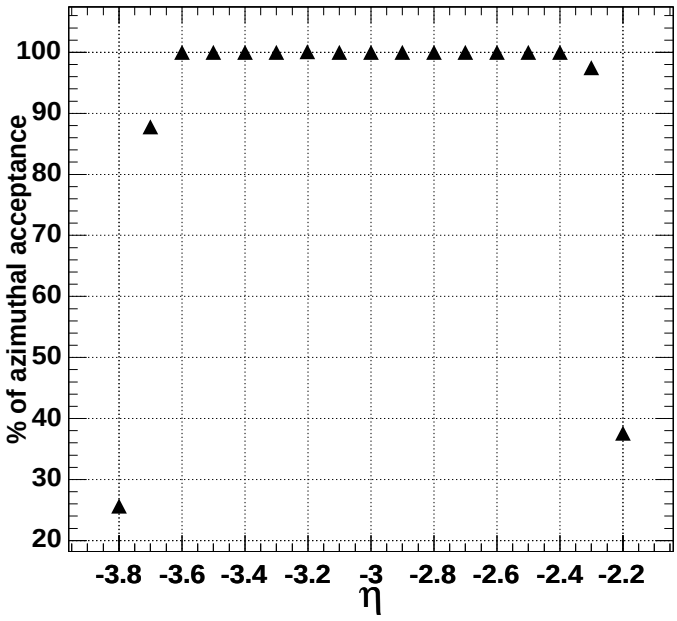

Figure 3.11: Azimuthal acceptance (ϕ) of PMD as a function of pseudorapidity (η)

of -2 to -3.9 which correspond to the limiting η values with full ϕ (i.e. 2π). η=-3.9 corresponds to the circle inscribed inside the hexagonal opening at the center while η=-2 corresponds to a circle circumscribing the hexagonal outer edge of the PMD. The acceptance is calculated taking the percentage of tracks falling within the PMD azimuthal acceptance in a particular η window.

As can be seen, PMD has 100% ϕ-acceptance within the η range between -3.6 to -2.4. For an η bin -3.7 $\leq \eta \leq$ -3.6 the ϕ-acceptance goes down to $\sim$ 87%. For our analysis, we use the η-region where PMD has full ϕ-acceptance.

3.8.3 Photon Conversion Efficiency

When an energetic photon passes through a converter, it produces a shower the shower particles depositing their energy in a cluster of PMD cells. If the energy of the incident photon is very low, it looses all its energy within the converter and doesn't reach the

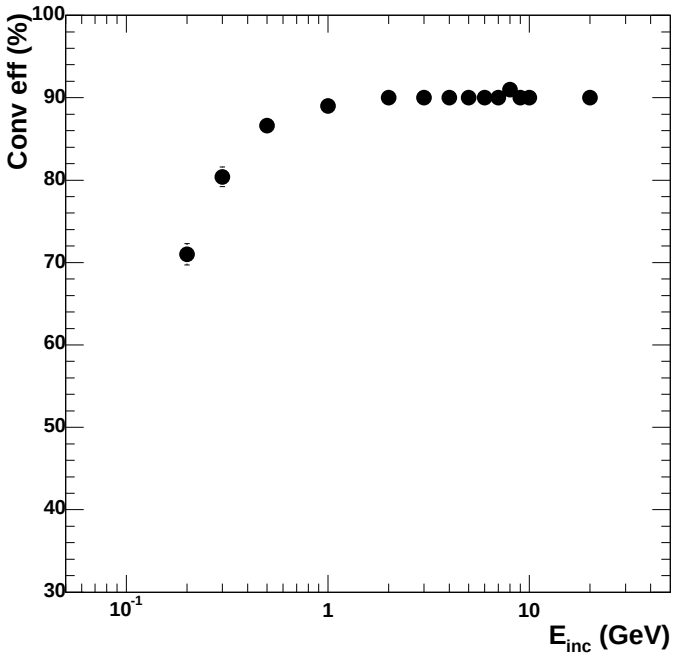

Figure 3.12: Photon conversion efficiency as a function of photon incident energy.

preshower plane. If the energy is high, the photon gets converted forming shower particles that come out of the converter producing signals in a detecting medium following the converter. The photon conversion efficiency is thus defined as the ratio of the number of photons get converted to the number of incident photons. This photon conversion efficiency as a function incident energy with a composite converter consisting of $3X_0$ thick Pb and an $0.34X_0$ thick iron structure, is shown in Fig. 3.12. The above results have been obtained using single photons as inputs to a GEANT [111] simulation.

From the figure, one can see that the conversion efficiency for photons with energy >1 GeV, is ∼90%. For 200 MeV photons, it has a value of about 70 %. It increases steadily with incident photon energy upto 1 GeV. Above an incident photon energy ∼ 1 GeV, the conversion efficiency has been found to be independent of incident photon energy.

3.8.4 Test Results/ Performance of the PMD

Detailed tests have been performed with STAR PMD prototypes using pion beams in the range of 3 to 30 GeV at the CERN PS for the study of the response to minimum ionizing particles (MIP)/charged hadrons. For preshower applications, the performance of the detector characteristics were studied using electron beams with various converter (Pb) thicknesses. The gas mixture, and operating bias voltage were the other two parameters which were optimized using the above data [93]. Some of these results are presented below.

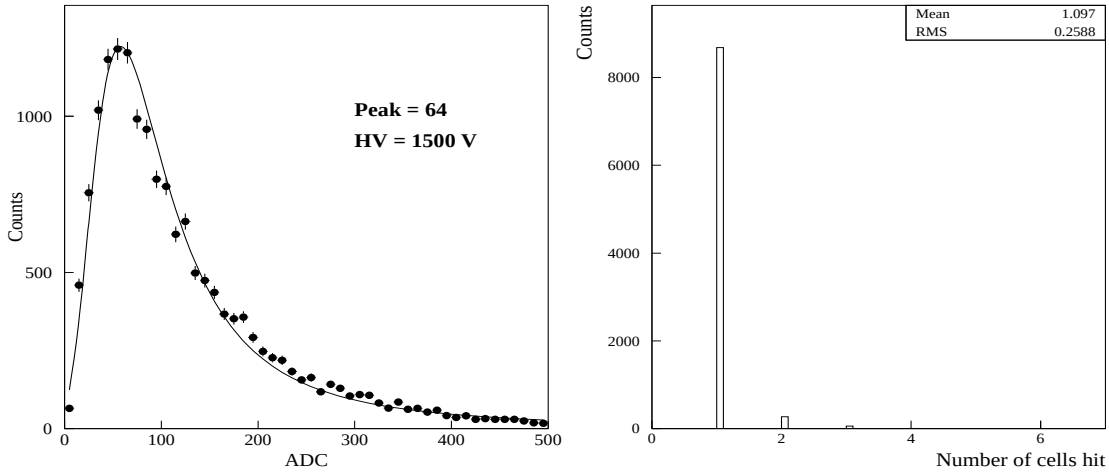

Figure 3.13: (left) Typical MIP spectra for cells with -1500 V, fitted with Landau distribution and (right) distribution of number of cells hit by MIP.

Response to charged particles

Figure 3.13 (left) shows a typical pulse height spectrum, taken with a STAR PMD prototype, with 5 GeV pions, at an applied voltage of -1500 V. The spectrum has been fitted with a Landau distribution characteristic of a MIP. Fig. 3.13 (right) shows a distribution of the number of cells hit by a MIP. One can see the most of the signal is confined to one cell which satisfies one of the main design goals of the detector.

The efficiency for charged particles detection and the cell to cell gain variation for the prototype has been determined for a number of cells chosen randomly in the prototype. The detection efficiency corresponds to the fraction of charged particles detected with respect to their incident number. The cell to cell gain variation or the so called relative gain is defined as the ratio of the mean pulse height in a cell to the value of the mean pulse height taken over a large number of cells. Fig. 3.14 (top) shows the histogram of the relative gains for a total of 40 cells. As shown in the figure, the overall gain of the prototype chamber was found to be quite uniform, the distribution showing a narrow width with a $\sigma \sim 6\%$. The bottom pannel in Fig. 3.14 shows the efficiency measured over the same 40 cells. The average value of the efficiency was found to be 90%. The efficiency was also found to be uniform over the cross-section of a single cell, varying within a narrow range of 93-99%, the lower value being at the edges of the cell [106].

Preshower characteristics

Preshower behavior is characterised by: (i) the transverse spread of the shower, which is given by the size of the cluster of hit cells, and (ii) by the energy deposition expressed in terms of the cluster signal (i.e. the total signal in all the hit cells, in ADC units). These have been determined using 1-6 GeV electrons and a $3X_0$ thick Pb converter kept in front of the prototype detector.

A typical preshower spread for 3 GeV electrons is shown in left panel of Fig. 3.15. One can see a 3 GeV electron incident on the STAR PMD prototype produces clusters of all sizes ranging from one to about 12 hit cells. On the average a cluster of five cells are hit whose signals are to be added to get the value of energy deposited by the showering particle. The centroid of the cluster of cells fired yield the position of the hit in the PMD plane. Earlier simulations studies indicate that the cluster size obtained form the test data very closely resembles that obtained from GEANT simulation thereby suggesting that the occupancy of the detector for a given multiplicity can be obtained reliably with GEANT simulation.

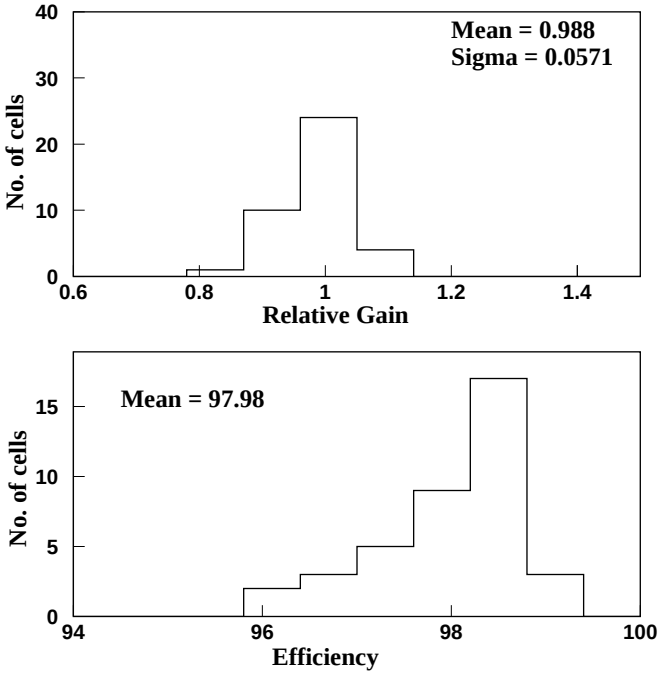

Figure 3.14: Distribution of (top) gain and (bottom) efficiency for randomly selected 40 cells from the prototype chamber.

The energy deposition spectra for electrons at various energies as obtained from the test data and those obtained from the GEANT simulation at corresponding energies are shown in the right panel of Fig. 3.15. Even though the shapes look similar, the relative widths in the preshower spectra are larger in test data compared to those in simulation. This difference is due to the fluctuations in gas ionization, signal generation and transmission processes associated in data, which are not accounted for in simulation. It was therefore necessary to estimate this and introduce the same in simulations regarding a proper modeling of width of energy deposition. This extra width is called the *readout width*.

Left panel of Fig. 3.16 shows the readout width for a range of energy deposition values. For this plot, data using $2X_0$ thick converter has also been used. From the given plot, we can deduce the readout width for any given energy deposition

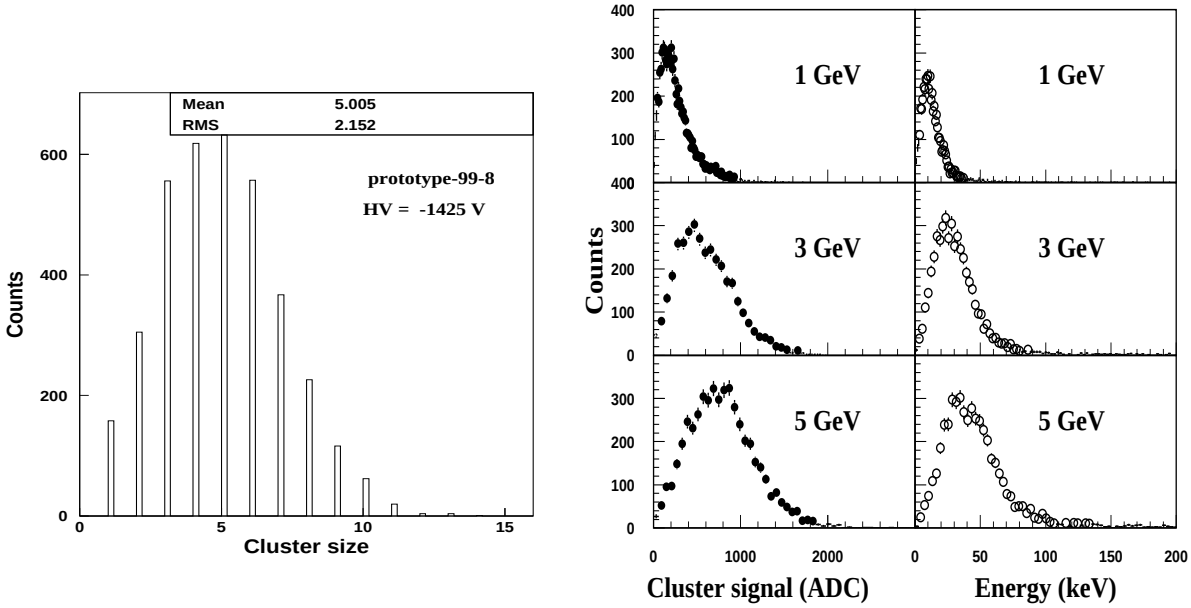

Figure 3.15: (left) Typical cluster size for preshower expressed in terms of the cells affected by electron, (right panel) filled circles represent energy deposition (in terms of cluster ADC) spectra for electrons with three energies, (right panel) open circles represent the simulated energy deposition (in keV) for electrons with corresponding energies. Width of simulated spectra is smaller compared to test data.

obtained from GEANT simulation and fold the values for a detailed comparison with experimental data.

The right panel of Fig. 3.16 shows the mean energy deposition obtained from simulation plotted against the mean ADC values obtained for a particle of given energy. The first point corresponds to a MIP while the last point correspond to 10 GeV electrons. One can see that the response of the prototype is fairly linear The response of the detector and readout is seen to be fairly nearer in the range of energy studied, upto that expected from 10 GeV photons in the preshower part.

3.9 Clustering in PMD and Finding Photon Hits

As we had mentioned earlier, to find the energy deposited by a photon or a hadron one needs to add the signals obtained from the associated cluster of cells. The particle

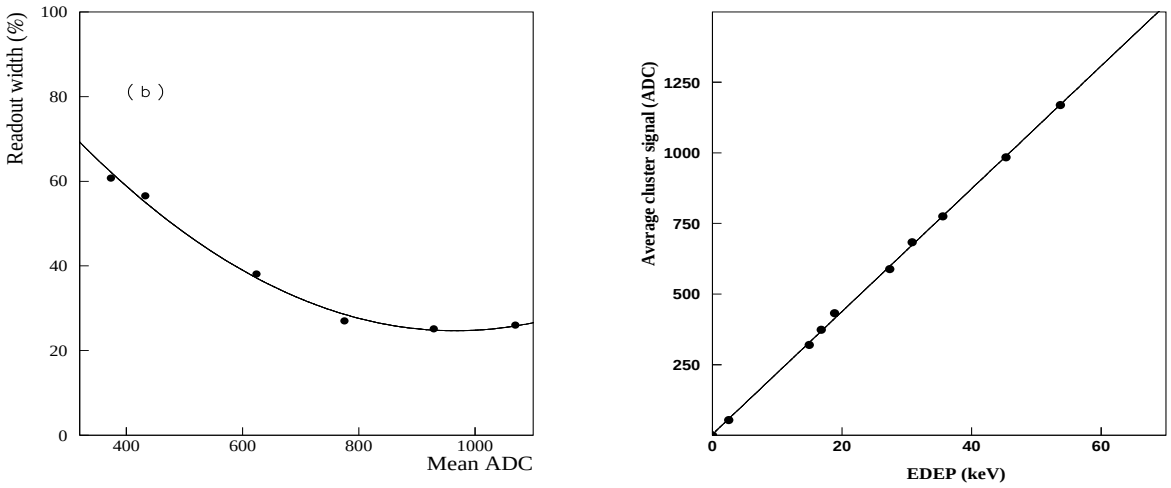

Figure 3.16: (left) Readout width (%) shown for various energy deposition expressed in terms of cluster ADC (right) Calibration plot, showing the relation between the energy deposition obtained from simulation and the cluster ADC obtained from test data.

hit position can be determined from the centroid of the cluster of cells hit. But to determine whether the particle was a photon or a charged hadron one needs to apply some kind of a discrimination on the obtained signal. One of the oldest methods [26, 77, 104] has been to apply a 3 MIP cut on the signal. Anything above this can considered, with certain probability, as that due to a photon. Therefore the first thing to do with the ADC signal is to employ some kind of a clustering and find out the total ADC contained.

When multiplicity is very high then clusters start overlapping and it becomes difficult to employ a simple procedure. In such a case, one can construct superclusters consisting of a large number of cells. The reconstruction procedure involves two steps: (a) breaking of large clusters into smaller clusters each of which represents one incident particle and (b) remove the clusters formed by charged particles from the reconstructed clusters using some energy threshold.

The first step involves arranging the energy deposited in each cell in descending order. The super clusters are then formed beginning at the cell having largest energy

deposition and collecting the all cells contiguous to it. This process is repeated with decreasing order of energy deposition till all the cells are exhausted. This completes the formation of superclusters. Each supercluster is then examined to determine whether it can be broken up into smaller clusters. If the cluster consists of one cell, the center of the cluster is identified with the center of the cell and the strength of the cluster is identified with the energy deposition of the cell. For two cell clusters, the center of the cluster is defined to be the center of gravity of the two cells and the strength is defined to be the sum of the energy deposited in the two cells. If the super cluster has more than two cells, then one has to break the large clusters into smaller clusters. The centers of the clusters are expected to be near the cells corresponding to the peaks in energy deposition. The reason for the above is as follows:

1. A weak peak close to a strong peak may not be considered as a separate cluster. Because we expect that there would be nonzero energy deposition in cells neighboring the peaks. If the peak is strong the neighboring cells will have relatively large energy deposition. Unless another peak close to the strong peak is strong enough, one may consider it to be associated with the strong peak.

2. There will have fluctuations in the actual energy deposition. These fluctuations may produce fictitious peaks, particularly for cells close to the cell having large energy deposition.

In order to accommodate these points, the peaks neighboring a peak having a large energy deposition are not considered as independent cluster centers if the corresponding peak strengths are below a certain fraction of that for the strong peak. The condition adopted at the moment is that the second next nearest neighbor (which is at a distance of $\sqrt{3}$ cell units) must have energy deposition greater than 25% to be considered as a separate centre in addition the third next nearest (which is at a distance of 2 cell units) must have an energy deposition greater than 10% of the main

peak energy deposition value.

Having determined the possible cluster centers, a minimization procedure is used to optimize the position and strength of the cluster. For this, we assume that each cluster has a Gaussian shape. The centers, heights and widths of these Gaussians are then varied for optimization. The output from the above clustering procedure are: X, Y position, η, ϕ, of the clusters, number of cells in each cluster and the energy deposition (ADC) of the clusters. Then one has to separate the charged particle clusters and identify the photon like clusters using different a procedure. One of the procedures is based on the fact that photon clusters are expected to deposit larger amount of energy compared to hadron clusters. So, one can tag the clusters having energy greater than some predetermined threshold energy value as photon clusters and others as non-photon clusters. In the present case, we use 3 MIP signal as the energy cut off for photon like clusters. However, it is possible that some of the hadrons would deposit enough energy to be misidentified as photons. Their fraction and the photon detection efficiency for the PMD is estimated from simulations. This is discussed later.

3.10 Procedure For Generating Simulated Data

From the test beam studies, we have learned details about the detector response to both hadrons and photons. Using the keV-ADC calibration relation (Fig. 3.16, right panel) as obtained from the test beam data, in the preshower mode, the energy deposition in each cell of the detector is converted to their ADC values. This conversion of energy deposition to the corresponding ADC values is necessary to make the simulated data resemble the real data. The various steps used in generating the simulated data, regarding a photon or charge particle hit, from an event generator (or from single particle input) along with a GEANT simulation are shown in the flow chart given in Fig. 3.17. In STAR simulation framework, this flow chart includes both the GEANT simulation for STAR (GSTAR) and the chain used for reconstruction, which

is the Big Full Chain (BFC). In the present study, with Au+Au collisions at $\sqrt{s_{NN}}$= 200 GeV, events from the HIJING event generator have been used.

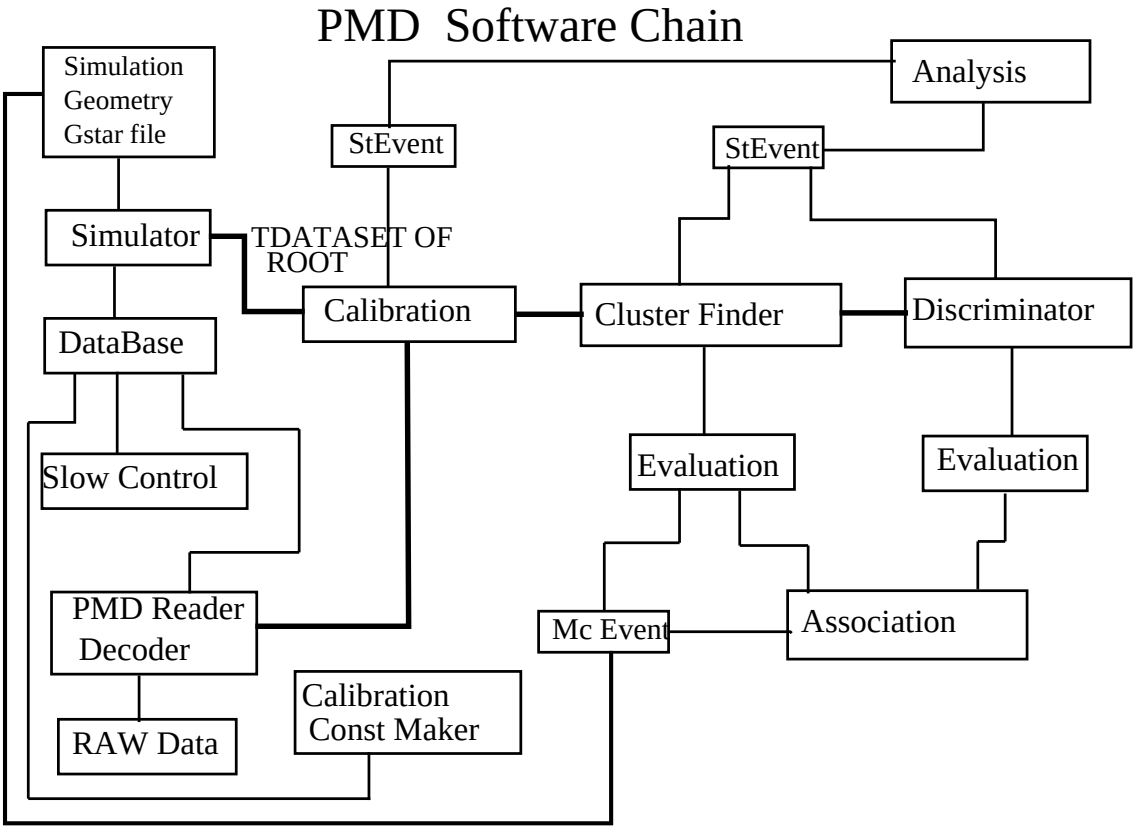

Figure 3.17: Flow chart showing the steps in generating simulated events.

3.10.1 PMD in GSTAR and Big Full Chain (BFC)

GSTAR is a simulation framework designed for the STAR detector using the GEANT simulation package Geant3.21. The GSTAR package consists of a set of **.g modules**, each providing the description of the geometry for different subsystems of the STAR detector, like: beam pipe, TPC, SVT, FTPC, PMD, etc. Also it performs particle generation with on-flight analysis. The PMD geometry has been implemented in the GSTAR framework considering each plane (preshower and veto) of the PMD to be consisting of 17 SMs. In order to simplify the implementation of SMs of different

sizes, there are more number of SMs in GEANT compared to their actual number (12). The layout of PMD in GSTAR framework is shown in Fig. 3.18.

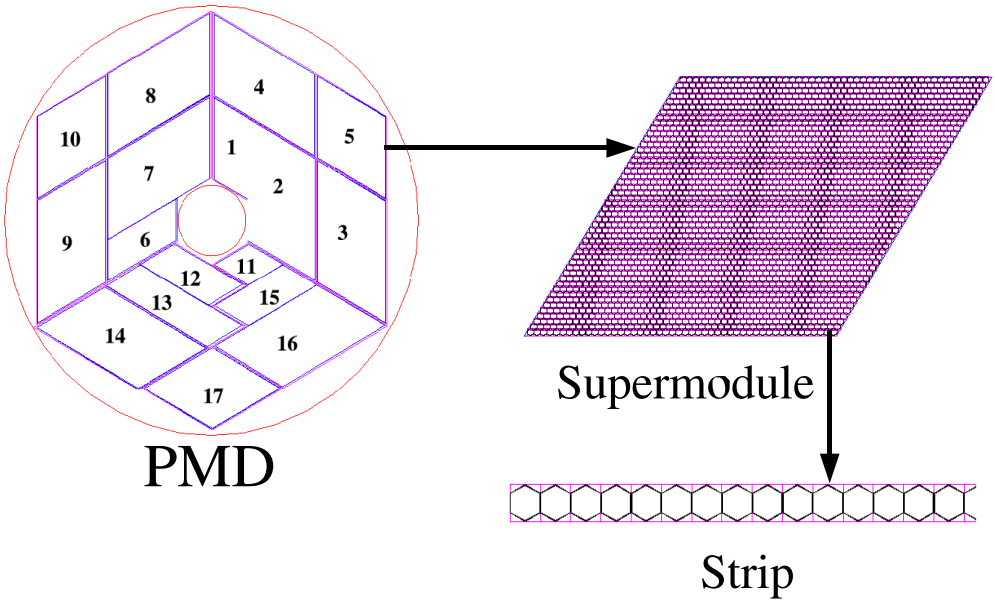

Figure 3.18: Layout of PMD in GSTAR framework.

In GSTAR framework the PMD is implemented in the following manner. First we divide the PMD volume into three sectors. Sector 1 and 2 are decided into 5 volumes with sector 3 divided into 7 volumes which are of same size as the SMs taken into consideration. Each volume has been made with air placed independently inside the sector. Then, we place an Al frame inside each volume which corresponds to the outer frames of the SMs. In the next step, for each SM, a PCB board (G10 material, density 1.7) which corresponds both the FEE plane and the first layer of PCB on

the chamber. The next layer of material corresponds to the active volume made out of gas filled honeycomb array of detectors. The implementation of the honeycomb array is done as follows. The material volume available inside the SM is broken up into rows of strips in air which are then filled with hexagonal cells of Cu with inner and outer radii 0.53 cm and 0.55 cm respectively. The volume is then filled with a mixture of Ar and CO_2 in the ratio Ar:CO_2::70:30. Having formed gas filled array of cells, we now place another layer of PCB material of thickness (density 1.7) to simulate the back plane of the chamber. This is done for all the 17 SMs in the CPV plane. Having constructed the CPV plane, we now include a Pb plane of thickness 1.5 cm on top of which we place an SS plane of thickness 0.5 cm. Next we proceed to construct a preshower plane starting with the Al frame as has been done in the beginning. However, here we include the FEE plane at the end.

Several processes have been implemented for different SMs e.g. applying calibration constants to outputs of each SMs, finding clusters from the hits over the SMs and associating hits/clusters from the SMs to reconstruct particle tracks etc. The STAR reconstruction process includes all the above processes in the proper ordering in the BFC. Each process is designated as a derived class (or Maker) from an abstract base class.

3.10.2 Occupancy and Multihit Probability

The study of occupancy and multiple-hit probability were carried out using the HIJING [75] event generator and GEANT simulation, taking PMD only in air as well as PMD with all the other sub-detectors. The occupancy is defined as the ratio of number of cells fired to the total number of cells. Similarly, the multi-hit probability is defined as the ratio of number of cells fired multiple times to the total number of cells fired. The results for occupancy and the multi-hit probability as a function of pseudorapidity (η) for central and peripheral events with PMD only in air and PMD with all the sub-detectors included are shown in the Fig. 3.19.

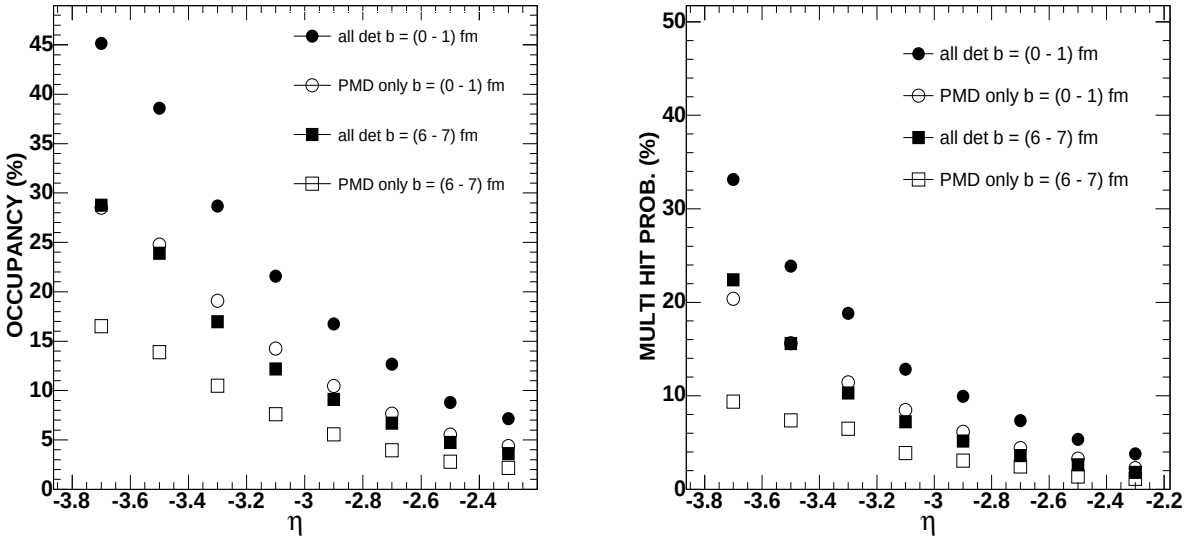

Figure 3.19: (a). Occupancy and (b). multihit probability as a function of pseudorapidity (η) for different impact parameter for all detector and PMD only in air cases.

Comparing both the cases viz PMD only in air and PMD with all other subdetectors, it is clear that, in the later case the occupancy and the multi-hit probability both go up because of the effect of upstream material. Both the occupancy and multihit probability decrease as we go from higher to lower pseudorapidity. Near the beam pipe, corresponding to higher η values, the particle density is high compared to the number of cells. Correspondingly the super modules which are near the beam pipe have large occupancy and multi-hit probability.

3.10.3 Effect of Upstream Material on Photons

The effect of upstream material is described in terms of changes in occupancy, multihit probability, deviation of incoming particles from their incident tracks. The effect of upstream material on photons is the conversion and the scattering because of which they may come to the detector after large deflections. This also affects the photon counting efficiency and purity of the detected photon sample.

The distributions of $\delta\eta$ ($= \eta_{clus} - \eta_{orig}$) and $\delta\phi$ ($= \phi_{clus} - \phi_{orig}$) for the PMD only and for PMD in presence of all the upstream material are shown in Fig. 3.20. Here η_{orig} and ϕ_{orig} represent the original values of the track resulting in a cluster at a position denoted by η_{clus} and ϕ_{clus} on the detector plane. For the case of full STAR simulation, a large number of photons appears on the PMD after getting scattered from the beam pipe and other upstream material. From Fig. 3.20, one can see that there is a bump on the left side of $\eta_{clus} - \eta_{orig}$ plot. Such large deflections worsen the capability of the PMD for the determination of spatial distribution of particles on an event-by-event basis.

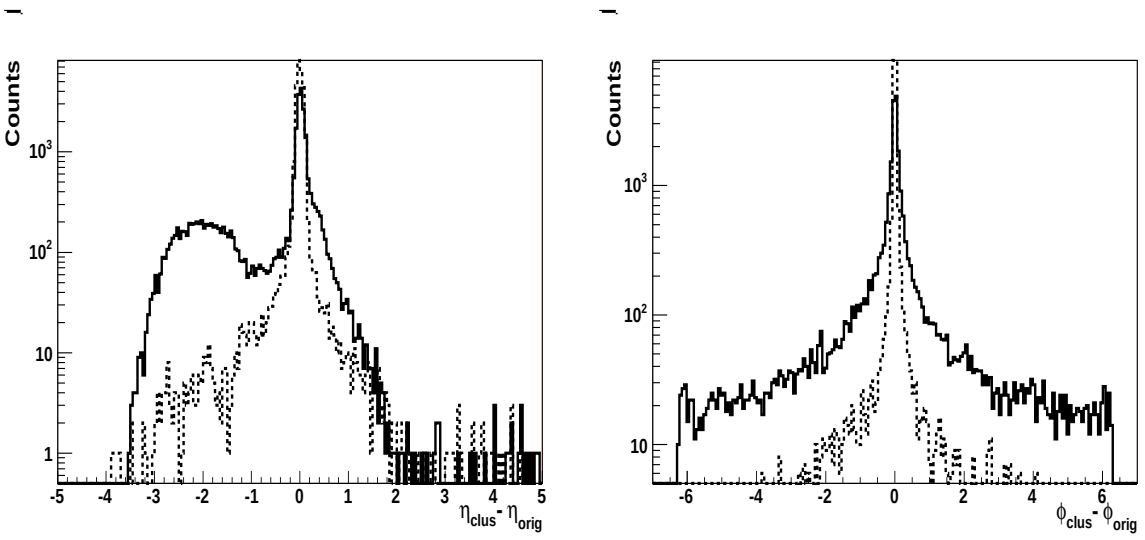

Figure 3.20: $\delta\eta$ and $\delta\phi$ distribution (the difference between the original η, ϕ of the corresponding cluster position) for photons for PMD alone (dotted lines), PMD with upstream material (solid line).

3.10.4 Photon counting

The main task of PMD was the counting of photons. The hadrons behave like MIPs. But high energetic hadrons undergoing interaction in the converter give signals which are similar to those of photons. Therefore, all the hadrons are not rejected by applying a 3 MIP threshold. The clusters, which remains above the hadron rejection threshold

are termed as γ-like clusters. Majority of these clusters correspond to photons with some fraction of hadrons as contaminants. This reduces the purity of the photon sample. Clusters on the preshower plane are labeled as contaminants if:

- they originate from an incident particle other than photon;
- there is more than one cluster for a photon track because of upstream material or splitting of cluster at the boundary of an SM. In such a case, the cluster with higher signal is treated as photon cluster, the other one being treated as contaminant.
- the clusters having $\delta\eta > 0.1$ or $\delta\phi > 20^0$ (which can occur because of large angle scattering of an incident track), will be taken as a contaminant.

A suitable correction is applied on the γ-like clusters to get the N_γ. The photon counting efficiency ϵ_γ and the fractional purity f_p of the photon sample are defined by the following relations:

$$\epsilon_\gamma = N_{cls}^{\gamma,th}/N_{inc}^{\gamma} \tag{3.1}$$

$$f_p = N_{cls}^{\gamma,th}/N_{\gamma-like} \tag{3.2}$$

where, N_{inc}^{γ} is the number of incident photons, which we calculate from the HIJING event generator, $N_{cls}^{\gamma,th}$ is number of photon clusters above the hadron rejection threshold and $N_{\gamma-like}$ is the total number of clusters above the hadron rejection threshold. Using the estimated values of ϵ_γ and f_p as defined above, one can estimate the number of incident photons (N_γ) as:

$$N_\gamma^{est} = N_{\gamma-like} \times f_p/\epsilon_\gamma \tag{3.3}$$

$N_{\gamma-like}$ is obtained from the data by applying an optimal value of the threshold energy cut on the clusters. The threshold value is determined in terms of MIP energy units. The efficiency (ϵ_γ) and purity (f_p) are determined from the simulation. The photon counting efficiency and purity depend on the several factors, like: the conversion probability, criteria applied for hadron rejection threshold, granularity and the track reconstruction efficiency. Because of the change in particle multiplicity and the energy, these factors also depend on the centrality and pseudorapidity. Results on some detailed studies regarding photon counting efficiency and purity of the photon sample in STAR are given below.

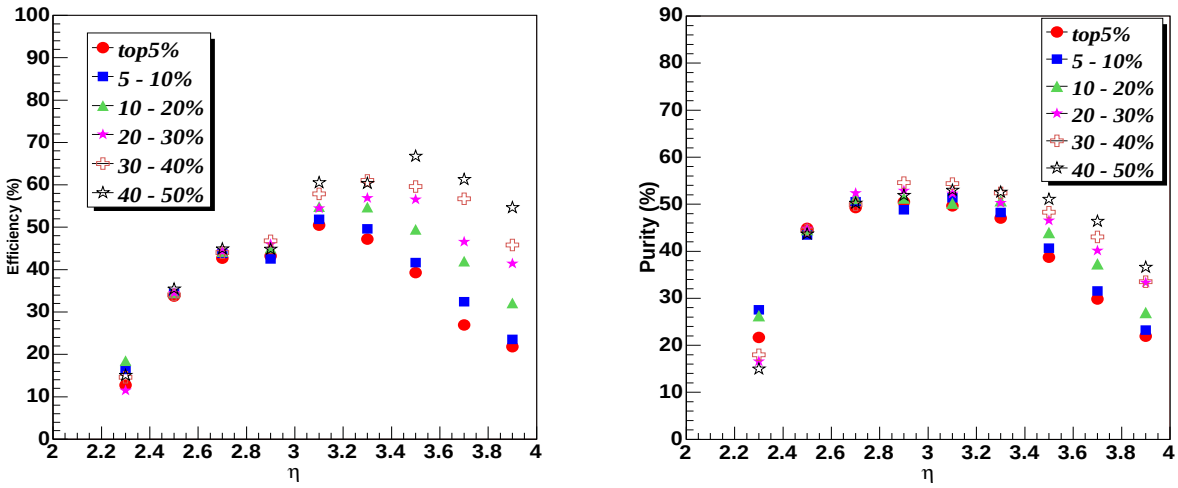

Figure 3.21: η-dependence of photon counting efficiency ϵ_{gamma}, (left) and purity, f_p, (right) for different centralities.

Figure 3.21 shows ϵ_γ and f_p values as functions of η, and centrality, for Au+Au collisions at $\sqrt{s_{NN}}$=200 GeV, obtained from simulation using HIJING with default parameters. The efficiency and purity values are found to be smaller at lower η values, away from the beam pipe. The obtained values of efficiency and purity correspond to a 3 MIP photon-hadron discrimination cut.

Figure 3.22 shows a typical event display in Au+Au collisions at $\sqrt{s_{NN}}$ = 200 GeV. The blank space in the figure indicates the locations where FEE chains were

absent during data taking. The figure shows x-y hit display accumulated over several events.The ADC distributions of all SMs were normalized to produce almost the same spectrum before any cut is applied for photon-hadron discrimination.

Using the above values of efficiency and purity, (Fig. 3.22), we obtain the total number of photons falling on the PMD coverage. The corresponding pseudorapidity distributions of photon for various centrality classes of events in Au+Au collisions at $\sqrt{s_{NN}}$ = 200 GeV, are shown in Fig.3.23. In the forward rapidity region, for 2.3 $< \eta <$ 3.8, the results seem to closely follow the PHOBOS data on charged particles [108]. This is not surprising since the charged particle multiplicity is almost twice that of neutral pions which eventually decay producing two photons. These data are still preliminary and a lot of checks regarding errors (both statistical and systematic) are in progress. These data on Au+Au collisions were taken in RUN4 in 2003-2004. The minimum bias events correspond to only 40k events with production high trigger.

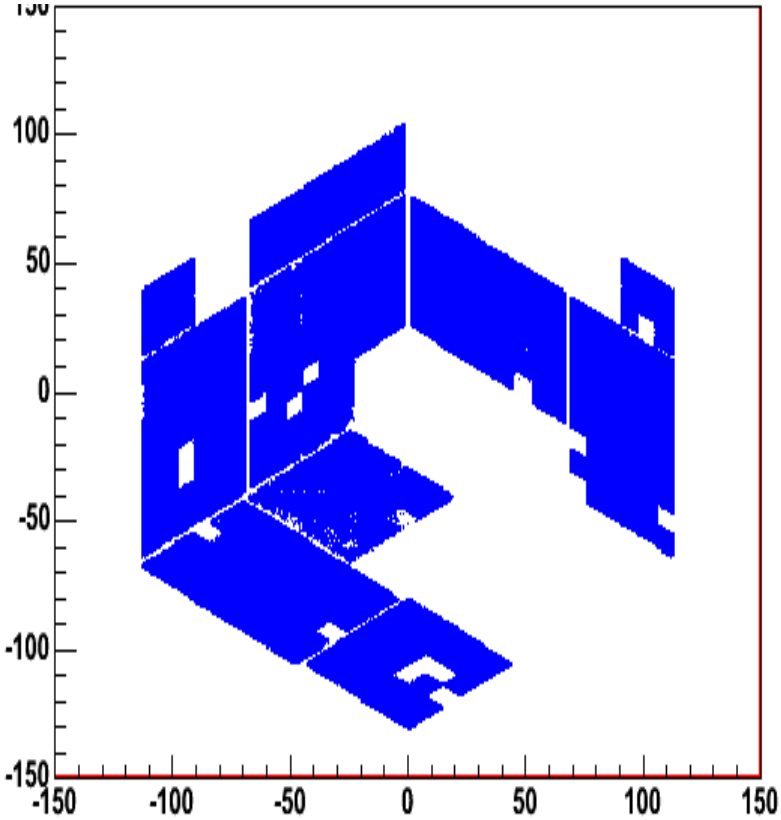

Figure 3.22: Typical event display in preshower plane of PMD in Au+Au collisions at $\sqrt{s_{NN}} = 200$ GeV.

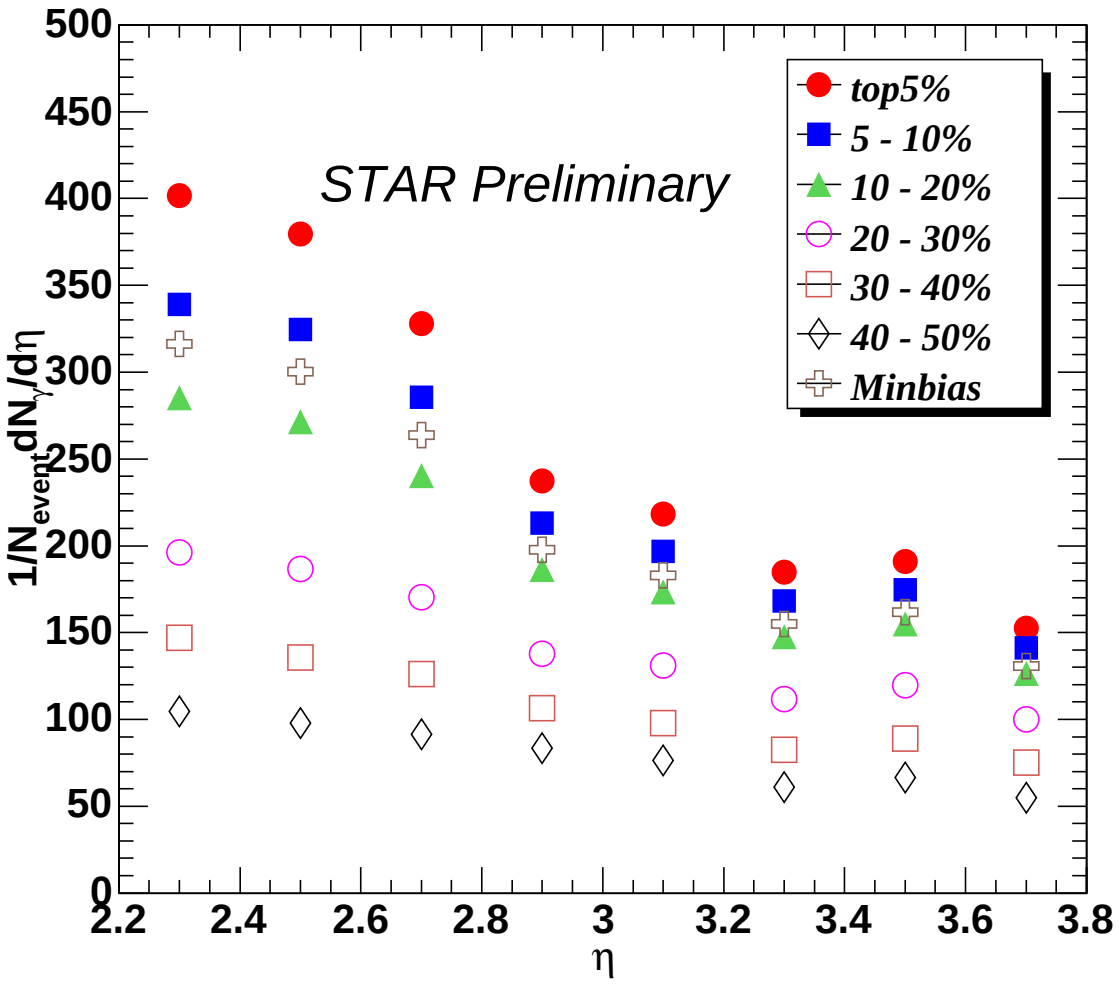

Figure 3.23: Pseudorapidity distribution of photons in Au+Au collisions at $\sqrt{s_{NN}} =$ 200 GeV, for different centralities.

Chapter 4

The $\Delta(1232)$ and $K^*(892)$ Resonance Production in d+Au Collisions

4.1 Introduction

As has been mentioned earlier, resonances have unique characteristics to probe various properties of the hot and dense matter produced in relativistic heavy-ion collisions. The in-medium effects related to the high density and/or high temperature of the medium can modify various resonance properties, such as masses, widths and yields. Since resonances may decay between chemical and thermal freeze-outs of the fire ball, they can also provide information on hadronization and the time span between chemical and thermal freeze-out. Comparison of the properties of these resonances obtained from heavy ion collisions with the same obtained from elementary p+p and $e^+ + e^-$ collisions is expected to provide evidences for possible in-medium effects. In view of this, STAR has attempted to detect and analyze a number of resonances such as $\rho(771)$, $K^*(892)$, $\phi(1020)$, $\Delta(1232)$, $\Sigma^*(1385)$ and $\Lambda(1520)$. The properties of these resonances in terms of decay channels, branching ratios, widths and life times

Resonance	Decay Channel	Branching Ratio (%)	Width (MeV/c^2)	Life time (fm)
$\rho^0(770)$	$\pi^+\pi^-$	~100	150	1.3
$\Delta(1232)$	$p\pi$	>99	~120	~1.6
$f_0(980)$	$\pi^+\pi^-$	~67	40 to 100	2.6
$K^*(892)$	$K\pi$	~100	50.7	4
$\Sigma^*(1385)$	$\Lambda\pi$	88.2	35.8	5.5
$\Lambda(1520)$	pK	45	15.5	12.6
$\Xi^*(1530)$	$\Xi\pi$	~100	9.1	22
$\phi(1020)$	K^+K^-	49.2	4.46	44

Table 4.1: The measured resonances with their decay channels, branching ratios, widths and lifetimes.

are given in Table 4.1. However, in the present thesis we will be presenting the STAR data only on $\Delta(1232)$ and $K^*(892)$ resonances obtained in d+Au collisions at $\sqrt{s_{NN}}$= 200 GeV. Data in terms of multiplicity density (dN/dy) and p_T distribution of the resonances, yielding information on the freeze-out temperature will be presented and discussed. In the present study, wherever we write Δ and K^*, we would mean $\Delta(1232)$ and $K^{*0}(896)$ respectively. But for $K^{*\pm}$ would be $K^{*\pm}(892)$.

4.2 Analysis Methods

4.2.1 Trigger

The majority of the STAR data are provided by relatively slow detectors: TPC, SVT, FTPC etc. The trigger system looks at every event to decide whether or not to accept that event and initiate recording the data. The detectors which have been used for trigger are: CTB, ZDC, BBC, BEMC, EEMC and FPD. The data set used for the present analysis was taken in the 2002 - 2003 RHIC run for d+Au collisions at $\sqrt{s_{NN}}$=200 GeV. The main tracking device was the TPC [84], which provides information on particle momenta together with energy loss, which are sufficient regarding identification of charged particles traversing through the TPC.

Centrality Bin	Uncorr. FTPCRefMult Range	Uncorr. N_{charge}	N_{bin}
(0-20)%	FTPCRefMult $\geq$ 17	17.58	15.0 $\pm$ 1.1
(20-40)%	10 $\leq$ FTPCRefMult $<$ 17	12.55	10.2 $\pm$ 1.0
(40-100)%	0 $\leq$ FTPCRefMult $<$ 10	6.17	4.0 $\pm$ 0.3

Table 4.2: Centrality definitions for different uncorrected FTPC east reference multiplicity ranges. Uncorrected N_{charge} stands for the average value of uncorrected reference multiplicity in certain centrality bin. In the last column N_{bin} represents the number of binary collisions calculated from Glauber model.

For d+Au collisions, the minimum bias trigger was defined by requiring at least one beam-rapidity neutron in the ZDC along the Au beam direction, which is assigned negative pseudorapidity (η) [109]. This trigger accepted (95 $\pm$ 3)% of the d+Au hadronic cross-section σ_{hadr}^{dAu}. Trigger backgrounds were measured using beam bunches which were not in collisions.

4.2.2 Centrality Selection

Centrality of the d+Au collisions was determined by the uncorrected charged particle multiplicity within a pseudorapidity window of -3.8 $< \eta <$ -2.8, as measured by the Forward Time Projection Chamber (FTPC) along the Au beam direction. The d+Au events were divided into three collision centrality classes: (0-20)%, (20-40)%, (40-100)% of the total hadronic cross section. Table 4.2 lists the uncorrected reference multiplicity ranges for centrality definitions.

The events with z-vertices within $\pm$ 50 cm and $\pm$ 75 cm from the center of TPC were accepted for the present Δ and K^* analysis respectively. The analysis involves a reconstruction of the resonances from their daughter particle tracks identified in the TPC.

4.2.3 Track Selection

In the present analysis, we look at the hadronic decay channels of $\Delta^{++} \rightarrow p\pi^+$ and $\overline{\Delta}^{--} \rightarrow \overline{p}\pi^-$, $K^{*0} \rightarrow K^+\pi^-$, $\overline{K}^{*0} \rightarrow K^-\pi^+$ and $K^{*\pm} \rightarrow K_S^0\pi^\pm$. For Δ, we select the

protons and pions from primary tracks whose distances of closest approach (DCA) were less than 3.0 cm from the vertex. Through the ionization energy loss (dE/dx) in the TPC, charged pions and kaons are identified with momenta upto 0.75 GeV/c, while protons are identified with momenta up to 1.1 GeV/c. The protons and pions were selected by requiring their dE/dx to be within two standard deviations (2σ) of the value ($|N_{\sigma p}|$, $|N_{\sigma \pi}| < 2$) as obtained from Bethe-Bloch fitting (Fig. 2.6). To assure quality track fitting, the proton tracks were selected in such a way that there were at least 22 fit points, the same for pions being 15. Also, in order to avoid unwanted split tracks, the ratio of the number of fit points to the maximum possible fit points was required to be greater than 0.5 for all the selected tracks. With this, tracks with both p and p_T lying between 0.3 - 1.1 GeV/c were cleanly identified as those for protons. Clean pion tracks were picked up with p and p_T lying between 0.1 - 0.6 GeV/c.

In the case of K^{*0} reconstruction, we have selected charged kaons and charged pions from the primary tracks whose DCA values were less than 1.5 cm. however, in the case of $K^{*\pm}$ it is not so simple. First a charged K^* would undergo a strong decay which produces a K^0_S and a charged pion which we call the daughter pion of the charged K^*. Second, the newly produced K^0_S would again undergo a weak decay via $K^0_S \rightarrow \pi^+\pi^-$. The last two pions we call as grand-daughters of the charged K^*. We select the charged daughter pions from primary tracks and select K^0_S candidates through their decay vertex geometries since STAR has great ability in measuring the V0 shaped decay modes through the decay topology method.

The charged kaon tracks were selected requiring dE/dx to be within two standard deviations ($|N_{\sigma K}| < 2$) from the Bethe-Bloch fitting, while for charged pions a less strict dE/dx cut of 3σ ($|N_{\sigma \pi}| < 3$) was selected. Both the kaons and pions were required to have at least 15 fit points and the ratio of the number of fit points to the number of maximum possible fit points was required to be greater than 0.55. Further, kaon tracks were selected with both p and p_T lying between 0.2 - 0.7 GeV/c while for pion tracks the corresponding momentum window was between 0.2 - 10 GeV/c. In the K^* case we have selected the pion tracks with momenta up to 10 GeV/c in order

Centrality	Number of events for Δ	Number of events for K^*
Min. bias	$\sim$ 11.6 M	$\sim$ 15 M
0-20%	$\sim$ 2.2 M	$\sim$ 2.6 M
20-40%	$\sim$ 2.6 M	$\sim$ 3.3 M
40-100%	$\sim$ 6.4 M	$\sim$ 9 M

Table 4.3: Number of events from different centralities used for the present Δ and K^* analysis.

to keep the largest possible statistics for K^* analysis.

In order to reconstruct the K^0_S signals the grand-daughter charged pion tracks were selected from global tracks with their DCAs to the primary vertex greater than 0.5 cm. The grand-daughter charged pions were also required to have at least 15 hit points in the TPC with momenta greater than 0.2 GeV/c. Oppositely charged pion tracks, if their DCA to each other was less than 1.0 cm, were then paired to form neutral decay vertices which are required to be at least 2.0 cm away from the primary vertex. Further, the reconstructed K^0_S momentum vector was required to point back to the primary vertex to within 1.0 cm. The charged K^* signals were then reconstructed by pairing the K^0_S candidates with the daughter pions. Different track IDs were assigned to each of the tracks to identify them as either daughter or grand-daughter pion tracks.

For both the Δ and K^* analysis a pseudo-rapidity cut $|\eta| < 0.8$ and the rapidity cut $|y| < 1$ were applied to all the daughter tracks. Using all the above cuts for event selection, the total number of events used for analysis from d+Au collisions at $\sqrt{s_{NN}}$ = 200 GeV are listed in the Table 4.3.

4.2.4 Constructing the $\Delta(1232)$ and $K^*(892)$ Signal

The STAR TPC can record upto several thousand charged tracks per event originating from the primary collision vertex. But it is difficult to distinguish the daughter particles of $\Delta(1232)$ and $K^*(892)$ from the other primary tracks. We use the following method to reconstruct the Δ and K^* signals. The Δ signals were reconstructed by

calculating the $p\pi$ pair invariant mass spectrum and K^{*0} signals were reconstructed by pairing each oppositely charged kaon and pion. Figure 4.1 (a) shows the $p\pi$ invariant mass and Fig 4.1 (b) shows the $K\pi$ invariant mass distribution from the same-event pairs (invariant mass spectrum determined from tracks in the same event) in the minimum bias d+Au collisions. The invariant mass distributions for Δ and K^* derived in this manner, as shown in Fig. 4.1, are mostly from random combinatorial $p\pi$ and $K\pi$ pairs respectively, which have no correlation at all. The real Δ and K^{*0} signals, within their mass ranges, only constitute about 1.5 % and 0.1% respectively, of the total area under the curves. Therefore, to get the real Δ and K^{*0} invariant spectra one needs to subtract out the huge combinatorial background present in the spectra shown in Fig. 4.1. This is done using an event-mixing analysis which has been successfully used in resonance production analysis at RHIC [66]. In this technique, the invariant mass distribution corresponding to the combinatorial background for the Δ resonance was calculated using uncorrelated proton and pion tracks from different events. The same for K^{*0} was calculated taking uncorrelated oppositely charged kaons and pions from different events.

In the mixed-event data set, the pair partners momenta are completely uncorrelated. However, the combinatorial background was determined taking two partners from different events but belonging to the same centrality class. For this, we have divided the whole data set into 10 uniform multiplicity bins. Also to make sure that there is no contribution from effects due to any vertex shift, the events for every centrality class were sub-divided into 10 further bins depending upon their vertex shift along Z-direction. Finally the mixed-event background was calculated selecting pairs from different events within the same multiplicity bin and same vertex shift bin along Z-direction. The corresponding combinatorial backgrounds obtained for both Δ and K^{*0} states are also included in Fig. 4.1 for comparison.

In the same-event spectrum, as shown in Fig. 4.1, the Δ^{++} and $\overline{\Delta}^{--}$ invariant mass has been reconstructed by taking $\mathrm{p}\pi^+$ and $\overline{p}\pi^-$ respectively. In the mixed-event spectrum, we have sampled $p_1\pi_2^+$ and $p_2\pi_1^+$ pairs for Δ^{++} and $\overline{p_1}\pi_2^-$ and $\overline{p_2}\pi_1^-$ pairs for

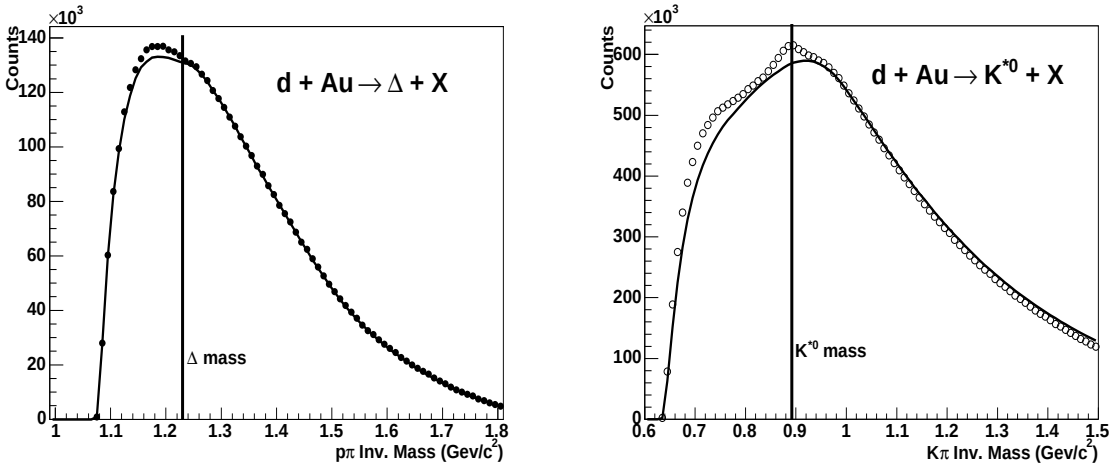

Figure 4.1: (a) $p\pi$ invariant mass distribution. (b) $K\pi$ invariant mass distribution. The symbols represent the same-event pair and the solid curve represent mixed-event pair.

$\overline{\Delta}^{--}$. In the above, the subscript 1 stands for one partner from event 1, 2 standing for the other partner from event 2. Similarly, for K^{*0}, we have sampled $K^+\pi^-$ and $K^-\pi^+$ pairs all coming from the same event. To get the mixed-event spectrum for this we have taken all combinations $K_1^+\pi_2^-$, $K_1^-\pi_2^+$, $K_2^+\pi_1^-$ and $K_2^-\pi_1^+$ satisfying the criteria of event class with respect to multiplicity and vertex shift as mentioned earlier. In order to reduce the statistical errors in the mixed-event spectrum, one can choose the second pair partner from many other events. In our case, we have taken five other events to mix. In this case, the total number of entries in the mixed-event spectrum would be about ten times as much as the total number of entries in the same-event spectrum. So, before the background subtraction from the same-event spectrum, we have to normalize the mixed-event spectrum. In the same-event spectrum the pπ pairs for Δ and the $K\pi$ pairs for K^* with their invariant masses greater than 1.4 GeV/c^2 and 1.1 GeV/c^2 respectively, are very unlikely to be correlated.

In view of the above, the normalization factor has been calculated by taking the ratio of the number of entries in the same-event spectrum to the number of entries in the mixed-event spectrum with invariant mass greater than 1.4 GeV/c^2 for Δ and

1.1 GeV/c^2 for K^*. The background subtraction and normalization of the same-event spectrum to get the true resonant signals is carried out using the following equations as given below.

$$N_{\Delta^{++}}(m) = N_{p_1\pi_1^+}(m) - R \times \sum_{i=2}^{6}[N_{p_1\pi_i^+}(m) + N_{p_i\pi_1^+}] \tag{4.1}$$

$$N_{K^{*0}}(m) = N_{K_1^+\pi_1^-}(m) + N_{K_1^-\pi_1^+}(m) - R \times \sum_{i=2}^{6}[N_{K_1^+\pi_i^-}(m) + N_{K_1^-\pi_i^+}(m) + N_{K_i^+\pi_1^-}(m) + N_{K_i^-\pi_1^+}(m)] \tag{4.2}$$

where, N stands for the number of $p\pi$ or $K\pi$ pairs in a bin, having bin center at m, R representing the normalization factor. Figure 4.2 shows the background subtracted and properly normalized pπ and $K\pi$ pair invariant mass spectra obtained for d+Au collisions at $\sqrt{s_{NN}}$ = 200 GeV.

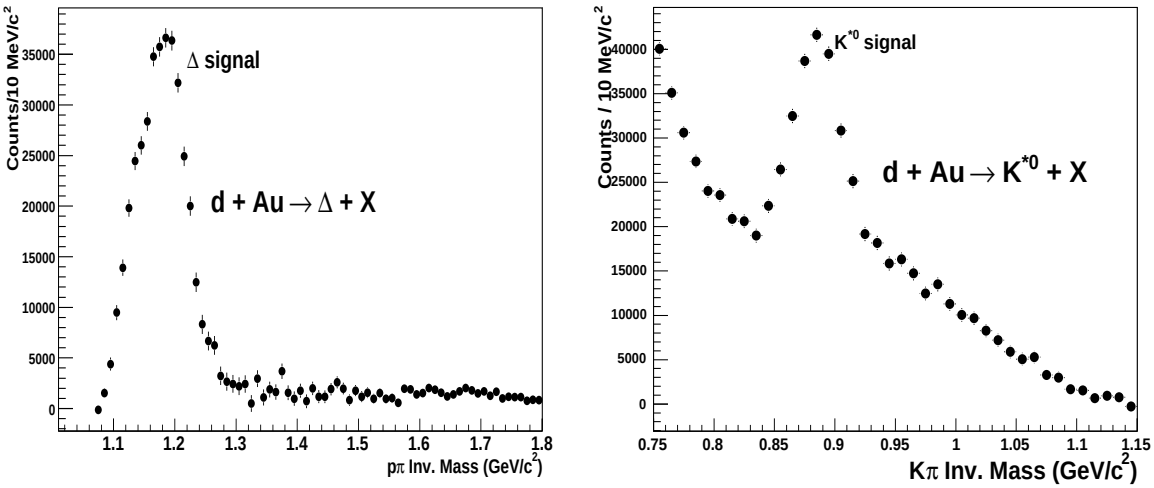

Figure 4.2: (a)The $p\pi$ pair invariant mass spectrum. (b) The $K\pi$ pair invariant mass spectrum after mixed-event background subtraction.

4.3 Residual Background

The event-mixing technique is very much effective in reconstructing the resonance signals in heavy-ion collision data. Nevertheless, the mixed-event combinatorial background cannot perfectly reproduce the background as the "same-event" spectrum. Even after subtraction of the background using mixed-event, there is always certain amount of residual background remaining under the resonance signal [77]. In Fig. 4.2 one can see certain amount of residual background, which could not be subtracted using the mixed-event analysis. The sources of this residual background are: (1) elliptic flow effect; (2) correlated real $p\pi$ and $K\pi$ pairs from decay of other particles; (3) otherwise correlated but misidentified pairs. Some discussions on the residual background are given in the following sections.

4.3.1 Elliptic Flow Effect

In non-central d+Au collisions, the azimuthal distributions of particles are different for different events. In fact, each event shows an elliptic azimuthal distribution in the event plane (as defined by the beam axis and the impact parameter). This anisotropic particle distribution, which we commonly identify as "elliptic flow" originates from various underlying physics issues, one of which is related to the "Equation-of-state". The presence of flow in every event (particularly in non-central ones), indicates that there is an inherent particle-particle correlation that cannot be ignored. In event-mixing, this correlation between particles, present due to elliptic flow, cannot be accounted for. Therefore, a subtraction of a combinatorial background obtained taking pair partners from different events cannot take care of "flow type" two particle correlations in the invariant mass spectrum of any of the considered resonances.

4.3.2 Correlated Real Pairs

Using the mixed-event technique, the subset of all the correlated $p\pi$ and $K\pi$ pairs in the same-event spectrum can not be subtracted taking the mixed-event spectrum. Apart from the $p\pi$ and $K\pi$ pairs from Δ and K^{*0} decays under consideration, there are correlated $p\pi$ and $K\pi$ pairs from other particles, which have the same decay modes. For instance resonances like $N(1440)$, $N(1520)$, $N(1535)$, $N(1650)$, $N(1675)$, $\Delta(1600)$, $\Delta(1620)$, $\Delta(1700)$ decay producing $p\pi$ pairs. Such decays will all have contributions in the invariant mass spectrum for $\Delta(1232)$ under consideration. Similarly as in the case of $K^*(892)$, there are other resonances like $K^*(1410)$, $K_0^*(1430)$, $K_2^*(1430)$, $K^*(1680)$, $D^0(1864)$ etc. which also decay into an oppositely charged $K\pi$ pairs. In addition, some of the kaon resonances such as $K_1(1400) \rightarrow K\rho \rightarrow K\pi\pi$, $K^*(1410) \rightarrow K\rho \rightarrow K\pi\pi$ and $K_2(1770) \rightarrow K\pi\pi$ which decay into more than two daughter particles and two of the final decay daughters can be counted as an oppositely charged $K\pi$ pair. They will also have contributions in the invariant mass spectrum constructed for $K^{*0}(892)$. But correlations coming from the above sources are completely killed in the mixed-event spectrum and their contributions are always present in the invariant mass spectrum shown in Fig. 4.2.

4.3.3 Mis-identified Pairs

The energy loss (dE/dx) curves for the STAR TPC corresponding to various detected particles has been shown in Fig. 2.6. As can be seen from the figure, pions and kaons can be easily identified with momenta less than 0.7 GeV/c while protons can be identified with momenta upto 1.1 GeV/c. However, in the present analysis for K^*, we have selected kaons and pions with their momenta lying between 0.2 GeV/c and 10 GeV/c. So, a pion (kaon) track with momentum greater than 0.7 GeV/c can be mis-identified as a kaon (pion) track. Similarly, a proton track with momentum greater than 1.1 GeV/c can be mis-identified as either a kaon or a pion track. In those cases, other particles can be falsely reconstructed as Δ or K^{*0}. The invariant mass

calculated from their mis-identified decay daughters will be different from their own masses and might be similar to the Δ and K^{*0} masses under consideration. These unwanted contributions in our mass ranges under consideration can not be subtracted out using the mixed-event technique.

4.4 Invariant Yield, Mass and Width Determination for Δ and K^*

The $\Delta(1232)$ is a baryon resonance having $I = 3/2$ and $J = 3/2$. It is designated as $P_{33}(1232)$, which is a $p-$wave ($l = 1$) pion-nucleon resonance. Similarly, in the case of $K^*(892)$ which is a vector meson having $J = 1$. The $K\pi$ invariant mass distribution should therefore be fit to a p-wave Breit-Wigner function.

4.4.1 Fitting Function used for $\Delta^{++}(1232)$

The yield, mass and width of this resonance is determined by fitting the invariant mass with a relativistic $p-$wave Breit-Wigner function [110] as given by

$$BW(M_{p\pi}) = \frac{Y M_{p\pi} M_{\Delta} \Gamma(M_{p\pi})}{(M_{p\pi}^2 - M_{\Delta}^2)^2 + M_{\Delta}^2 \Gamma(M_{p\pi})^2} \tag{4.3}$$

where Y is a constant parameter proportional to the yield of Δ, $M_{p\pi}$ is the $p\pi$ invariant mass, M_{Δ} is the nominal Δ mass and the $\Gamma(M_{p\pi})$ is the momentum dependent width.

$$\Gamma(M_{p\pi}) = \Gamma_{\Delta} \frac{M_{\Delta}}{M_{p\pi}} \frac{k(M_{p\pi})^3 F(\Lambda_{\pi}, k(M_{p\pi}))^2}{k(M_{\Delta})^3 F(\Lambda_{\pi}, k(M_{\Delta}))^2} \tag{4.4}$$

where, $F(\Lambda_{\pi}, k(M_{\Delta}))$ is the form factor used to fit the π-N scattering phase-shift with $\Lambda\pi = 290$ MeV and Γ_{Δ} is the natural Δ width of 120 MeV.

$$k(M_{p\pi})^2 = \frac{(M_{p\pi}^2 - m_p^2 - m_{\pi}^2)^2 - 4m_p^2 m_{\pi}^2}{4M_{p\pi}^2} \tag{4.5}$$

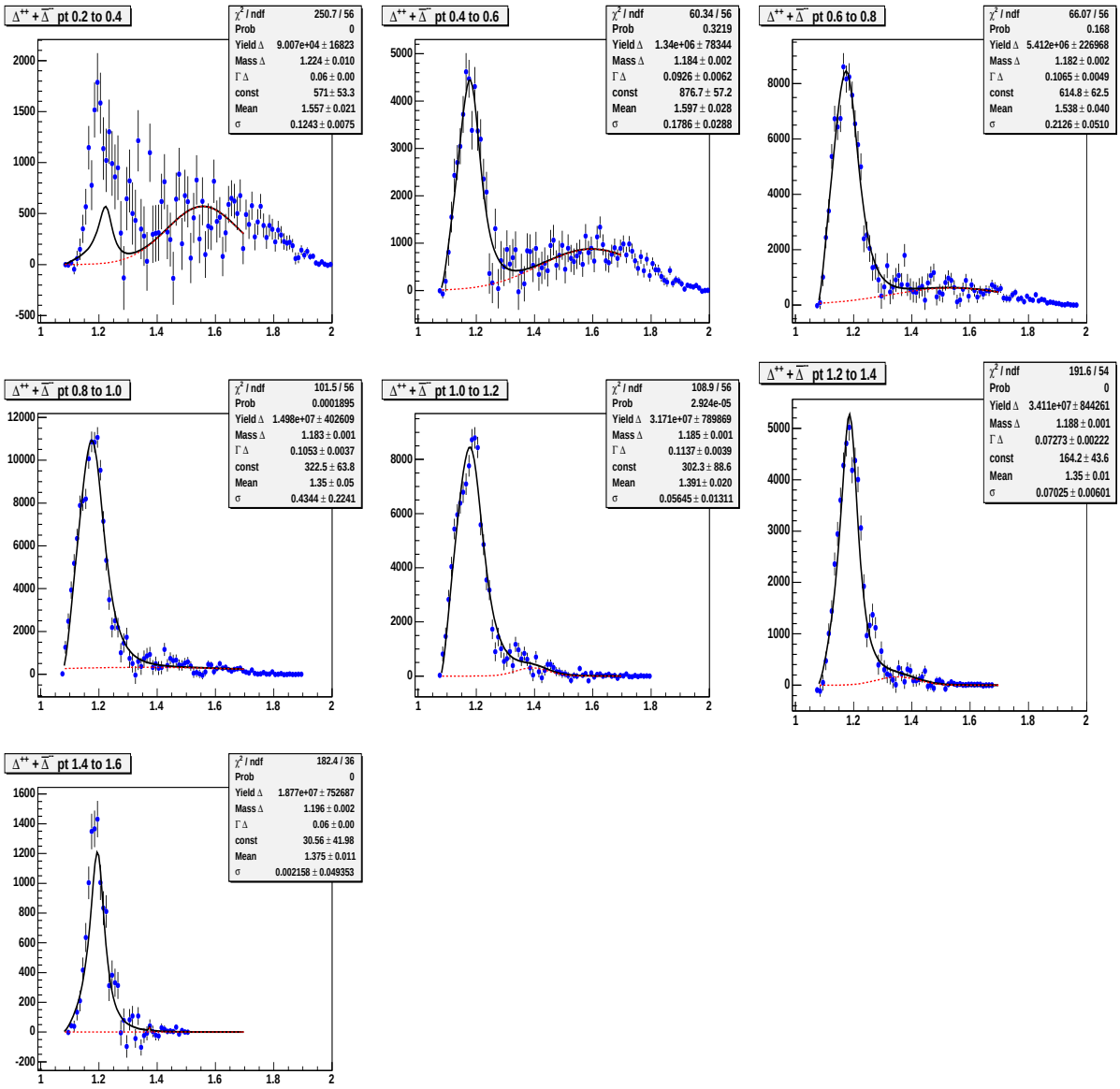

Figure 4.3: The $p\pi$ invariant mass distributions for different p_T bins, each having bin width 0.2 GeV/c for minimum bias trigger. The solid curves stand for the fit function using eqn. 4.12 and the dashed lines stand for the Gaussian residual background.

and

$$k(M_\Delta)^2 = \frac{(M_\Delta^2 - m_p^2 - m_\pi^2)^2 - 4m_p^2 m_\pi^2}{4M_\Delta^2} \tag{4.6}$$

$$F(\Lambda_\pi, k(M_{p\pi})) = \frac{\Lambda_\pi^2}{\Lambda_\pi^2 + k(M_{p\pi})^2} \tag{4.7}$$

and

$$F(\Lambda_\pi, k(M_\Delta)) = \frac{\Lambda_\pi^2}{\Lambda_\pi^2 + k(M_\Delta)^2} \tag{4.8}$$

From eqns 4.5 to 4.8, one can write the momentum dependent width as

$$\Gamma(M) = \Gamma_\Delta[\frac{M_\Delta}{M_{p\pi}}]^2 \left[\frac{(M_{p\pi}^2 - m_p^2 - m_\pi^2)^2 - 4m_p^2 m_\pi^2}{(M_\Delta^2 - m_p^2 - m_\pi^2)^2 - 4m_p^2 m_\pi^2}\right]^{3/2} \times \left[\frac{M_\Delta^2 \Lambda_\pi^2 + (M_\Delta^2 - m_p^2 - m_\pi^2)^2 - 4m_p^2 m_\pi^2}{M_{p\pi}^2 \Lambda_\pi^2 + (M_{p\pi}^2 - m_p^2 - m_\pi^2)^2 - 4m_p^2 m_\pi^2}\right]^2 \tag{4.9}$$

where, m_π is the natural pion mass (139 MeV), m_p is the natural proton mass (938 MeV). As we know, in d+Au collisions, apart from a direct production the Δ particles (resonances), these particles are also produced by re-generation through p and π scatterings in the medium [65], as shown schematically in Fig. 4.4(a). Therefore, the

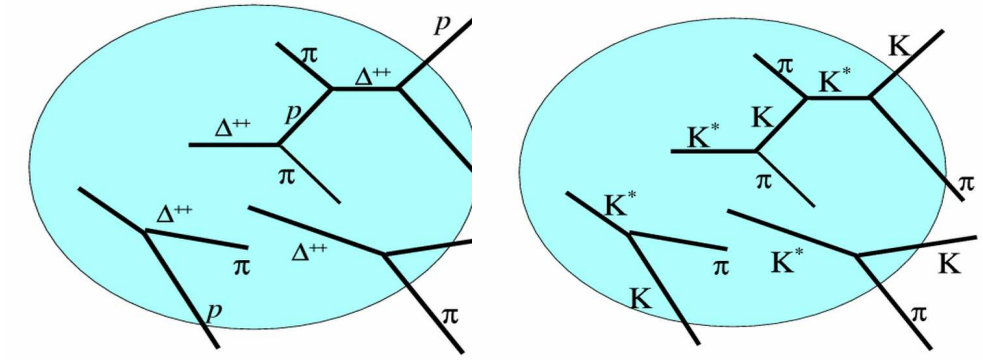

Figure 4.4: Schematic diagram showing the production and re-generation of Δ and K^* by re-scattering and re-generation effects inside the medium (a) Δ and (b) K^*.

$p\pi$ invariant mass distribution is expected to get modified by the initial phase space distribution of p and π. An appropriate correction factor in terms of a multiplication

factor coming from phase-space requirements must therefore be included in the function used to fit the invariant mass distribution [63, 68, 113]. This factor called the phase space (PSF) factor is given by.

$$PSF(M_{p\pi}) = \frac{M_{p\pi}}{\sqrt{M_{p\pi}^2 + p_T^2}} exp\left(\frac{-\sqrt{M_{p\pi}^2 + p_T^2}}{T_{fo}}\right) \tag{4.10}$$

where, p_T is the transverse momentum of Δ and T_{fo} is the expected "freeze-out" temperature at which the resonance is emitted. The value of T_{fo} for Au+Au and p+p collisions at $\sqrt{s_{NN}}$=200 GeV, as obtained from the respective p_T spectra, are found to be 120 and 160 MeV respectively. For the present case with d+Au at the same energy, which is more likely p+p collisions. So, we have taken $T_{fo} = 160$ MeV for our analysis. The residual background as denoted by RBG in the fitting function is defined as given below.

$$RBG(M_{p\pi}) = A \times exp(\frac{M_{p\pi} - B^2}{2C^2}) \tag{4.11}$$

where A is a normalization constant, B and C representing the mean and the sigma of the Gaussian function respectively.

Taking the above correction, for residual background together with the phase-space factor as given by eqn. 4.10 into account, we use the following equation to fit the $p\pi$ invariant mass spectrum.

$$f(M_{p\pi}) = BW(M_{p\pi}) \times PSF(M_{p\pi}) + RBG(M_{p\pi}) \tag{4.12}$$

In the above fitting function, there are six open parameters *viz.* Y, A, B, C, M_Δ and Γ_Δ which need to be determined. Among these, Y, M_Δ and Γ_Δ represent the yield, the mass and the width of the Δ resonance.

4.4.2 Fitting Function Used For K^*(892)

The yield, mass and width of K^* is determined by fitting the $K\pi$ invariant mass distribution with the relativistic p-wave Breit-Wigner function as has been done for $\Delta(1232)$ (eqn. 4.3).

$$BW(M_{K\pi}) = \frac{Y M_{K\pi} M_{K^*} \Gamma(M_{K\pi})}{(M_{K\pi}^2 - M_{K^*}^2)^2 + M_{K^*}^2 \Gamma(M_{K\pi})^2} \tag{4.13}$$

where Y is a constant parameter proportional to the yield, $M_{K\pi}$ is the $K\pi$ invariant mass, M_{K^*} is the natural K^* mass (892 MeV), $\Gamma(M_{K\pi})$ representing the momentum dependent width which can be written as

$$\Gamma(M_{K\pi}) = \left[\frac{M_{K\pi}^2 - (m_\pi + M_K)^2}{M_{K^*}^2 - (m_\pi + M_K)^2}\right]^{3/2} \frac{\Gamma_{K^*} M_{K^*}}{M_{K\pi}} \tag{4.14}$$

where, Γ_{K^*} is the natural $K^*(892)$ width (50.7 MeV), m_π is the natural pion mass (139 MeV), m_K being the natural kaon mass (493 MeV). As in the case of Δ resonance, K^* can also be re-generated through kaon and pion scattering in the hadronic medium. This is shown schematically in Fig. 4.4(b). Because of this, the invariant mass of K^* is expected to be modified by the initial kaon and pion phase space distribution. So, the p-wave Breit-Wigner fitting function (eqn. 4.13) needs to be multiplied by a phase space factor which is given in the following equation.

$$PSF(M_{K\pi}) = \frac{M_{K\pi}}{\sqrt{M_{K\pi}^2 + p_T^2}} \times exp\left(\frac{-\sqrt{M_{K\pi}^2 + p_T^2}}{T_{fo}}\right) \tag{4.15}$$

where, p_T is the transverse momentum of the K^* and T_{fo} (160 MeV) is the expected freeze-out temperature at which the K^* resonance is emitted. In this case also there is a certain amount of residual background even after the subtraction of background obtained from mixed-events. This residual background, denoted by RBG, can be represented by a linear function:

$$RBG(M_{K\pi}) = BM_{K\pi} + C \tag{4.16}$$

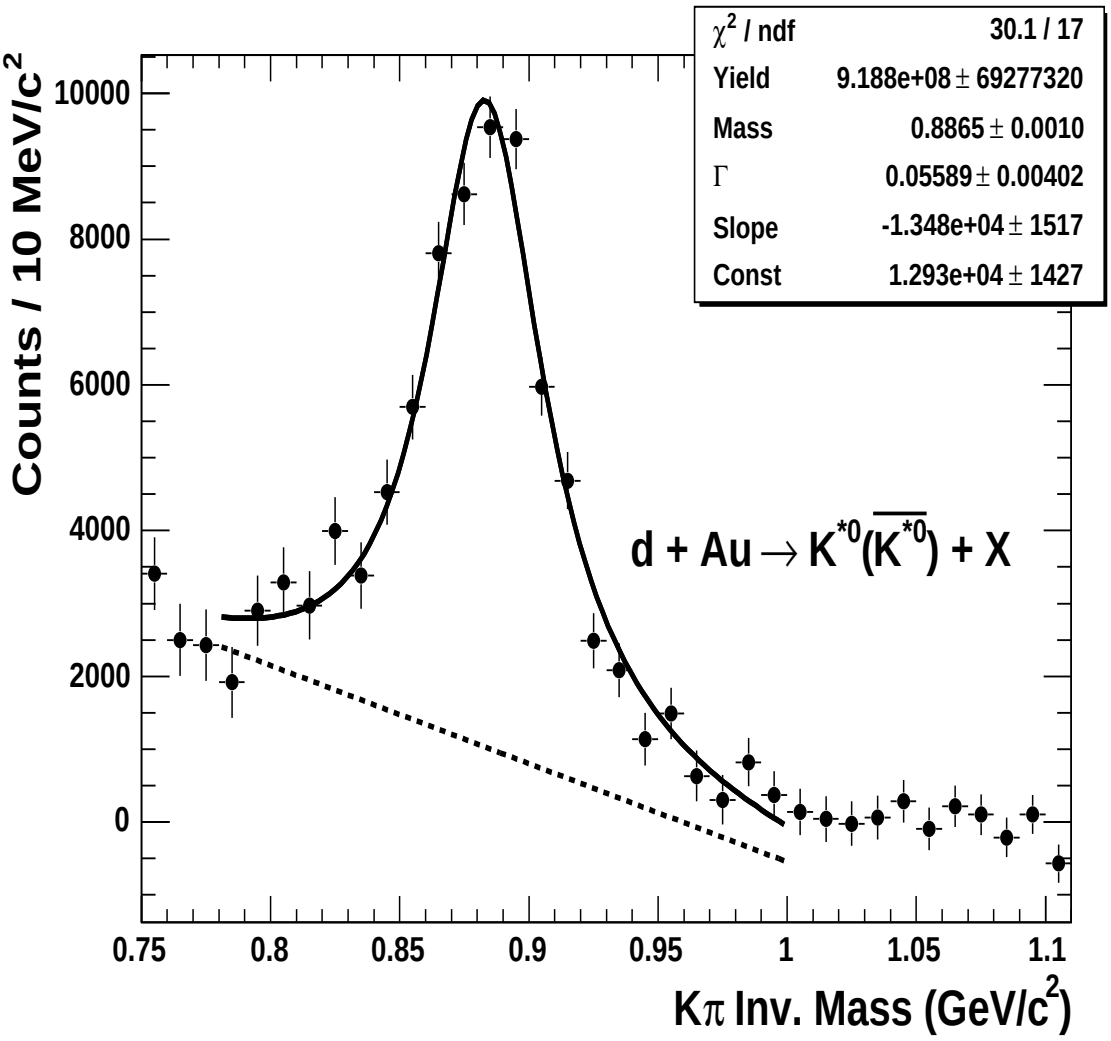

Figure 4.5: The $K\pi$ invariant mass distribution fitted to eqn. 4.17 to extract the $K^{*0}(892)$ yield in $d+Au$ collisions at $\sqrt{s_{NN}}$=200 GeV. The solid curve represents the Breit-Wigner fit to the data points with a linear background as given by the dashed line (eqn. 4.17).

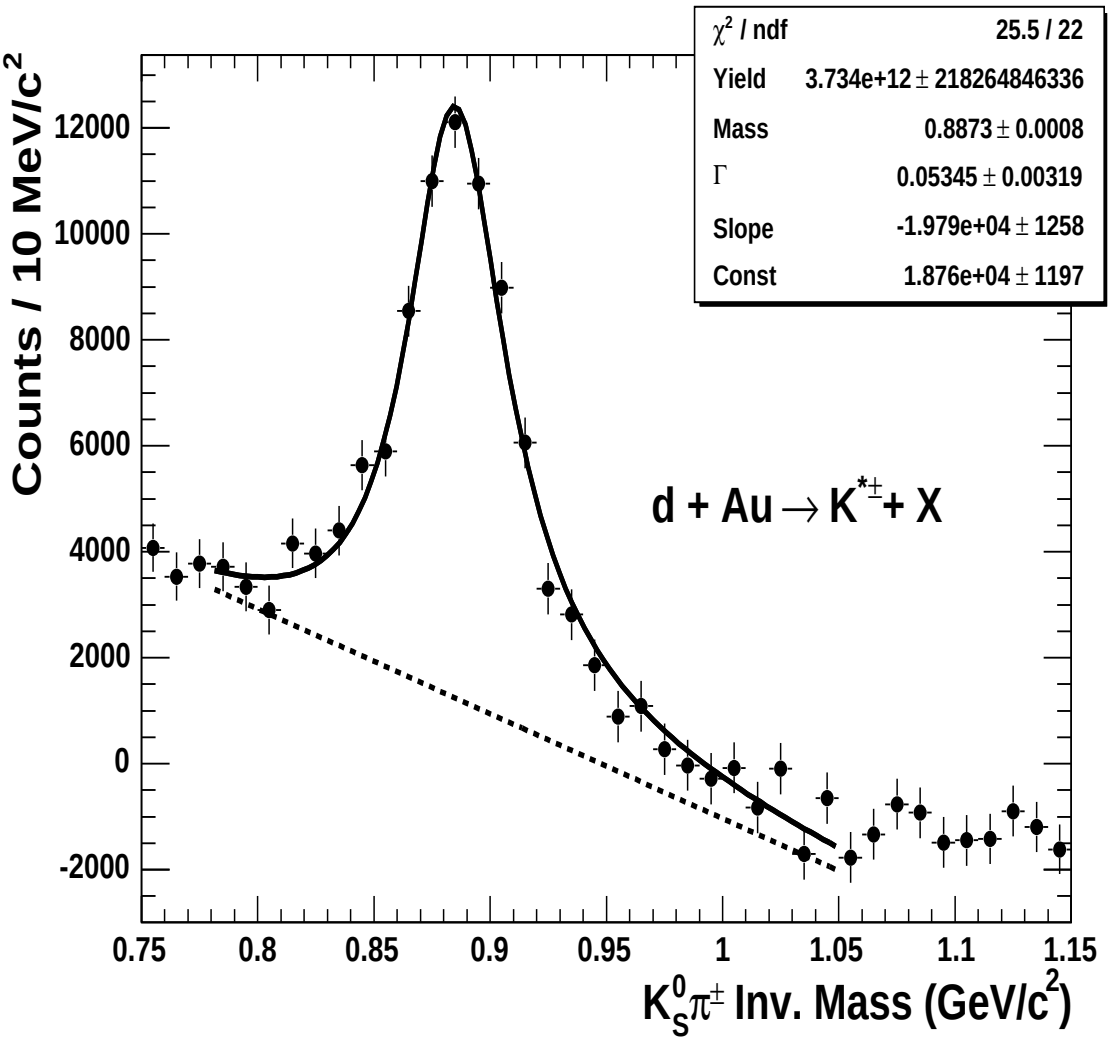

Figure 4.6: The $K^0_S\pi^{\pm}$ invariant mass distribution fitted to eqn. 4.17 to extract the $K^{*\pm}(892)$ yield in $d+Au$ collisions at $\sqrt{s_{NN}}$=200 GeV. The solid curve represents the Breit-Wigner fit to the data points with a linear background as given by the dashed line (eqn. 4.17).

Combining the above, with the phase space factor (PSF) and the BW function, we write the following function to fit the $K\pi$ invariant mass spectrum.

$$f(M_{K\pi}) = BW(M_{K\pi}) \times PSF(M_{K\pi}) + RBG(M_{K\pi}) \tag{4.17}$$

in which, Y, B, C, M_{K^*} and Γ_{K^*} are five open parameters with their usual meaning. We can now extract the mass and width of the $K^*(892)$ from the fit.

Figures 4.5 and 4.6 show the $K\pi$ invariant mass spectrum at mid-rapidity $|y| < 0.5$ for the minimum bias d+Au collisions for K^{*0} and $K^{*\pm}$ respectively. Through the fit as given by eqn. 4.17, we get the K^{*0} mass, $M_{K^{*0}}$ as 886.5 $\pm$ 0.1 MeV with the width $\Gamma_{K^{*0}} = 55.9 \pm 0.4$ MeV. The raw K^{*0} yield is found to be $9.188 \times 10^8 \pm 6.9 \times 10^7$.

Using eqn. 4.17, the $K^{*\pm}$ mass, $M_{K^{*\pm}}$ has been found to be 888.7 $\pm$ 0.8 MeV and the width $\Gamma_{K^{*\pm}}$ is found to be 53.4 $\pm$ 3.1 MeV. The raw $K^{*\pm}$ yield is found to be $3.734 \times 10^{12} \pm 2.18 \times 10^{11}$.

In order to get the yield, mass and width of each of the two resonances *viz.* Δ and K^*, as a function of transverse momentum p_T, we have to carry out all the above calculations for given p_T-bins. Results of these are presented in a following section.

Figure 4.3, shows the fitted invariant mass spectra, for the Δ resonance, for various p_T bins, using eqn. 4.12. One can see that the fits are not so good which is primarily due to the non-inclusion of a reconstruction efficiency factor which also depends upon the invariant mass in a given p_T bin. A discussion on the reconstruction efficiency is given in the following section. However, for the K^* resonance eqn. 4.17 fits the invariant mass spectrum very well.

4.5 Efficiency Correction

The raw yields for Δ, K^{*0} and $K^{*\pm}$ as obtained for various p_T-bins now need to be corrected for the total "reconstruction efficiencies" which includes detector acceptance, response, tracking efficiency, and dynamical cut effects. The correction factors

for this are generated from simulated data using the following procedure.

To start with we generate a flat p_T distribution with about the same number of resonances (Δ or K^*) in every p_T-bin. These simulated particles, with a given Monte-Carlo ID (identification code), were then passed through GSTAR (the framework software package to run the STAR detector simulation using GEANT [111]) and TRS (the TPC Response Simulator). The resonances were then allowed to decay via their decay channels: $\Delta \rightarrow p\pi$, $K^{*0} \rightarrow K\pi$ and $K^{*\pm} \rightarrow K^0_S\pi^{\pm}$. The decayed daughters were then combined with the real raw event with only one (simulated) resonance daughter pair embedded in every event. This combined event, called a "simulated event", was then made to pass through the STAR reconstruction chain. The reconstruction efficiency was determined as the fraction of simulated events where the embedded resonances are recovered. Similarly, the reconstruction efficiency for a given p_T-bin can be determined from the fraction of reconstructed Monte-Carlo resonances out of the total number of simulated resonances embedded in that p_T-bin. However one has to remember that the above analysis is also to be carried out using the same dynamical cuts as discussed in Sections 4.2.2 and 4.2.3. This is expected to modify the reconstruction efficiency further.

The reconstruction efficiency as derived above has been studied as a function of collision centrality for the K^* resonance coming from d+Au collisions at $\sqrt{s_{NN}}$ =200 GeV. The results are shown in Fig. 4.7.

In the case of Δ, the reconstruction efficiency has been found to vary with the invariant mass. These results for various p_T bins are presented in Fig. 4.8. The distributions are fitted with a fourth order polynomial. For correcting the invariant mass spectrum for each p_T bin we have used the corresponding functional dependence between the efficiency and the invariant mass as given in the Fig. 4.8. Including this efficiency function, the final function used for fitting the invariant mass spectra for reconstructed Δ resonance is as given below.

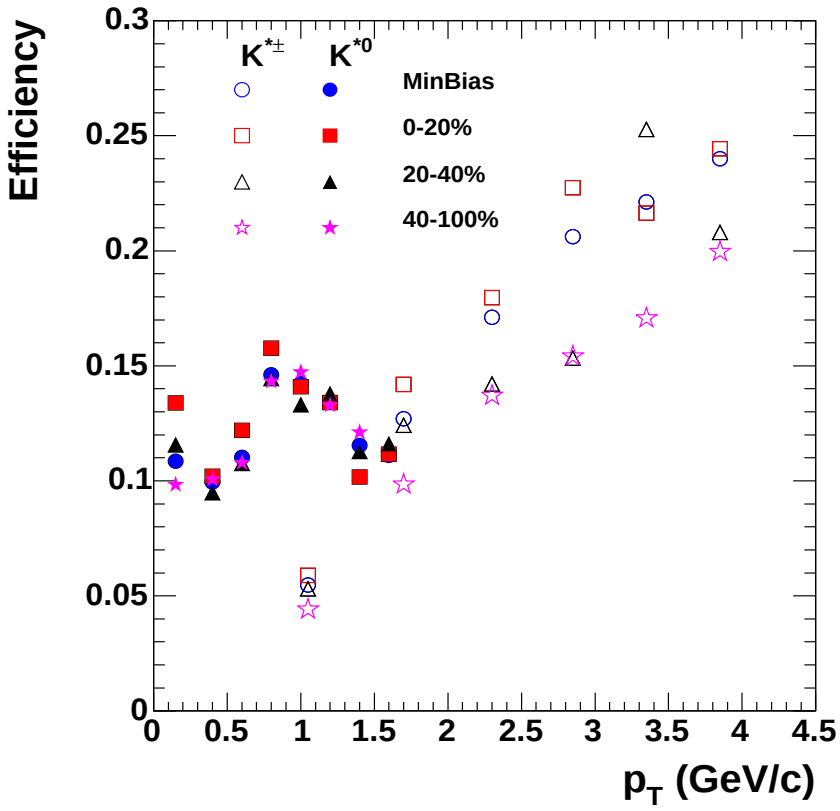

Figure 4.7: The total reconstruction efficiency as a function of p_T for K^{*0} and $K^{*\pm}$ for minimum bias as well as for different centralities of $d + Au$ collisions. The filled symbols are for neutral K^* and the open symbols are for charged K^*.

$$f(M_{p\pi}) = Efficiency\ function \times BW(M_{p\pi} \times PSF(M_{p\pi}) + RBG(M_{p\pi}) \quad (4.18)$$

Figure 4.9 shows the $p\pi$ invariant mass spectrum at the mid-rapidity $|y| < 0.5$ for the minimum bias $d + Au$ collisions. By fitting with the eqn. 4.18, we get the Δ mass, M_Δ as 1179 ± 1 MeV and the width Γ_Δ as 117.3 ± 4.6 MeV. The raw $\Delta(1232)$ is found to be $4.191 \times 10^7 \pm 1.24 \times 10^6$.

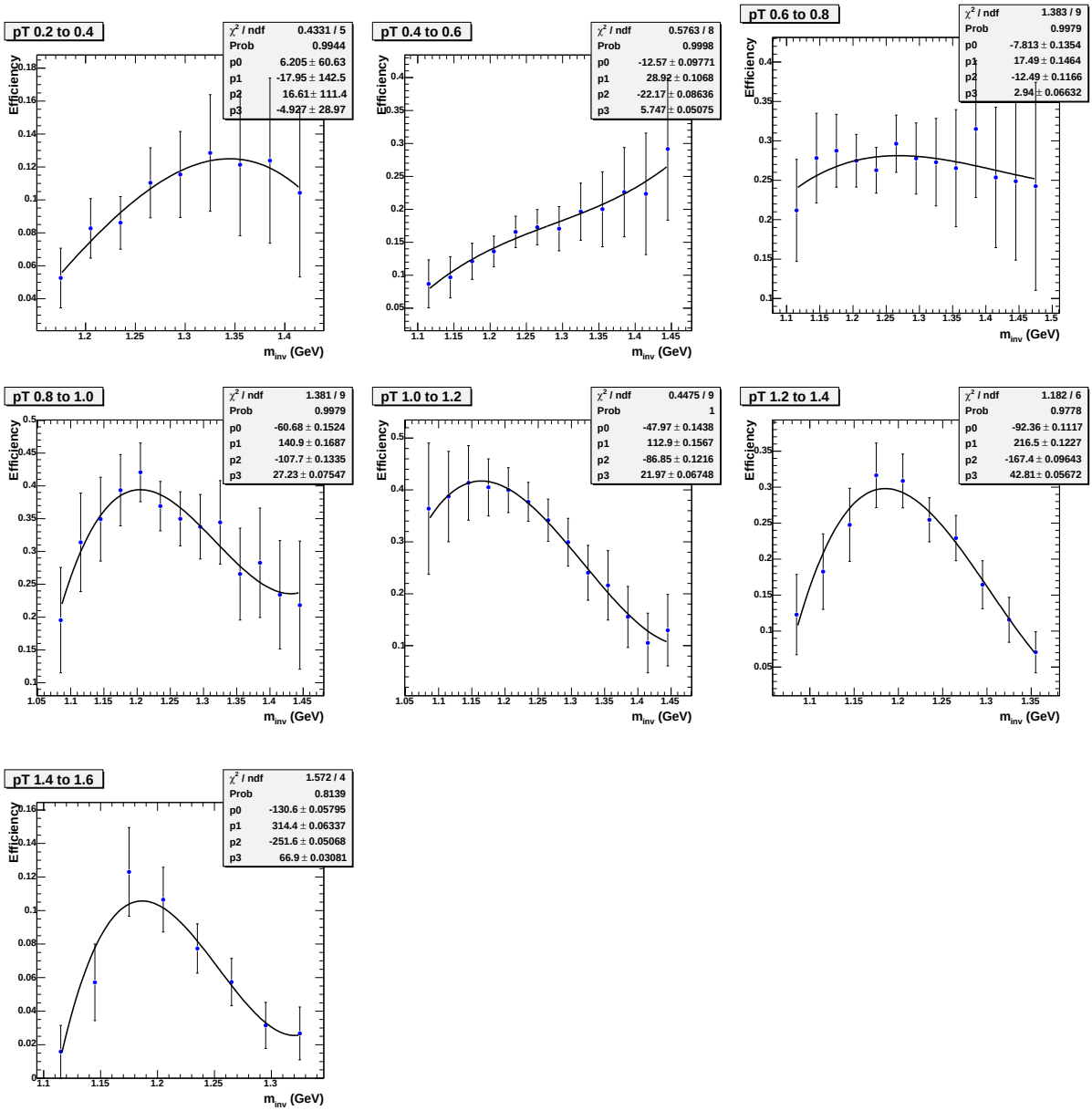

Figure 4.8: The total reconstruction efficiency as a function of invariant mass for different p_T bins. The solid line represents a fourth order polynomial fitting function.

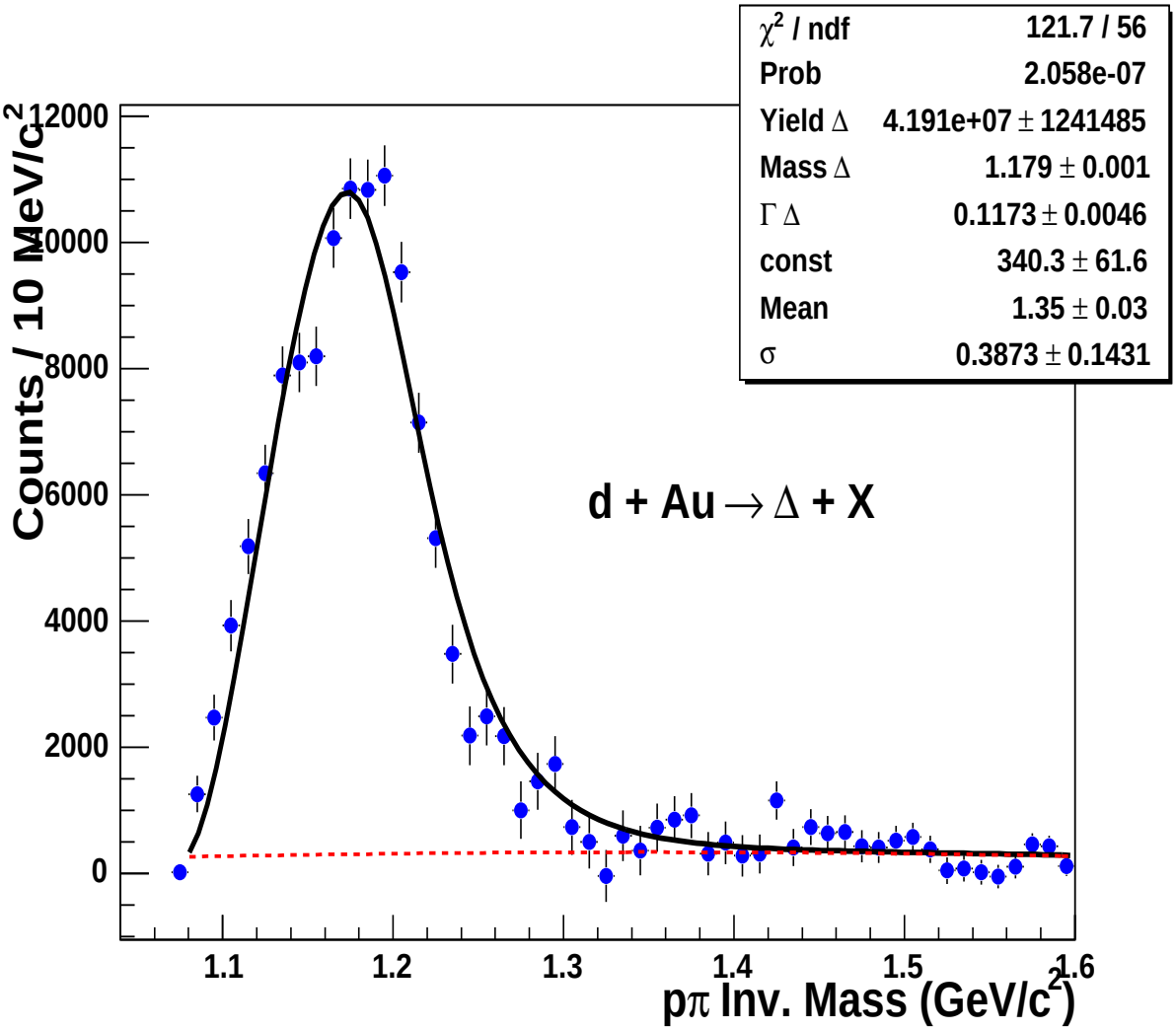

Figure 4.9: The $p\pi$ invariant mass distribution fitted to eqn. 4.18 to extract the $\Delta(1232)$ yield in $d + Au$ collisions at $\sqrt{s_{NN}}$=200 GeV. The solid curve represents the Breit-Wigner fit to the data points with a Gaussian background as shown by the dashed line (eqn. 4.11).

4.5.1 Correction for Branching Ratio

As has been mentioned earlier (Section 4.5), in order to correct the raw yields for Δ, K^{*0} and $K^{*\pm}$ one needs to consider the reconstruction efficiency as determined from simulations. In addition, the yields for K^{*0} and $K^{*\pm}$ need to be corrected for the corresponding branching ratios.

We know from [56] that, K^{*0} mesons decays $\sim$100% of the time via the following two decay channels: (i) into two oppositely charged daughters ($K^{*0} \rightarrow K^{+}\pi^{-}$ or $K^{*0} \rightarrow K^{-}\pi^{+}$) and (ii) into two neutral daughters ($K^{*0} \rightarrow K^{0}\pi^{0}$). From isospin considerations, we know that 2/3 of the K^{*0} mesons would decay into the channel with oppositely charged daughters, 1/3 of them decaying into the channel with neutral daughters. Since we measure the K^{*0} through the decay channel with two oppositely charged daughters, the K^{*0} yields have to be corrected using the branching ratio 2/3. Similarly, $K^{*\pm}$ mesons decay $\sim$100% via the following two decay channels: (i) into a neutral kaon and a charged pion ($K^{*\pm} \rightarrow K^{0}\pi^{\pm}$) and (ii) into a charged kaon and a neutral pion ($K^{*\pm} \rightarrow K^{\pm}\pi^{0}$). Again from isospin considerations we know that, 2/3 of the $K^{*\pm}$ mesons would decay producing a neutral kaon, 1/3 of them decaying into a neutral pion. But we measure the $K^{\pm}$ signal by selecting the K^{0}_{S} mesons via the decay channel $K^{0}_{S} \rightarrow \pi^{+}\pi^{-}$. Also we have to consider that only half of the K^{0} mesons decay as a K^{0}_{S} and the other half decay as a K^{0}_{L} which we don't measure. The branching ratio for $K^{0}_{S} \rightarrow \pi^{+}\pi^{-}$ is 68.61% [56]. Therefore the total decay branching ratio is equal to 2/3$\times$1/2$\times$ 0.6861 which is equal to 0.2287. The same value is also valid for K^{*-} as well. For the case of Δ, we don't need to do the correction for branching ratio, because Δ decays >99% of the time via proton and pion.

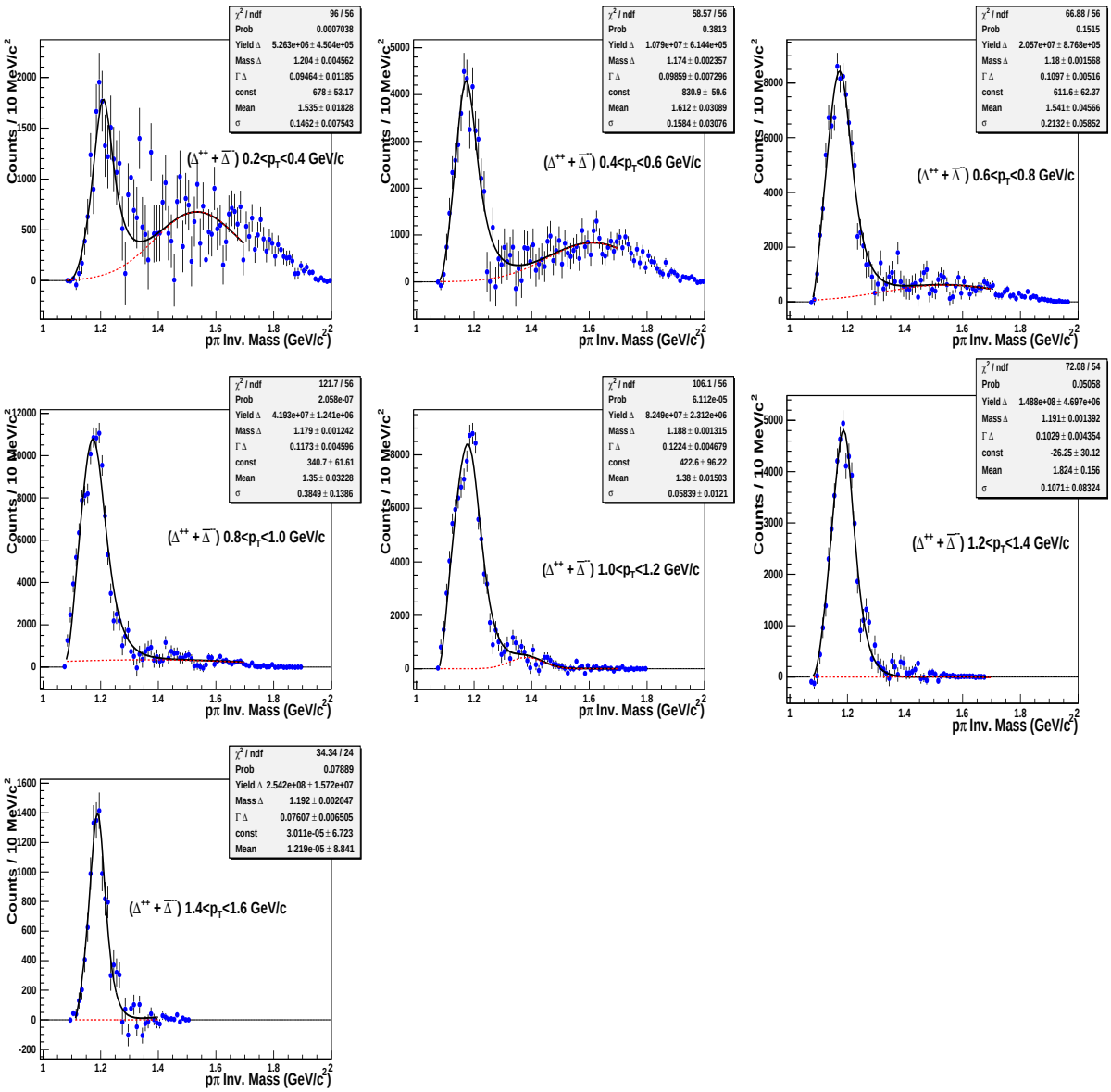

Figure 4.10: The $p\pi$ invariant mass distributions for different p_T bins, each having bin width 0.2 GeV/c for minimum bias trigger. The solid curves stand for the fit function using eqn. 4.18 and the dashed lines stand for the Gaussian residual background.

4.6 Transverse momentum spectra for $\triangle(1232)$ and $K^*(892)$ in d+Au Collisions

Figure 4.10 shows the $p\pi$ invariant mass distributions for seven p_T bins between 0.2 to 1.6 GeV/c, at bin widths of 0.2 GeV/c. Similarly, Fig. 4.11, 4.12, 4.13 show the $p\pi$ invariant mass distributions for (0-20)%, (20-40)% and (40-100)% of d+Au collision centralities respectively within the p_T range between 0.2 to 1.6 GeV/c. Similar results for K^{*0} and $K^{*\pm}$ reconstruction for various p_T bins and different centralities *viz.* minimum bias, 0-20%, 20-40%, 40-100% are shown in Figures 4.14-4.21.

However, in case of K^*, the baseline results regarding yield, as shown in the Figures 4.14-4.21 have been obtained by fixing the width parameter at 50.7 MeV. One can further see that the p_T ranges for K^{*0} and $K^{*\pm}$ are 0-1.7 GeV/c and 0.7-4.1 GeV/c respectively.

Figure 4.22 shows the raw charged K^* yield determined from the average of the raw yields of K^{*+} and K^{*-} as a function p_T, for various collision centralities. The raw yields for the neutral K^*, determined from the average raw yields of K^{*0} and $\overline{K^{*0}}$, as functions of p_T, for various centralities, are also shown in the same figure for comparison. The data points for minimum bias, 20-40%, 40-100% centrality are scaled by factors of 10, 0.33 and 0.1, respectively, in order to show easily the difference between different collision centralities.

The corrected invariant yields, $d^2N/(2\pi p_T dp_T dy)$ for Δ^{++} at $|y| < 0.5$ in each p_T bin for minimum bias and for different collisions centrality in d+Au collisions are shown in Fig. 4.23. The same values for each p_T bin are listed also in Table 4.4. In addition to the inverse slope parameter of the p_T spectrum, which is related to the "freeze-out" temperature, it is also possible to get an estimation of the rapidity density, dN/dy from the above data [66].

In terms of p_T, the Δ transverse mass is defined as: $m_T = \sqrt{m_\Delta^2 + p_T^2}$, where m_Δ is the Δ natural mass, 1232 MeV, one can see that, $p_T dp_T = m_T dm_T$. Using this, we can write the invariant yield $d^2N/(2\pi p_T dp_T dy)$ at mid-rapidity as:

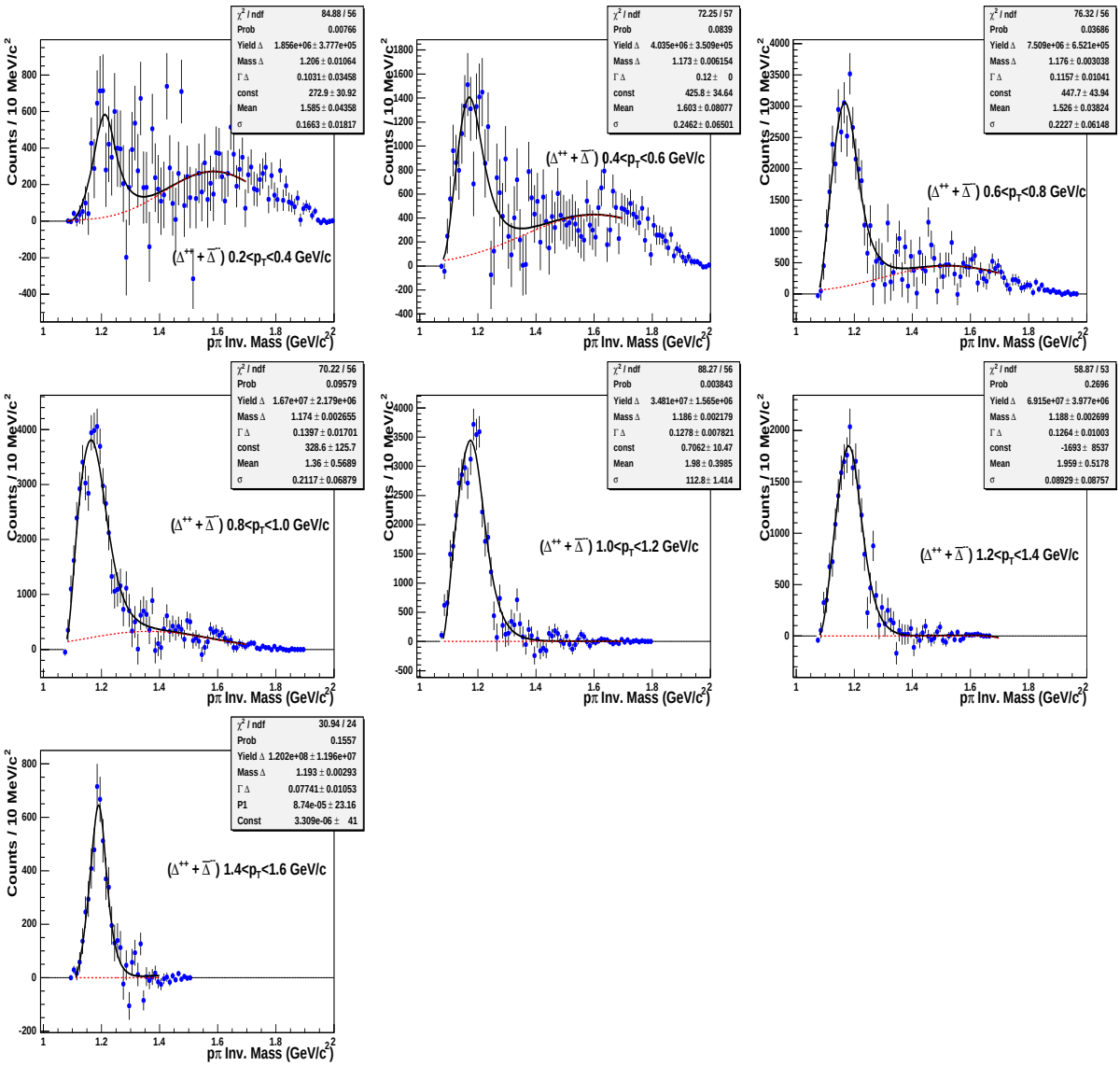

Figure 4.11: The $p\pi$ invariant mass distributions for different p_T bins, each having bin width 0.2 GeV/c for (0-20)% $d + Au$ collision centrality. The solid curves stand for the fit function using eqn. 4.18 and the dashed lines stand for the Gaussian residual background.

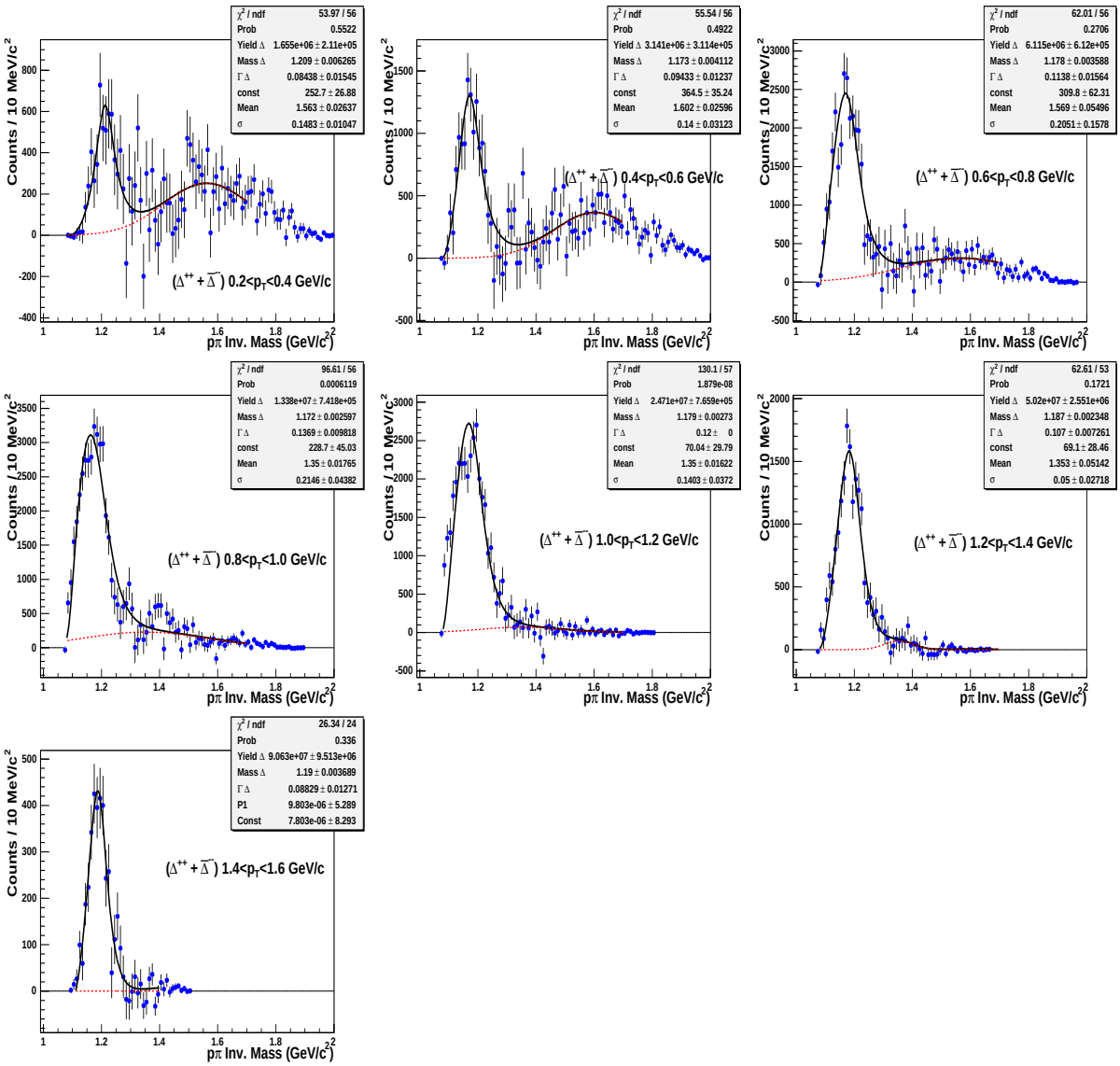

Figure 4.12: The $p\pi$ invariant mass distributions for different p_T bins, each having bin width 0.2 GeV/c for (20-40)% $d + Au$ collision centrality. The solid curves stand for the fit function using eqn. 4.18 and the dashed lines stand for the Gaussian residual background.

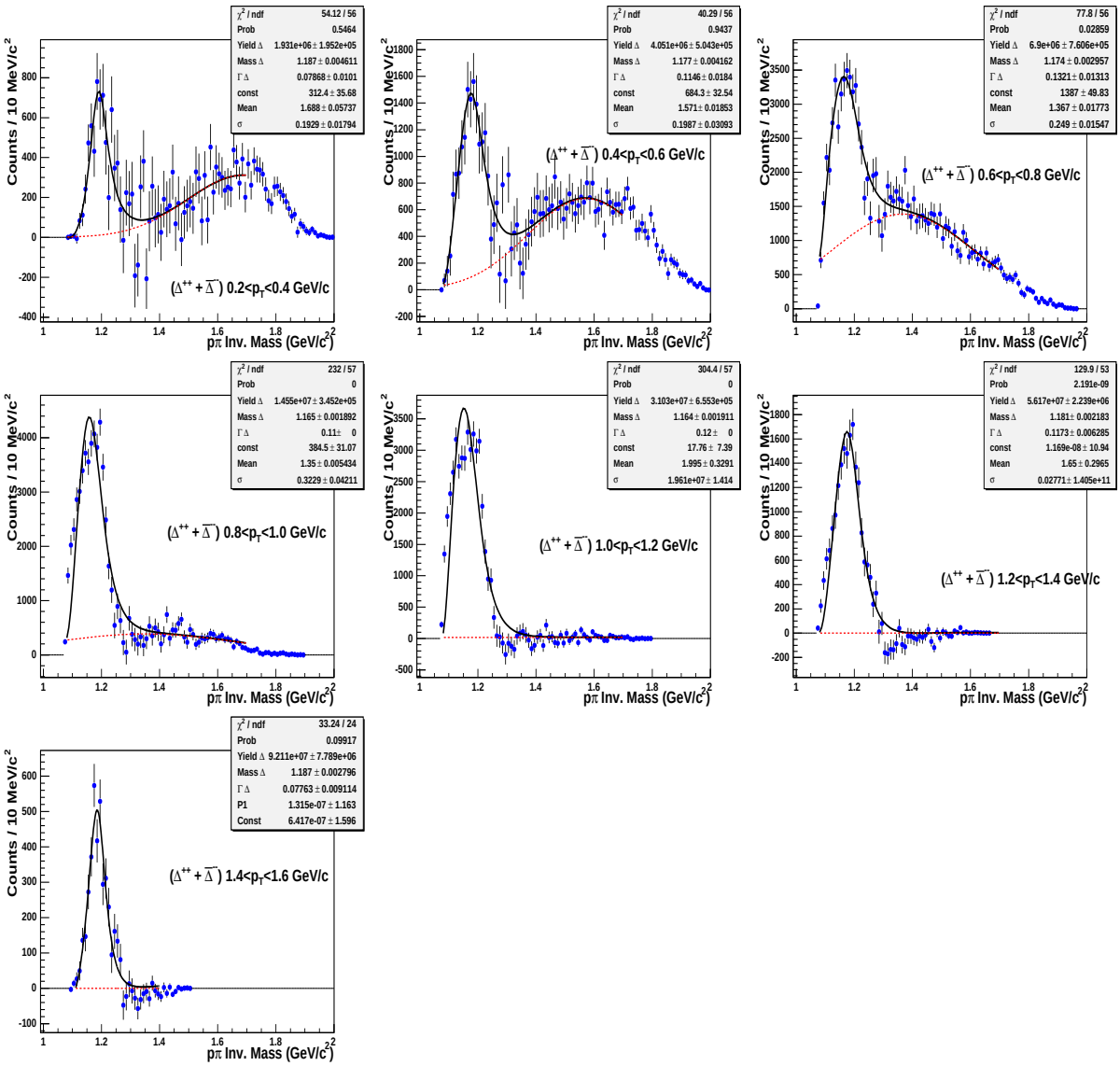

Figure 4.13: The $p\pi$ invariant mass distributions for different p_T bins, each having bin width 0.2 GeV/c for (40-100)% $d+Au$ collision centrality. The solid curves stand for the fit function using eqn. 4.18 and the dashed lines stand for the Gaussian residual background.

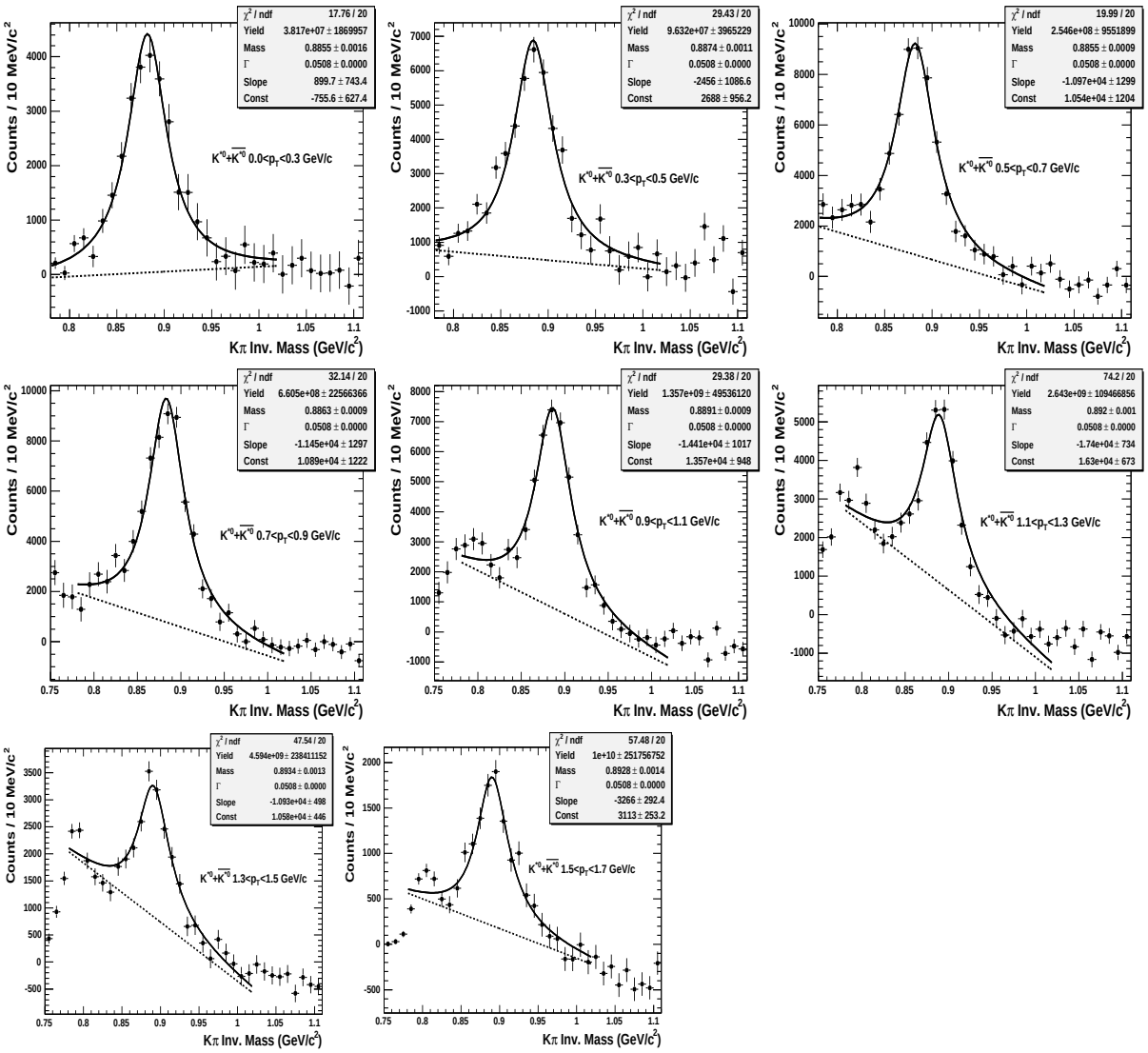

Figure 4.14: The $K\pi$ invariant mass distributions for different p_T bins, each having bin width 0.2 GeV/c for minimum bias trigger. The solid curves stand for the fit function using eqn. 4.17 and the dashed lines stand for the linear residual background.

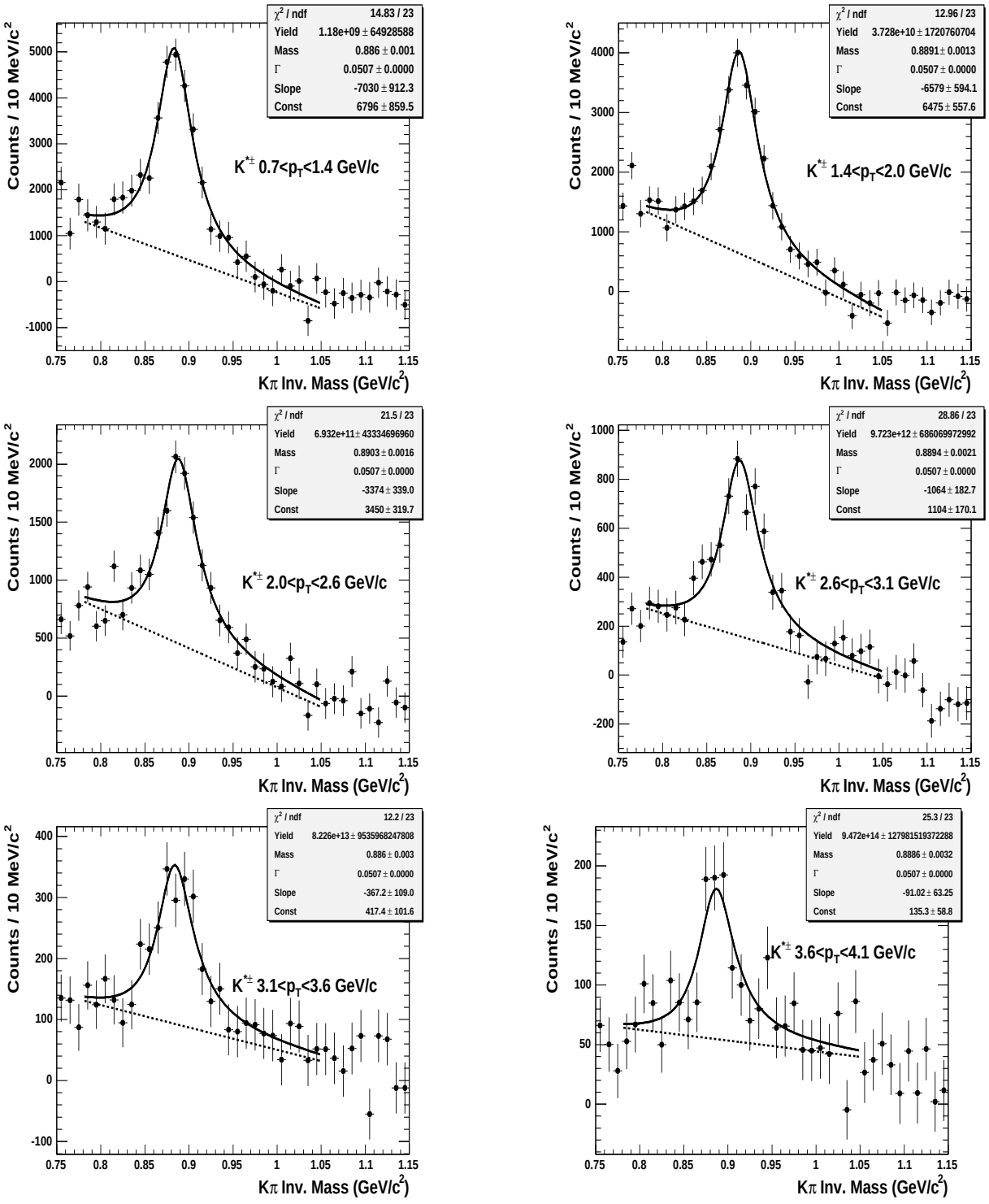

Figure 4.15: The $K^0_S\pi^\pm$ invariant mass distributions for different p_T bins, each having bin width 0.7 GeV/c for (0-20)% centrality. The solid curves stand for the fit function using eqn. 4.17 and the dashed lines stand for the linear residual background.

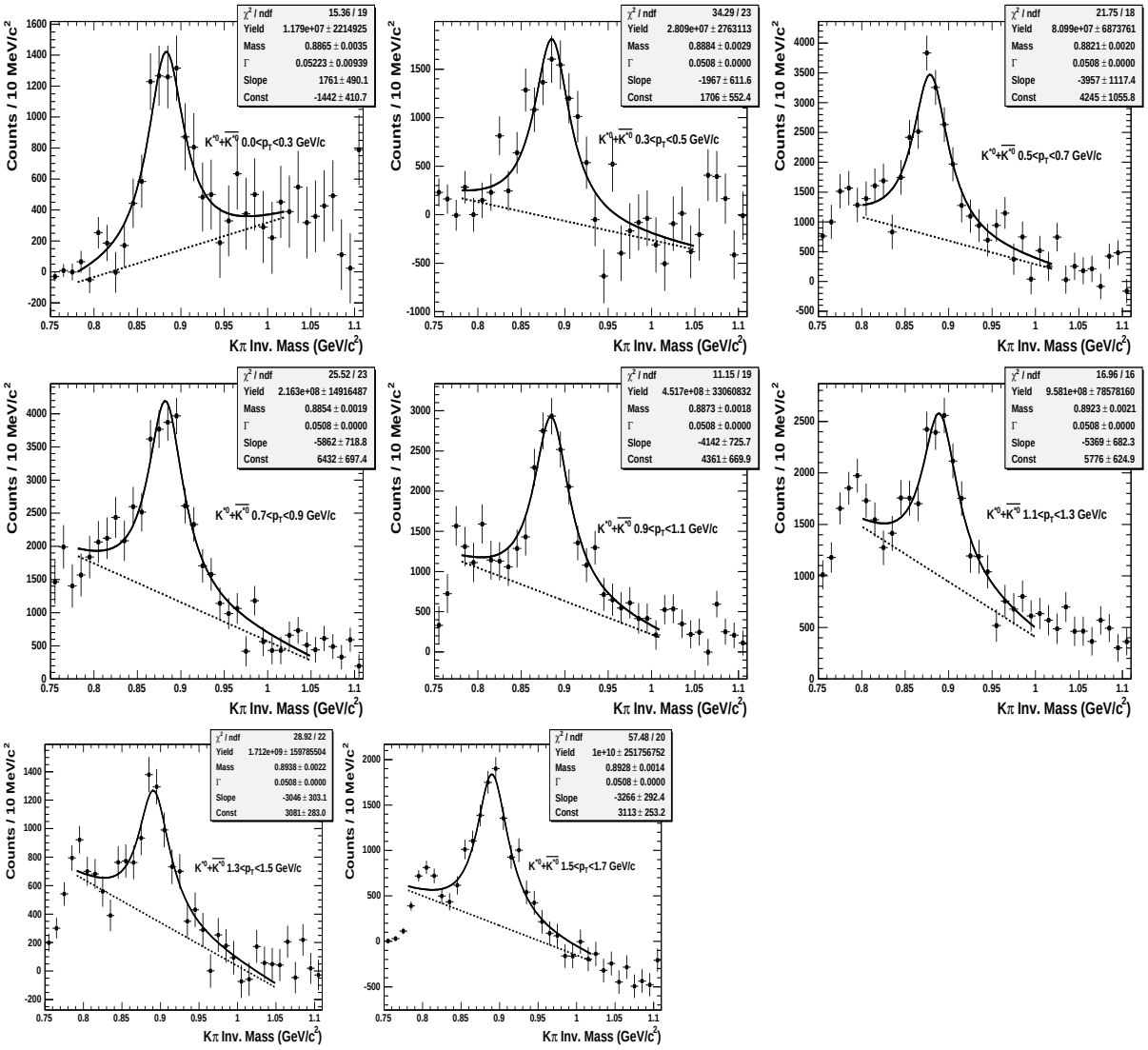

Figure 4.16: The $K\pi$ invariant mass distributions for different p_T bins, each having bin width 0.2 GeV/c for (0-20)% centrality. The solid curves stand for the fit function using eqn. 4.17 and the dashed lines stand for the linear residual background.

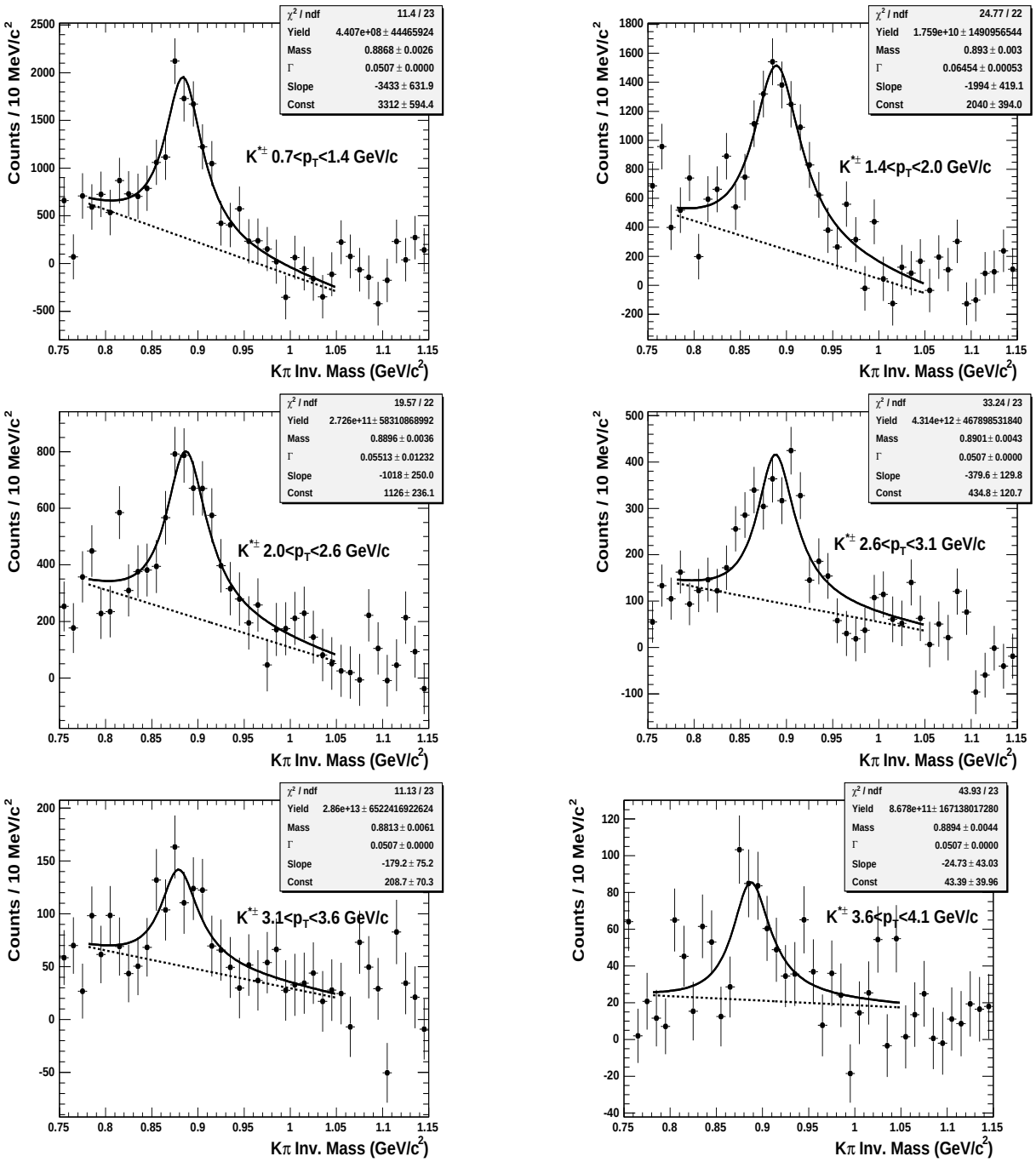

Figure 4.17: The $K^0_S\pi^\pm$ invariant mass distributions for different p_T bins, each having bin width 0.7 GeV/c for (20-40)% centrality. The solid curves stand for the fit function using eqn. 4.17 and the dashed lines stand for the linear residual background.

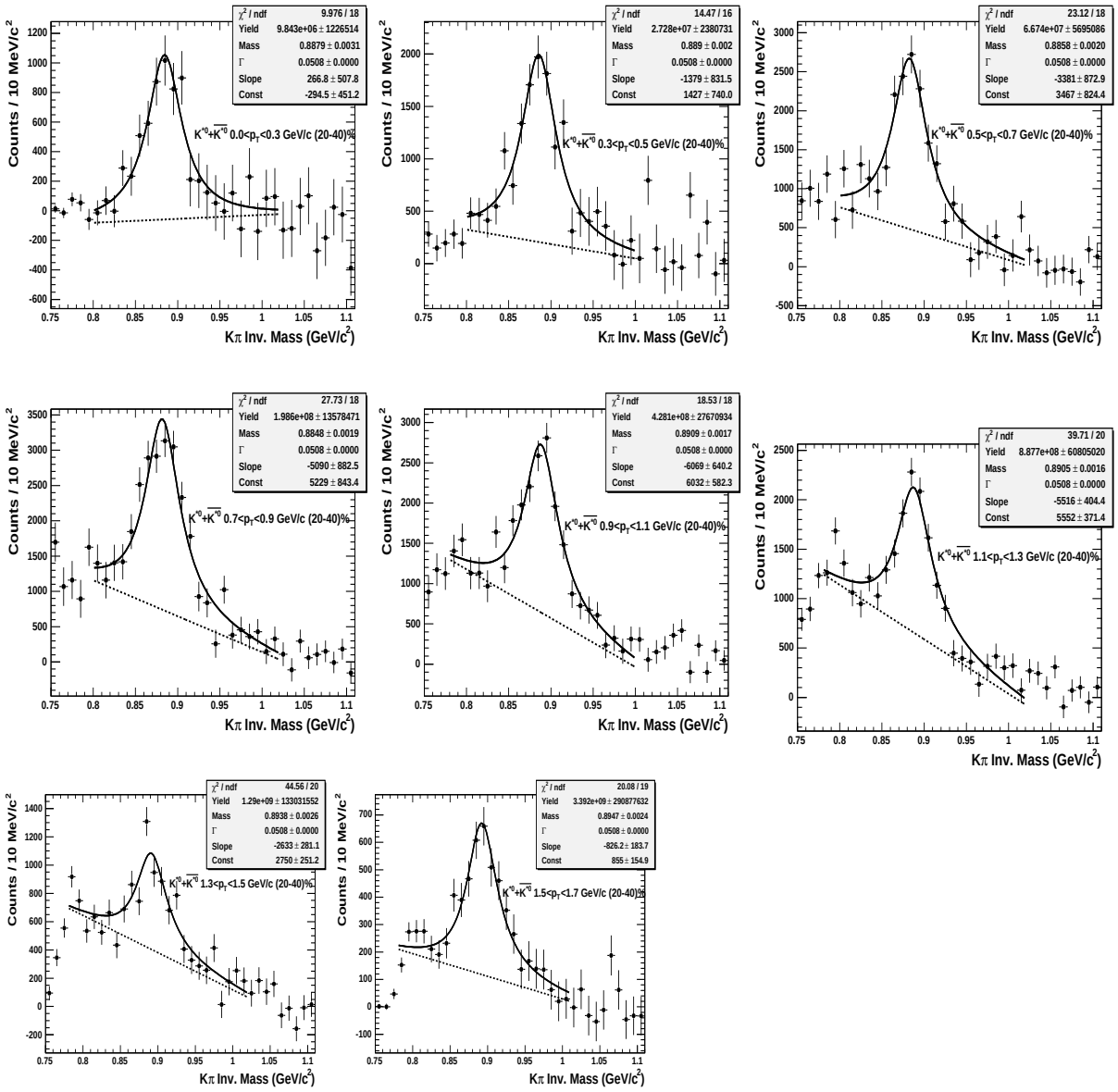

Figure 4.18: The $K\pi$ invariant mass distributions for different p_T bins, each having bin width 0.2 GeV/c for (20-40)% centrality. The solid curves stand for the fit function using eqn. 4.17 and the dashed lines stand for the linear residual background.

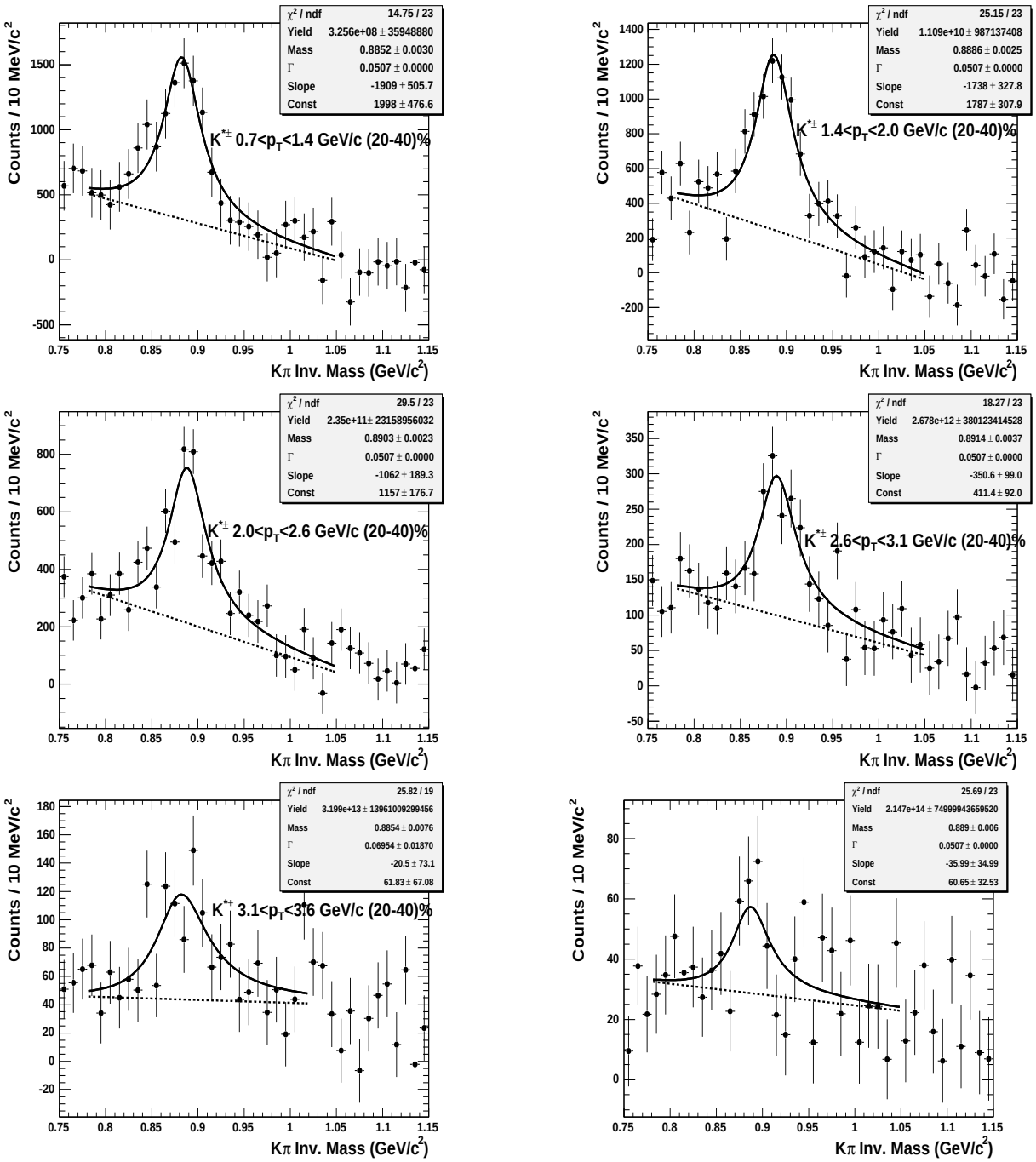

Figure 4.19: The $K^0_S\pi^\pm$ invariant mass distributions for different p_T bins, each having bin width 0.7 GeV/c for (20-40)% centrality. The solid curves stand for the fit function using eqn. 4.17 and the dashed lines stand for the linear residual background.

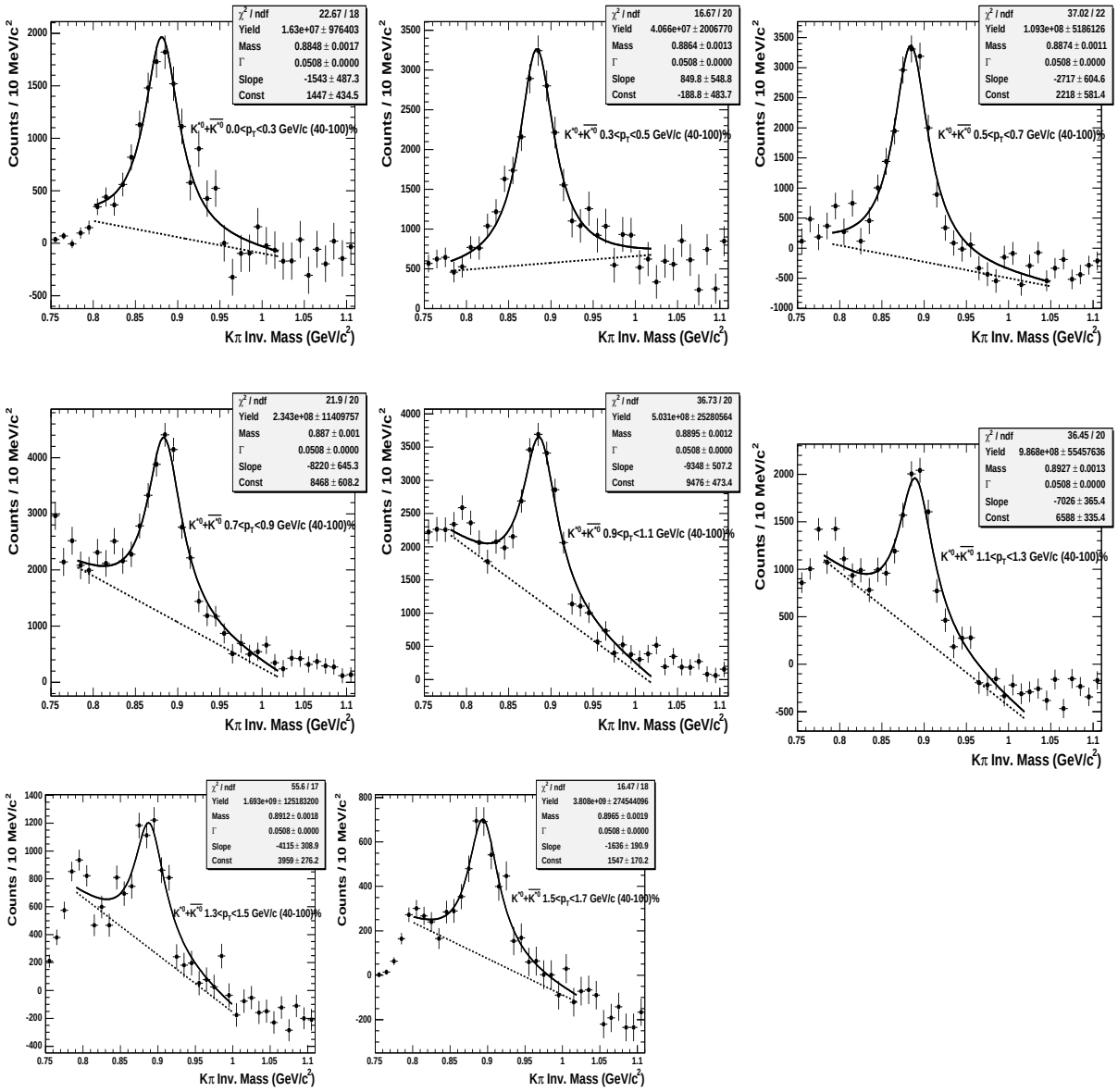

Figure 4.20: The $K\pi$ invariant mass distributions for different p_T bins, each having bin width 0.2 GeV/c for (40-100)% centrality. The solid curves stand for the fit function using eqn. 4.17 and the dashed lines stand for the linear residual background.

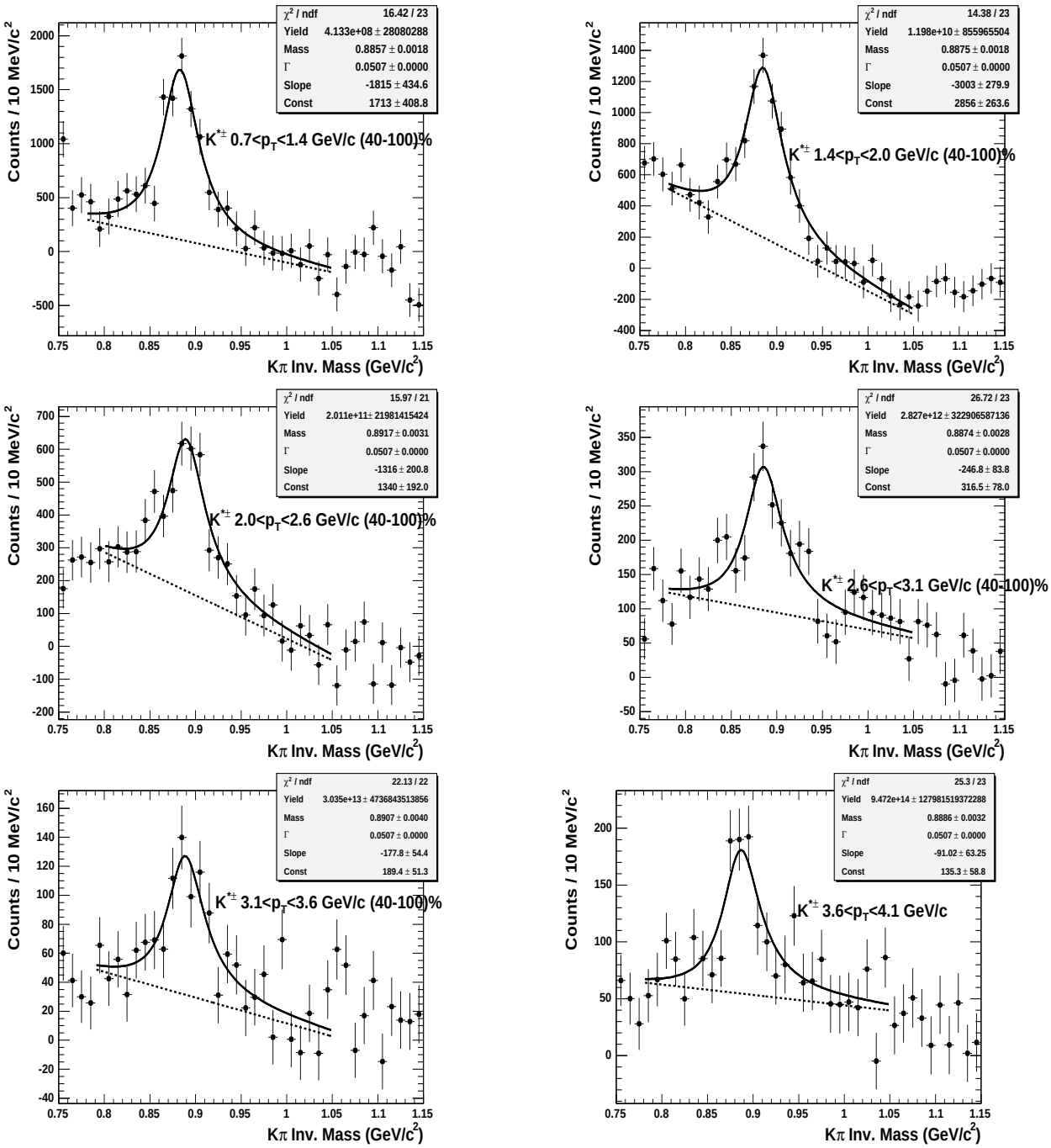

Figure 4.21: The $K^0_S\pi^\pm$ invariant mass distributions for different p_T bins, each having bin width 0.7 GeV/c for (40-100)% centrality. The solid curves stand for the fit function using eqn. 4.17 and the dashed lines stand for the linear residual background.

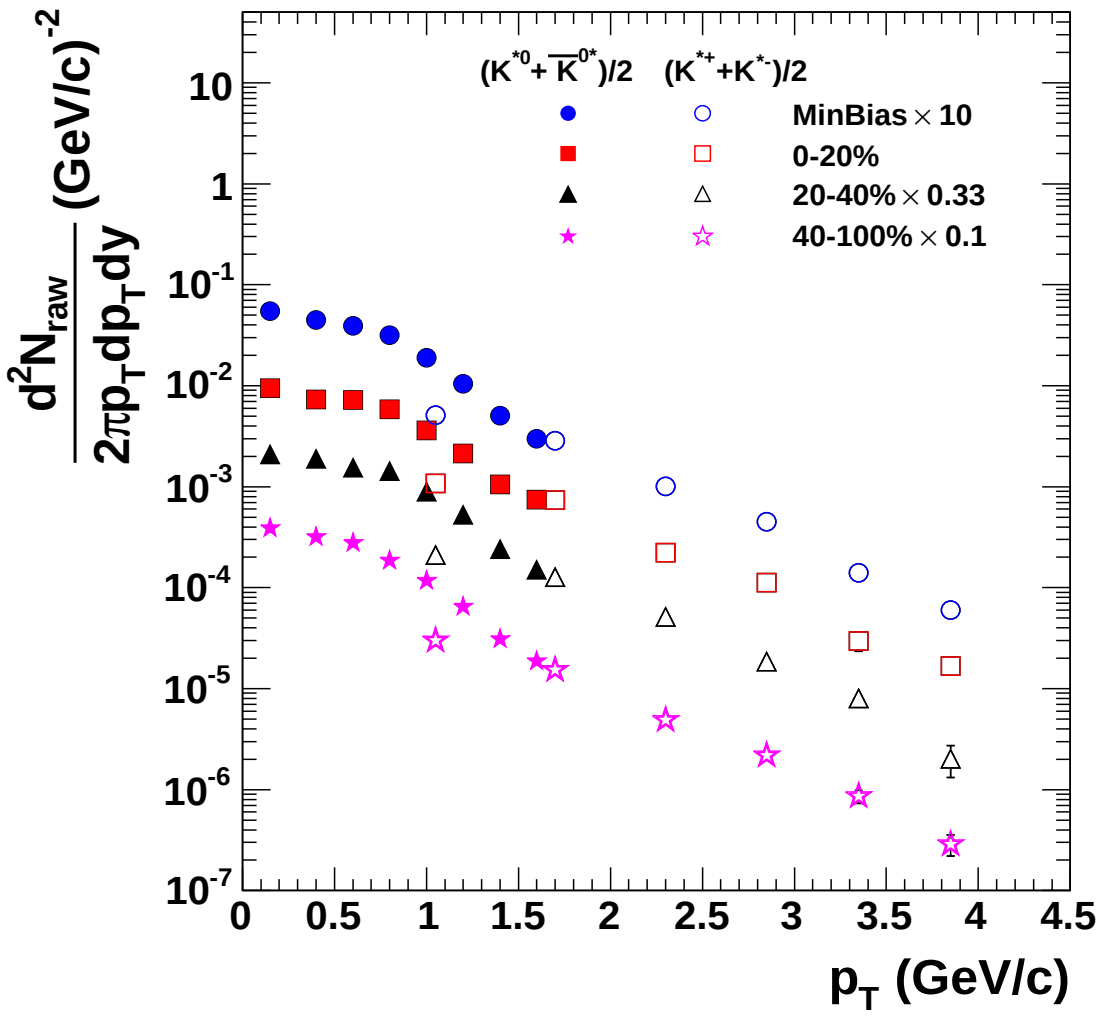

Figure 4.22: The raw yield $d^2N_{raw}/(2\pi p_T dp_T dy)$ for the average of the K^{*0} and $\overline{K^{*0}}$ yields and the average of K^{*+} and K^{*-} raw yields as a function of p_T at $|y| < 0.5$ in d+Au collisions for minimum bias as well as for different centralities. Filled symbols are for neutral K^* and open symbols are for charged K^*.

$$\frac{1}{2\pi p_T}\frac{d^2N}{dp_T dy} = \frac{1}{2\pi m_T}\frac{d^2N}{dm_T dy} \tag{4.19}$$

Now, one can write

$$\frac{1}{2\pi m_T}\frac{d^2N}{dy dm_T} = A \times exp[-(m_T - m_\Delta)/B] \tag{4.20}$$

The p_T spectra for the Δ resonances can, in principle be fitted to the above function to determine the inverse slope parameter B which we normally write as T_{eff} or T. In view of this we replace B by a parameter T. The strength parameter, A is thus related to the rapidity density, dN/dy which can be seen from a direct integration of eqn. 4.20, as shown below.

$$\frac{1}{2\pi}\frac{dN}{dy} = \int_{m_\Delta}^{+\infty} A \times exp[-(m_T - m_\Delta)/T] m_T dm_T \tag{4.21}$$

Integrating we get,

$$\int_{m_\Delta}^{+\infty} A \times exp[-(m_T - m_\Delta)/T] m_T dm_T = AT(m_\Delta + T) \tag{4.22}$$

which results in

$$A = \frac{dN/dy}{2\pi T(m_\Delta + T)} \tag{4.23}$$

So, the final function which has been used to fit the corrected yield versus transverse momentum in Fig. 4.23 is

$$\frac{1}{2\pi p_T}\frac{d^2N}{dm_T dy} = \frac{dN/dy}{2\pi T(m_\Delta + T)} exp[-(m_T - m_\Delta)/T] \tag{4.24}$$

which has two open parameters viz. the yield dN/dy at mid-rapidity and the inverse slope parameter T. Results of such a fit to the p_T spectra for Δ resonance are listed in Table 4.5 with their statistical and systematic uncertainties.

Similarly, the corrected invariant yields for the K^*, at mid-rapidity, as given by $d^2N/(2\pi p_T dp_T dy)$, for various p_T and centrality bins (minimum bias, 0-20%, 20-40%, 40-100%) in d+Au collisions, are shown in Fig. 4.24. The values for K^{*0} are the average of the values for K^{*0} and $\overline{K}^{*0}$. Similarly the values shown for $K^{*\pm}$ are the

p_T (GeV/c)	Minimum bias	(0-20)%	(20-40)%	(40-100)%
0.2 - 0.4	(2.58±0.22)× 10^{-2}	(4.7±0.9)× 10^{-2}	(3.7±0.4)× 10^{-2}	(1.79±0.18)× 10^{-2}
0.4 - 0.6	(2.2±0.12)× 10^{-2}	(4.1±0.36)× 10^{-2}	(2.9±0.29)× 10^{-2}	(1.34±0.16)× 10^{-2}
0.6 - 0.8	(1.5±0.06)× 10^{-2}	(2.9±0.25)× 10^{-2}	(2.0±0.2)× 10^{-2}	(8.34±0.9)× 10^{-3}
0.8 - 1.0	(1.0±0.03)× 10^{-2}	(2.2±0.29)× 10^{-2}	(1.5±0.08)× 10^{-2}	(6.76±0.16)× 10^{-3}
1.0 - 1.2	(7.0±0.19)× 10^{-3}	(1.5±0.07)× 10^{-2}	(9.7±0.3)× 10^{-3}	(4.7±0.09)× 10^{-3}
1.2 - 1.4	(4.2±0.13)× 10^{-3}	(1.0±0.05)× 10^{-2}	(6.48±0.3)× 10^{-3}	(2.67±0.1)× 10^{-3}
1.4 - 1.6	(2.4±0.14)× 10^{-3}	(0.6±0.06)× 10^{-2}	(3.7±0.39)× 10^{-3}	(1.48±0.12)× 10^{-3}

Table 4.4: The average values of Δ^{++} and $\overline{\Delta}^{--}$ invariant yields $d^2N/(2\pi p_T dp_T dy)$ in each p_T bin for minimum bias and different collision centralities.

Centrality	dN/dy	T (MeV)
Minimum bias	0.0822 ± 0.0012±0.01	284 ± 7±45
0-20%	0.177±0.005±0.02	328 ± 16±52
20-40%	0.116 ± 0.0026±0.014	302 ± 14±48
40-100%	0.053 ± 0.0008±0.006	290 ± 9±46

Table 4.5: The average yield of Δ^{++} and $\overline{\Delta}^{--}$ at $|y| < 0.5$ and the inverse slope parameter T for minimum bias and and different collision centralities with their stat. uncertainties and sys. uncertainties

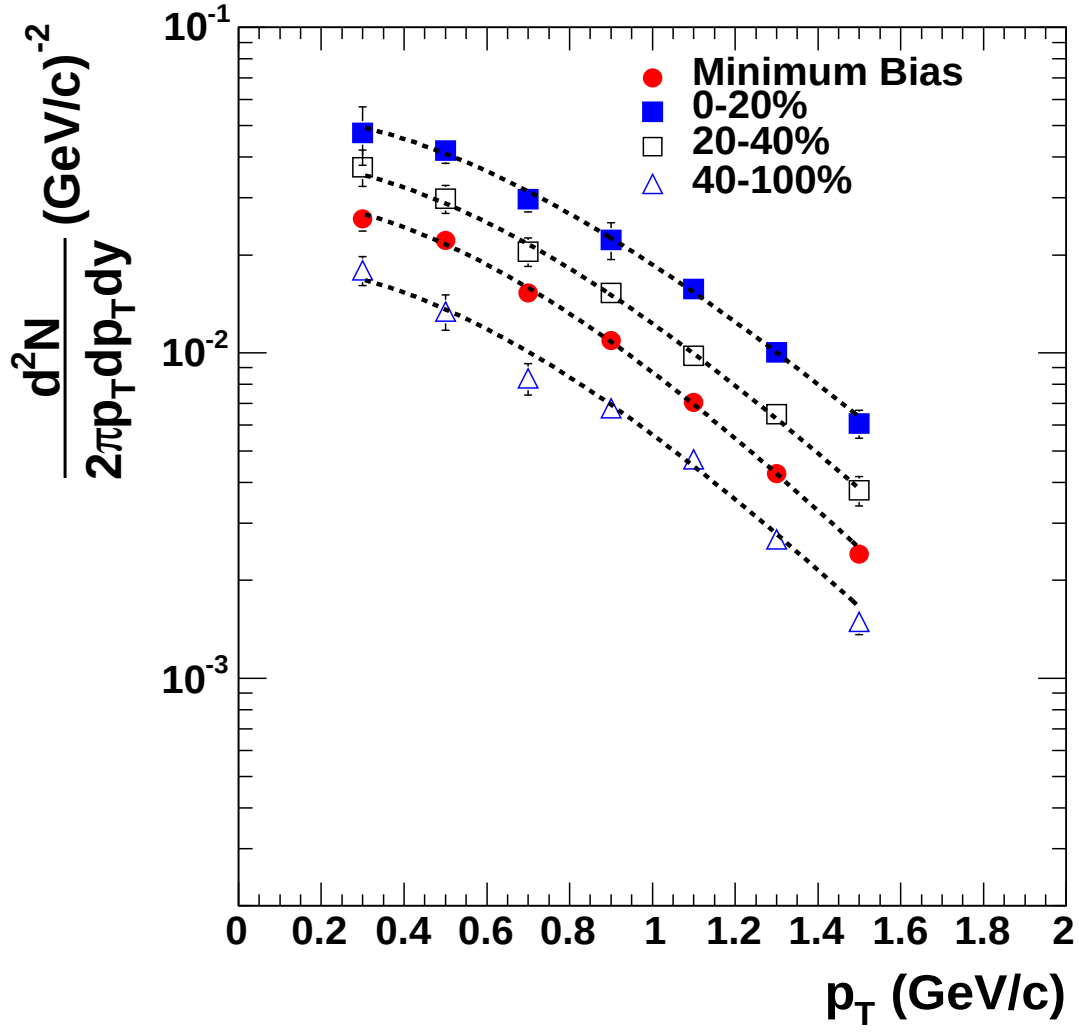

Figure 4.23: The corrected yield for average of Δ^{++} and $\overline{\Delta}^{--}$ as a function of p_T at $|y| < 0.5$ in $d + Au$ collisions for minimum bias as well as for different centralities. The spectra are fitted with exponential function as defined in eqn. 4.24.

average values of yields obtained for the two charged K^* mesons. These values are also presented in Tables. 4.6 and 4.7 for neutral and charged K^* mesons respectively.

We know that, at higher transverse momentum ($p_T > 1.5$ GeV/c) particle production is dominated by hard processes [114]. Compared to this, soft processes dominate at low transverse momentum ($p_T < 1.5$ GeV/c). Thus, we expect to observe a power-law shape in the p_T distribution for $p_T > 1.5$ GeV. On the other hand, the low p_T part ($p_T < 1.5$ GeV/c) of the p_T distribution is expected to be still exponential in nature. Based on the above logic, when hard processes dominate, it has been suggested to use a Levy function which fits well to the data over the entire p_T range [114]. We have carried out such a fit to the K^* data using the Levy function as given below. We write

$$\frac{1}{2\pi p_T}\frac{d^2N}{dp_T dy} = A[1 + \frac{m_T - m_{K^*}}{nT}]^{-n} \tag{4.25}$$

in which the parameter A is a constant proportional to the yield at mid-rapidity, T is the inverse slope parameter, n being the power law exponent.

After integration with respect to m_T we get,

$$A = \frac{(dN/dy)(n-1)(n-2)}{2\pi nT(nT + m_{K^*}(n-2))} \tag{4.26}$$

The final function which has been used to fit the K^* yield distribution over the entire p_T range, as shown in Fig. 4.24, is given by

$$\frac{1}{2\pi p_T}\frac{d^2N}{dp_T dy} = \frac{(dN/dy)(n-1)(n-2)}{2\pi nT(nT + m_{K^*}(n-2))}[1 + \frac{m_T - m_{K^*}}{nT}]^{-n} \tag{4.27}$$

There are three open parameters in the fit function, which represent the mid-rapidity yield dN/dy, inverse slope parameter T and the exponent n. The results from the fitting of the p_T distributions are listed in Table 4.8.

From the Table 4.5 and Table 4.8, one can see that the mid-rapidity yield dN/dy for Δ and K^* increases with increase in centrality of the collisions.

p_T (GeV/c)	Minimum bias	(0-20)%	(20-40)%	(40-100)%
0.0 - 0.3	(5.97±0.29)× 10^{-2}	(8.4±1.57)× 10^{-2}	(6.4±0.79)× 10^{-2}	(4.7±0.28)× 10^{-2}
0.3 - 0.5	(5.34±0.22)× 10^{-2}	(8.54±0.84)× 10^{-2}	(7.07±0.6)× 10^{-2}	(3.73±0.18)× 10^{-2}
0.5 - 0.7	(4.23±0.15)× 10^{-2}	(7.06±0.6)× 10^{-2}	(5.09±0.4)× 10^{-2}	(3.07±0.14)× 10^{-2}
0.7 - 0.9	(2.57±0.08)× 10^{-2}	(4.4±0.3)× 10^{-2}	(3.5±0.24)× 10^{-2}	(1.54±0.07)× 10^{-2}
0.9 - 1.1	(1.59±0.05)× 10^{-2}	(3.03±0.2)× 10^{-2}	(2.39±0.15)× 10^{-2}	(9.47±0.47)× 10^{-3}
1.1 - 1.3	(9.24±0.38)× 10^{-3}	(1.89±0.15)× 10^{-2}	(1.36±0.09)× 10^{-2}	(5.8±0.32)× 10^{-3}
1.3 - 1.5	(5.17±0.26)× 10^{-3}	(1.2±0.11)× 10^{-2}	(7.63±0.68)× 10^{-3}	(3.04±0.22)× 10^{-3}
1.5 - 1.7	(3.19±0.08)× 10^{-3}	(0.79±0.16)× 10^{-2}	(4.64±0.39)× 10^{-3}	(1.88±0.13)× 10^{-3}

Table 4.6: The average of K^{*0} and $\overline{K}^{*0}$ invariant yields $d^2N/(2\pi p_T dp_T dy)$ in each p_T bin for minimum bias and different collision centralities.

p_T (GeV/c)	Minimum bias	(0-20)%	(20-40)%	(40-100)%
0.7 - 1.4	(1.05±0.05)× 10^{-2}	(2.06±0.2)× 10^{-2}	(1.35±0.14)× 10^{-2}	(7.6±0.5)× 10^{-3}
1.4 - 2.0	(2.53±0.11)× 10^{-3}	(5.86±0.5)× 10^{-3}	(3.46±0.3)× 10^{-3}	(1.7±0.12)× 10^{-3}
2.0 - 2.6	(6.7±0.4)× 10^{-4}	(1.41±0.15)× 10^{-3}	(1.22±0.4)× 10^{-3}	(4.03±0.4)× 10^{-4}
2.6 - 3.1	(2.4±0.17)× 10^{-4}	(5.59±0.6)× 10^{-4}	(4.08±0.57)× 10^{-4}	(1.6±0.18)× 10^{-4}
3.1 - 3.6	(0.7±0.08)× 10^{-4}	(1.55±0.3)× 10^{-4}	(1.08±0.18)× 10^{-4}	(5.7±0.85)× 10^{-5}
3.6 - 4.1	(0.28±0.38)× 10^{-4}	(0.77±0.14)× 10^{-4}	(0.33±0.11)× 10^{-4}	(1.6±0.39)× 10^{-5}

Table 4.7: The average of K^{*+} and K^{*-} invariant yields $d^2N/(2\pi p_T dp_T dy)$ in each p_T bin for minimum bias and different collision centralities.

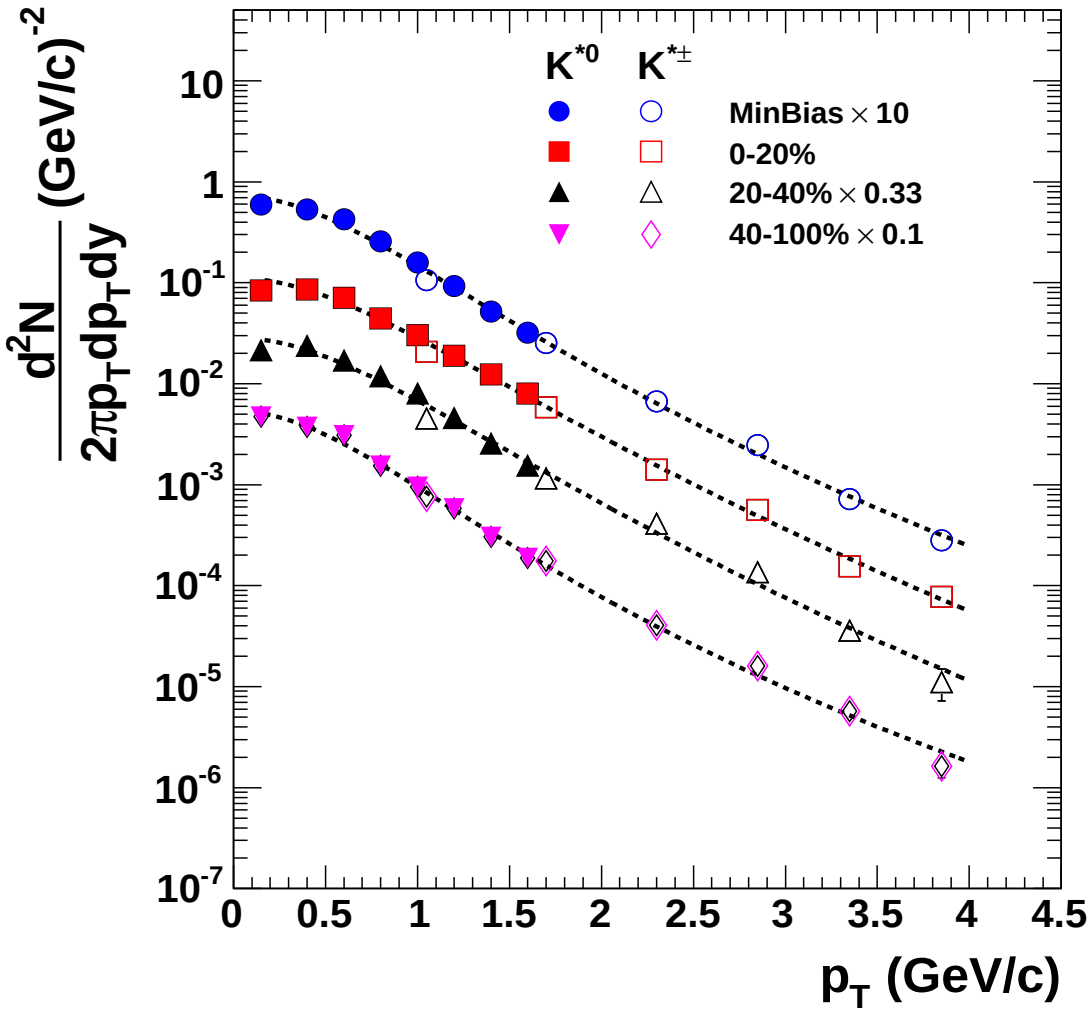

Figure 4.24: The corrected invariant yield for both $(K^{*0}+\overline{K}^{*0})/2$ and $(K^{*+}+K^{*-})/2$ as a function of p_T at $|y| < 0.5$ in $d+Au$ collisions for minimum bias as well as for different centralities. Filled symbols are for neutral K^* and open symbols are for charged K^*. The spectra are fitted with Levy function as defined in eqn. 4.27

Centrality	dN/dy	T (MeV)	n
Minimum bias	0.160 ± 0.002 ± 0.02	256 ± 5 ± 43	9.5 ± 0.6
0-20%	0.296 ± 0.008 ± 0.038	307 ± 18 ± 52	12.5 ± 2.5
20-40%	0.214 ± 0.006 ± 0.028	293 ± 14 ± 49	12.4 ± 2.0
40-100%	0.108 ± 0.002 ± 0.014	238 ± 9 ± 40	8.3 ± 0.7

Table 4.8: The average of K^{*0} and $\overline{K}^{*0}$ and average of K^{*+} and K^{*-} yields at $|y| < 0.5$, the inverse slope parameter T and the exponent n for minimum bias and different collision centralities with their stat. uncertainties and sys. uncertainties.

4.7 Mass and Width Distribution for Δ and K^*

As has been mentioned earlier in Section 4.4, the resonances Δ and K^* produced in the hot and dense nuclear matter, interact with the medium resulting in changes in their mass, width and final yield. These are the so-called $in-medium\ effects$ which come about because of both re-scattering and re-generation. In that connection we have already discussed how to correct the invariant mass distributions including appropriate phase-space correction factors.

In-medium modifications for K^* have been observed in p+p and Au+Au collisions at $\sqrt{s_{NN}}$=200 GeV [66, 98]. Similar effects are also expected to be observed in d+Au collisions at the same energy. The Δ and K^{*0} and $K^{*\pm}$ masses and widths in each p_T bin, measured at mid-rapidity $|y| < 0.5$ have already been presented in Section 4.4 for various centrality bins.

Figure 4.25 shows the p_T dependences of K^* and Δ masses for minimum bias trigger in d+Au collisions. The left panel shows the K^* mass distribution for eight p_T bins for neutral K^* (solid symbols) within $0.0 < p_T < 1.7$ GeV/c and for six p_T bins for charged K^* (open symbols) within $0.7 < p_T < 4.1$ GeV/c. The dashed line and the dotted line represent the standard masses for K^{*0} (896 MeV/c^2) and $K^{*\pm}$ (892 MeV/c^2) respectively, as given in the Particle Data Book [56]. From the figure, we can see that the present reconstructed K^{*0} mass is about 10 MeV/c^2 less compared to the standard value, for $p_T < 0.9$ GeV/c. Above this there is an increase in the mass which reaches the standard value at a p_T value of 1.4 GeV/c. On the other

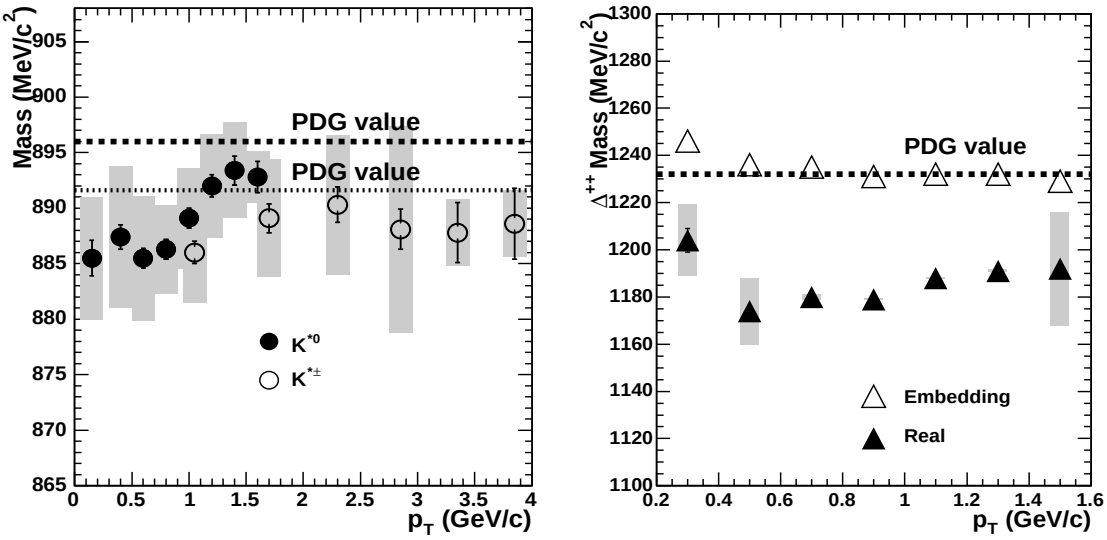

Figure 4.25: (a) Left panel of the figure shows the K^* mass as a function of p_T. The dashed line and the dotted line represent the K^{*0} and $K^{*\pm}$ mass values from Particle Data Book [56]. The solid symbols are for neutral K^* and the open symbols are for charged $K^{*\pm}$ with their stat. uncertainties. (b) Right panel shows the Δ mass from real data (filled symbols) and the Δ mass obtained from the Monte Carlo (MC) simulation (open symbols) as a function of p_T with their statistical uncertainties. The dashed line represents the Δ mass values from Particle Data Book. The shaded region show the systematic uncertainties on the obtained values.

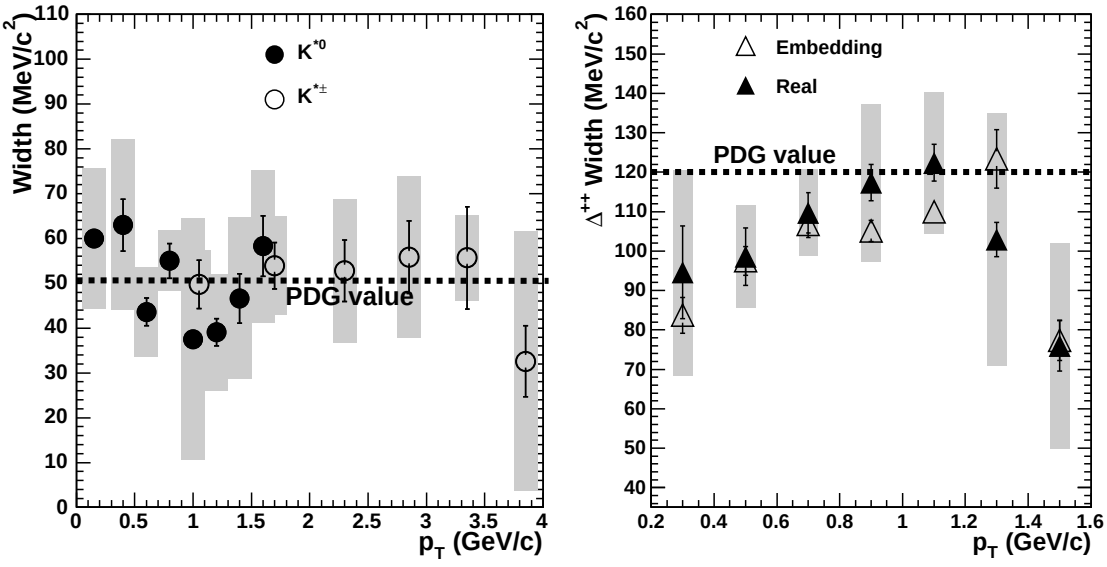

Figure 4.26: (a) Left panel of the figure shows the K^* width as a function of p_T. The dashed line and the dotted line represent the standard K^{*0} and $K^{*\pm}$ width values from Particle Data Book [56]. The solid symbols are for neutral K^* and the open symbols are for charged $K^{*\pm}$. (b) Right panel shows the Δ mass from real data (filled symbols) and the Δ mass obtained from the Monte Carlo (MC) simulation (open symbols) as a function of p_T. The dashed line represents the Δ mass values from Particle Data Book. The errors are statistical. The shaded region show the systematic uncertainties on the measured value.

hand, the charged $K^{*\pm}$ mass doesn't change with respect to p_T, remaining close to the standard value, except at lower p_T (< 1.4 GeV/c) values.

Thus, in both the K^{*0} and $K^{*\pm}$ cases, we observe a shift in mass towards smaller values at low p_T. It looks like, after the production of K^{*0} and $K^{*\pm}$, may be the kaon resonances produced with low p_T spent more time inside the medium, resulting in a modification of their masses. The high p_T particles seems to leave the medium very fast in the process decaying outside the fireball. In such a case there would not be much of a medium induced effect on the mass.

The right panel of the Fig. 4.25 shows the Δ mass distribution for $0.2 < p_T < 1.6$ GeV/c. The dashed line represents the standard mass of 1232 MeV/c^2 [56]. One can see, there is a clear mass shift towards smaller values observed in all the seven p_T bins. On the average this mass reduction is upto about 50 MeV/c^2. In oder to check for the correctness of the calculations, in the same figure we have also shown the results obtained from Monte Carlo (MC) simulations (embedding simulated events in real data) as discussed in Section 4.5. It is important to note that no in-medium effect was considered in constructing the MC generated data. The Δ resonance mass obtained from this is seen to agree with standard values over the entire p_T range considered.

The Δ resonance has a very short life time ($\tau = 1.6 fm/c$). If the lifetime of the fireball source is longer than this, then the decayed daughters of Δ resonance have a chance to re-scatter from other particles present in the medium resulting in a momentum loss. As has been mentioned earlier, there can be re-generation of the resonances through interaction of one of the decay daughters with its pair partner coming from other sources. Such a process has been shown in Fig. 4.4. Because of the momentum loss from re-scattering of a decayed daughter, the reconstructed masses are found to significantly smaller than the standard results. Similar results have also been observed for K^* resonance in Au+Au collisions at $\sqrt{s_{NN}} = 200$ GeV [98].

Figure 4.26 shows the variation of Δ and K^* widths with p_T for minimum bias d+Au collisions at 200 GeV. The left panel shows the K^* width distribution for eight p_T bins for K^{*0} within $0.0 < p_T < 1.7$ GeV/c and for six p_T bins for charged K^*

for $0.7 < p_T < 4.1$ GeV/c. The dashed line represents the standard K^* width of 50 MeV/c^2 [56]. In the figure we don't see any significant difference between the width of K^{*0} and $K^{*\pm}$. The right panel of the Fig. 4.26 shows the Δ width as a function of p_T. The results show an increase in width with increase in p_T, excepting the last point which is expected to be eroneous because of dynamical cut effects. The widths, determined embedding simulated Δ decays in real data (discussed in Section 4.5), have been found to be almost the same as in the real data.

4.8 $\langle p_T \rangle$ Distributions of Δ and K^*

In the hadronic phase between chemical and kinetic freeze-out, the resonances having higher p_T have a greater chance to escape from the hadronic medium and decay outside the fireball source. In such cases there is less probability of daughter particles' re-scattering effects. Thus, high p_T resonances have a greater chance to be detected than the ones with lower p_T [65]. Thus, for resonances we expect a $\langle p_T \rangle$ distribution extending to higher $\langle p_T \rangle$ in heavy ion collisions than in elementary collisions, such as p+p collisions.

The measured transverse momentum spectra for Δ has been fitted with an exponential function shown in Fig. 4.23. From the fitting function we have obtained the Δ yield (dN/dy) and the inverse slope parameter T for minimum bias as well as for three different centralities. Integrating the fitted function within the p_T range from 0.2 -1.6 GeV/c we see that the area covered is $> 86\%$ of the total area under the curve, evaluated taking a p_T range between 0 to infinity. Because of this, a reasonable estimate of the average transverse momentum ($\langle p_T \rangle$) for the Δ can be obtained from the fitted p_T distribution which has a functional form as given in eqn. 4.24. We write,

$$\langle p_T \rangle = \frac{\int_0^\infty p_T^2 exp[-(\sqrt{p_T^2 + m_\Delta^2} - m_\Delta)/T] dp_T}{\int_0^\infty p_T exp[-(\sqrt{p_T^2 + m_\Delta^2} - m_\Delta)/T] dp_T} \tag{4.28}$$

where, m_Δ is the standard Δ mass which is 1232 MeV.

Centrality	$\langle p_T \rangle$ (GeV/c) for Δ	$\langle p_T \rangle$ (GeV/c) for K^*	Δ/p	K^*/K
Min. bias	0.887 ± 0.02 ± 0.142	0.958 ±0.018 ±0.162	0.172 ± 0.005 0.02	0.238 ±0.008 ±0.021
0-20%	0.977 ± 0.05 ± 0.156	1.106 ±0.05 ± 0.188	0.176 ± 0.006 ± 0.018	0.211 ±0.008 ± 0.02
20-40%	0.924 ± 0.04 ± 0.148	1.065 ±0.05 ± 0.181	0.170 ± 0.005 ± 0.018	0.217 ±0.008 ± 0.02
40-100%	0.899 ± 0.03 ± 0.143	0.905 ±0.034 ± 0.154	0.196 ± 0.006 ± 0.021	0.284 ±0.008 ± 0.025

Table 4.9: The $\langle p_T \rangle$values for Δ and K^* and Δ/p and K^*/K ratio for centralities of d+Au collisions with their stat. and sys. uncertainties.

The neutral and charged K^* spectra, for the d+Au collisions, within the p_T range 0.0 to 4.1 GeV/c, have been shown in Fig. 4.24. These p_T spectra have been fitted with Levy functions which, in the given p_T range, have been found to cover $> 96\%$ of the total area under the curve. Therefore, like in the earlier case of the Δ resonance, one can calculate the $\langle p_T \rangle$ for the K^* resonances using eqn. 4.27. One can write

$$\langle p_T \rangle = \frac{\int_0^\infty p_T^2 \frac{1}{1+(\sqrt{m_{K^*}^2+p_T^2}-m_{K^*})} \frac{1}{(nT)^n} dp_T}{\int_0^\infty p_T \frac{1}{1+(\sqrt{m_{K^*}^2+p_T^2}-m_{K^*})} \frac{1}{(nT)^n} dp_T} \tag{4.29}$$

where, m_{K^*} is the standard K^* mass which is 892 MeV.

The $\langle p_T \rangle$ results for Δ and K^*, as calculated using eqn. 4.28 and 4.29 respectively, for various centralities of d+Au collisions, are listed in Table 4.9.

Figure 4.27 shows the $\langle p_T \rangle$ values of Δ and K^* for various centralities (in terms of charged particle multiplicity $dN_{ch}/d\eta$ at mid rapidity) for d+Au collisions. For comparison the $\langle p_T \rangle$ values of π^-, K^- and $\overline{p}$ in p+p, d+Au and Au+Au collisions are also shown in the same figure [66, 118]. From the figure, one can see, the $\langle p_T \rangle$ values for K^* increase with centrality and are relatively higher for d+Au collisions compared to the same for p+p collisions at the same centre of mass energy of 200 GeV. The maximum value of $\langle p_T \rangle$ for K^* obtained for the d+Au collisions at top 20 % centrality is seen to be almost the same as obtained for central Au+Au collisions

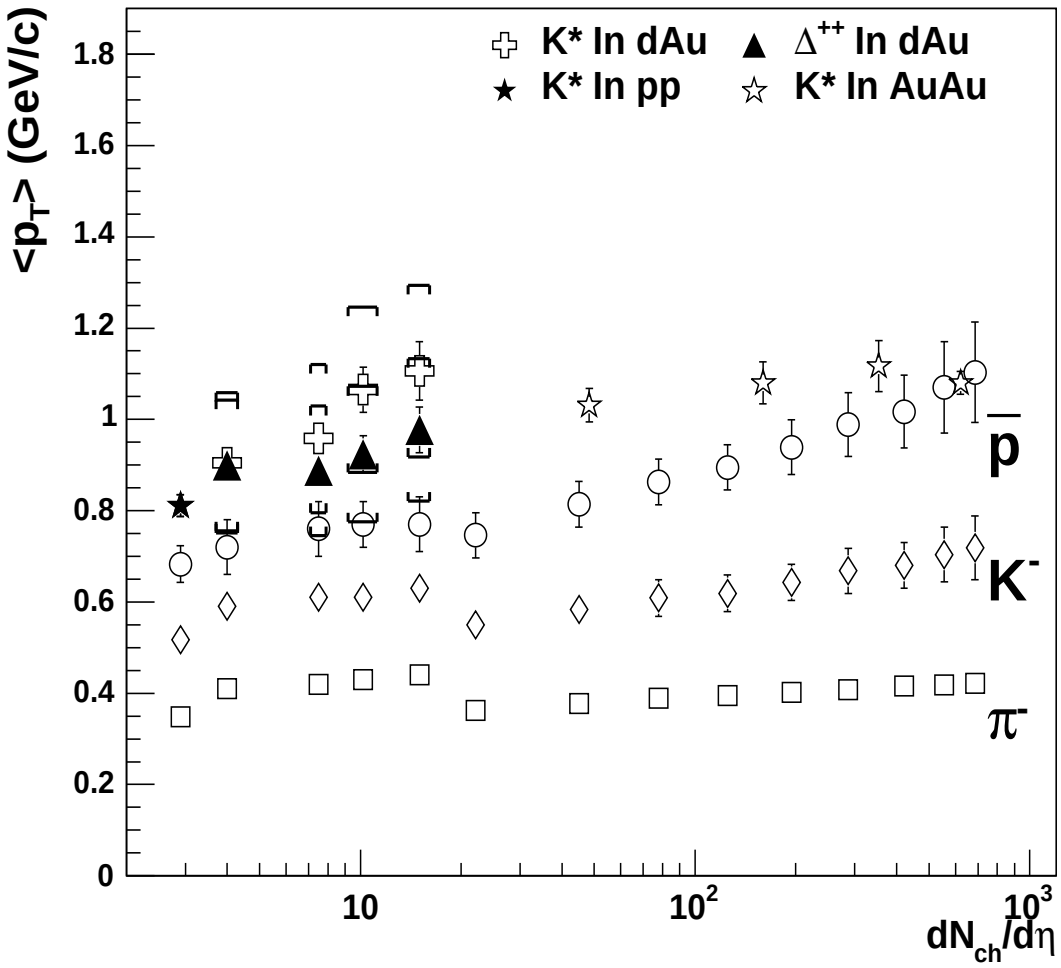

Figure 4.27: The Δ and K^* $\langle p_T \rangle$ as a function of charged hadrons compared to π^-, K^- and $\overline{p}$ in p+p, d+Au and Au+Au collisions.

at the same energy. The Au+Au data do not show any centrality dependence.

For the Δ case we don't have reference point from p+p or Au+Au data to compare with our d+Au results. In the present case (with d+Au) the $\langle p_T \rangle$ values of K^* increase as we go from peripheral to central collisions. Where as we don't see any significant centrality dependence K^* $\langle p_T \rangle$ in Au+Au collisions. For the case of Δ there is a slight increase in $\langle p_T \rangle$ values as we go from peripheral to central collisions. From the ISR data [117], the $\langle p_T \rangle$ values increase with mass of the particles. The K^* $\langle p_T \rangle$ is higher than that of $\overline{p}$ for p+p, d+Au and even in peripheral Au+Au collisions, even though $m_{K^*} < m_{\overline{p}}$. One of the explanation for this result may be that the re-scattering of the daughter particles is the dominant process compared to the K^* re-generation. This is because only the K^* with higher p_T are more likely to decay outside the fireball. Since the higher mass particles are more dominantly produced in the higher multiplicity events, they have higher $\langle p_T \rangle$ values. According to microscopic model predictions, the loss of signal in the low p_T region would result in an increase of the inverse slope parameter (i.e $\langle p_T \rangle$) of the p_T spectra of the resonances. The $\langle p_T \rangle$ of stable particles shows a smooth rise from p+p to most central Au+Au collisions while the resonances show a faster rise from p+p to d+Au and Au+Au reaching a saturation for most central Au+Au collisions.

4.9 Systematic Uncertainties for Yield and Inverse Slope Parameter (or $\langle p_T \rangle$) for Δ and K^*

In order to study the systematic uncertainties on the dN/dy and $\langle p_T \rangle$ of Δ and K^* at mid-rapidity, one needs to consider the systematic errors, which come from different sources. The sources of those errors are: (1) different fitting functions to the invariant mass spectra of Δ and K^*, (2) different fitting function used to fit the p_T spectra, (3) different residual background functions, (4) different freeze-out temperature, (5) different rapidity region considered, (6) different |Z-vertex| cut, and (7) all kinds of

dynamical cuts and detector effects. Some discussions on each of these are given below.

4.9.1 Fit Functions

For extracting the yield of K^* within the p_T range 0.0 to 4.1 GeV/c, the relativistic Breit-Wigner function as shown in eqn.4.17 has been used with minimum bias d+Au events. To get the above base-line results, as mentioned earlier (Section 4.6), the mass parameter has been varied keeping the width fixed . However, one can also try to fit the minimum bias invariant mass spectra for different p_T bins using a simplified Breit-Wigner formula with a linear background as given by

$$f(M) = \frac{a}{2\pi \times 100} \frac{\Gamma_0}{(M - M_0)^2 + \Gamma_0^2/4} + bM + c \tag{4.30}$$

where a is proportional to the K^* yield, M_0 is the mass and Γ_0 is the width of K^*. With this, the K^* yield (dN/dy) and $\langle p_T \rangle$ have been found to change by -10.6% and +6.7% respectively from their baseline values. For the case of Δ this study could not be carried out since the simplified BW function does no fit the invariant mass spectra obtained from data.

4.9.2 Residual Background Functions

For generating the correct invariant mass distribution of the resonances, in each case, a mixed event based combinatorial background was subtracted out of the invariant mass distribution obtained from the same-event (Section 4.4). However, there is still some residual background (RBG) present even after the subtraction of the combinatorial background. For Δ and K^* the RBGs used were a Gaussian and a linear function respectively to get the baseline results. In order to study the systematic uncertainties on the Δ and K^* yields, due to the above background correction, we have used both first order and second order functions for Δ and an exponential and a second order polynomial for K^* to describe the residual background. The first order, second order

and exponential function used are defined as follows:

$$B_1(M) = aM + b \tag{4.31}$$

$$B_2(M) = aM^2 + bM + c \tag{4.32}$$

$$B_3(M) = a \times e^{-b(M-c)} \tag{4.33}$$

Using a linear background, as mentioned above, for the Δ invariant mass spectra, the dN/dy and $\langle p_T \rangle$ have been found to change by -5.6% and +2.8% respectively from the baseline results obtained earlier. The second order polynomial background also resulted in systematic errors of similar order. Unfortunately, for K^* the exponential function did not fit the data. On the other hand use of a second order polynomial background resulted in a change of +5% and +7.9% for dN/dy and $\langle p_T \rangle$ respectively.

4.9.3 Dynamical Cut Effects

There are systematic uncertainties on Δ and K^* results which occur due to various dynamical cuts, like: number of fit points on the TPC tracks, the ratio of number of fit points to the maximum number of possible fit points, DCA cut on detected tracks, acceptance cut based on η-range, track momentum cut based on dE/dx (which contributes to maximally to the total systematic errors under various cut effects).

As discussed in Section 4.2.3, in order to reduce the amount of residual background in the invariant mass distributions, we have used the tighter p (and p_T) cuts for selecting the tracks. For the case of Δ we have selected pion tracks having p (and p_T) 0.1 to 0.6 GeV/c and for proton it is 0.3 to 1.1 GeV/c for an unambiguous determination of particle identity which can be very clearly seen from Fig. 2.6. For the baseline analysis, the minimum number of fit points for pion tracks were 15 the same for proton tracks being 22. Further, all proton and pion tracks with $|\eta| < 0.8$ were selected. For K^*, we had selected kaon tracks having p (and p_T) in the range 0.2 to 0.7 GeV/c and pion tracks with p (and p_T) in the range 0.2 to 10.0 GeV/c with other cuts as presented in Section 4.2.3.

To get an idea about systematic uncertainties due to some relaxation of various cuts, we have opened up the momentum range 0.1 <p (and p_T)< 10 GeV/c for pion and 0.3 <p(and p_T)< 10 GeV/c for proton. Further, tracks with DCA < 1.5 cm were selected. For studying the uncertainties in selecting the momentum cuts we have taken two sets of track momentum cuts. In the first case we take kaons tracks with 0.2 <p (and p_T)< 0.7 GeV/c and pion tracks with 0.2 <p(and p_T)< 0.7 GeV/c for constructing the invariant mass of K^*. In the second case we take kaons tracks with 0.2 <p (and p_T)< 10.0 GeV/c and pion tracks with 0.2 <p (and p_T)< 10.0 GeV/c for the same.

With all the above mentioned (momentum, η, DCA etc) cuts into account, the results on yield (dN/dy) and $\langle p_T \rangle$ were found to change by +7% for both Δ and K^*.

4.9.4 Track Types

For calculating the Δ yields (dN/dy) and $\langle p_T \rangle$ at mid-rapidity for baseline results, we had added both the $p\pi^+$ and $\overline{p}\pi^-$ invariant yields together to increase the statistics. In order to calculate the uncertainties because of this addition, we have now fitted the invariant mass spectra of $p\pi^+$ and $\overline{p}\pi^-$ separately, over all p_T bins and then combine the corrected yields obtained in both cases to calculate (dN/dy) and $\langle p_T \rangle$. The (dN/dy) and $\langle p_T \rangle$ are found to change by -6.3% and -3.9% respectively. Similarly, for the case of K^*, we have fitted the invariant spectra for K^{*0}, $\overline{K^{*0}}$, K^{*+} and K^{*-} separately and then have combined the corrected yields in each p_T bin to calculate (dN/dy) and $\langle p_T \rangle$ for K^* at mid-rapidity. The dN/dy and $\langle p_T \rangle$ values have been found to differ from their baseline values by -1.8% and 0%, respectively.

4.9.5 Detector Effects

The charged tracks measured by the east/west sides of the TPC are defined to have negative/positive rapidity (y) values. In the baseline analysis we had accepted all tracks with $|y| < 0.5$ which means invariant mass spectra were constructed adding

the same obtained from daughter tracks on both sides of TPC. For getting systematic effects, now we consider daughter tracks on each side of TPC and reconstruct the invariant mass spectra for every p_T bin for positive and negative rapidity regions separately. This enables one to evaluate dN/dy and $\langle p_T \rangle$ values for the resonances considered for different rapidity regions. The values obtained are now multiplied by a factor of two to compare with the baseline results. As for results we did not see any difference between the new and baseline results for K^*. However, for Δ, dN/dy and $\langle p_T \rangle$ values for the negative rapidity region are found to differ from the corresponding baseline values by +3% and +1.8% respectively. Where as for the positive rapidity region the corresponding values were -3% and +0.4 % respectively.

In order to achieve roughly uniform acceptance over the pseudorapidity range as defined by $|\eta| < 0.8$, we require the collision vertex to be within |Z-vertex| < 50 cm. However, for K^* we have relaxed this condition to |Z-vertex| < 75 cm to increase the statistics and obtained the baseline results. For studying the effect on Z-vertex shift, for Δ and K^* we have changed Z-vertex cuts to 75 cm and 50 cm respectively. The corresponding dN/dy and $\langle p_T \rangle$ were found to change by -3.7% and -3% respectively for Δ. Similarly, for K^* the above two values are found to change by -0.6% and -3.6% respectively from the baseline results.

4.9.6 Different Freeze-out Parameter

The functions used for fitting the invariant mass spectra for $p\pi$ and $K\pi$ cases corresponding to the Δ and K^* resonances, we have used a value of 160 MeV (in eqns. 4.10 and 4.15) for the freeze-out parameter, (T_{fo}), in the phase-space factor. The effect of this parameter is studied using two values *viz.* 140 MeV and 180 MeV.

Changing T_{fo} to 140 MeV is found to result in -0.3% and +0.4% changes respectively in dN/dy and $\langle p_T \rangle$ values for Δ. A value of 180 MeV for T_{fo} has been found to result in -0.9% and +1.5% changes over the corresponding baseline values. For K^*, a value of 140 MeV for T_{fo}, results in -3.7% and +1.5% change over the baseline values

Different Cuts	dN/dy for Δ	$\langle p_T \rangle$ (GeV/c) for Δ	dN/dy for K^*	$\langle p_T \rangle$ (GeV/c) for K^*
Levy fit	0%	0%	0%	0%
Pow-law fit	+15%	+9.5%	+5%	+5.3%
exponential fit	0%	0%	+4.3%	-10.6%
Boltzmann fit	-1%	-10%	NA	NA
Backgrnd eqn 4.34	-5.6%	+2%	0%	0%
Backgrnd eqn 4.35	-5.6%	+2.8%	+5%	+7.9%
Simplified BW	NA	NA	-10.6%	+6.7%
$T_{fo} = 180$ MeV	-0.9%	+1.5%	+1.2%	+3.6%
$T_{fo} = 140$ MeV	-0.3%	+0.4%	-3.7%	+1.5%
|Z-vertex| < 75 cm	-3.7%	-3%	0%	0%
|Z-vertex| < 50 cm	0%	0%	-0.6%	-3.6%
-0.5$< y <$0.	+3%	+1.8%	NA	NA
0.$< y <$0.5	-3%	0.4%	NA	NA
Track type	-6.3%	-3.9%	-1.8%	0%
Final Sys. Error	±12%	±16%	±13%	±17%

Table 4.10: The systematic uncertainties in percentages for Δ and K^* at midrapidity ($|y| <$0.5) on dN/dy and $\langle p_T \rangle$ in minimum bias $d + Au$ collisions.

of dN/dy and $\langle p_T \rangle$. Taking value of 180 MeV for T_{fo} is found to result in changes of +1.2% and +3.6% respectively in the corresponding values.

4.9.7 Fit Function Used to Fit the p_T Spectra

In order to extract the yield (dN/dy) and the slope parameter (or $\langle p_T \rangle$) for minimum bias and different collision centralities, we have to fit the p_T or m_T spectra with a suitable exponential or power-law or some other function. The low and intermediate p_T region is relatively well described by an exponential function while it fails for the high p_T region where a Levy function is a better choice. Based on this we had carried out our baseline analysis of Δ and K^* using exponential and Levy functions respectively. This has been discussed in Section 4.6. However, to see the differences resulting from different fits, the p_T distribution of Δ (Fig. 4.23) was fitted with a Levy function as given in eqn. 4.27 and a power law as given below.

$$\frac{1}{2\pi p_T}\frac{d^2N}{dydp_T} = \frac{(dN/dy)2(n-1)(n-2)}{\pi\langle p_T\rangle^2(n-3)^2} \times [1 + \frac{p_T}{\langle p_T\rangle(n-3)/2}]^{-n} \quad (4.34)$$

Similarly the minimum bias p_T distribution of K^* (Fig. 4.24) was fitted with an exponential function and a Levy function. The changes over the baseline results on dN/dy and $\langle p_T\rangle$ as obtained with the above fittings are listed in Table 4.10.

4.9.8 Total Systematic Errors

All the systematic uncertainties coming from various sources as discussed in the above sections are listed in Table 4.9. At the bottom of the table we present an estimate of the total systematic errors which in every case has been evaluated in the following manner. All the positive errors and negative errors have been added up separately in the quadrature rule. The larger of the two is what has been presented in the table as the final systematic error.

4.10 Particle Ratios

The measurement of resonance yields with respect to the yields of their corresponding stable particles, such as K^*/K, ρ/π, Δ/p, etc, can give us information about the fireball evolution between chemical and kinetic freeze-out in heavy ion collisions. There are many theoretical predictions regarding whether there exist two freeze-out temperatures or they coincide to one [69, 71, 73].

As we have discussed earlier, resonances can get re-generated in the medium if one daughter particle can combine with another daughter particle coming from a different source. At the same time their number reduces if the daughter particles undergo re-scattering resulting in a change in their momenta. A simple way to look for in-medium effects is to look at the resonance yield to its stable particle yield ratio as a function of centrality. In this case we look at yield ratios like Δ/p and K^*/K. If the ratio is independent of centrality then one can conclude that the re-generation

effect is compensated by re-scattering. A rising trend would mean re-generation effect to be dominant while a decreasing trend with increase in centrality would mean re-scattering to be dominant. Further, individual particle/resonance yields would depend upon their freeze-out temperatures [73] which means particle yield ratios would depend upon the corresponding freeze-out temperatures. The ratio is also expected to depend on whether the freeze-out temperatures for the two species are same or different. If the two freeze-out temperatures are different then kinetic and chemical freeze-out temperatures are different. Therefore it is interesting to study the above mentioned ratio and its variation with centrality in p+p, d+Au and Au+Au collisions.

The yields dN/dy for the stable charged hadrons $\pi^{\pm}$, $K^{\pm}$, p and $\overline{p}$ have been measured for the $d + Au$ collisions at $\sqrt{s_{NN}} = 200$ GeV in the STAR experiment [118]. Using these data on stable hadrons together with the K^* and Δ results from $d+Au$ collisions, we have calculated the ratio of resonance yield to the corresponding yield of $K^{\pm}$ and $(p, \overline{p}\ )$.

Figure 4.28 shows the Δ/p, K^*/K ratio as a function of centrality (defined in terms $dN/d\eta$ of charged hadrons at mid-rapidity) in p+p, d+Au and Au+Au collisions. From the figure we can see that the K^*/K ratios in d+Au and Au+Au collisions are significantly smaller than the same in p+p collisions. The K^*/K ratio suppression may indicate that between the chemical and kinetic freeze-out, K^* signals are predominantly destroyed due to the re-scattering of daughter particles which cannot be compensated by the re-generation effect. The $\pi - \pi$ total interaction cross section, which determines the re-scattering effect is significantly larger than the $K - \pi$ total interaction cross section that decides the re-generation effect. In the case of the Δ resonance, the $p - \pi$ total interaction cross section, which determines the re-generation effect, is comparable to the $\pi - \pi$ total interaction cross section leading to the re-scattering effect. The over all effect is that the observed $(\Delta^{++}+\overline{\Delta}^{--})/(p+\overline{p})$ ratios are flat from peripheral to central $d + Au$ collisions.

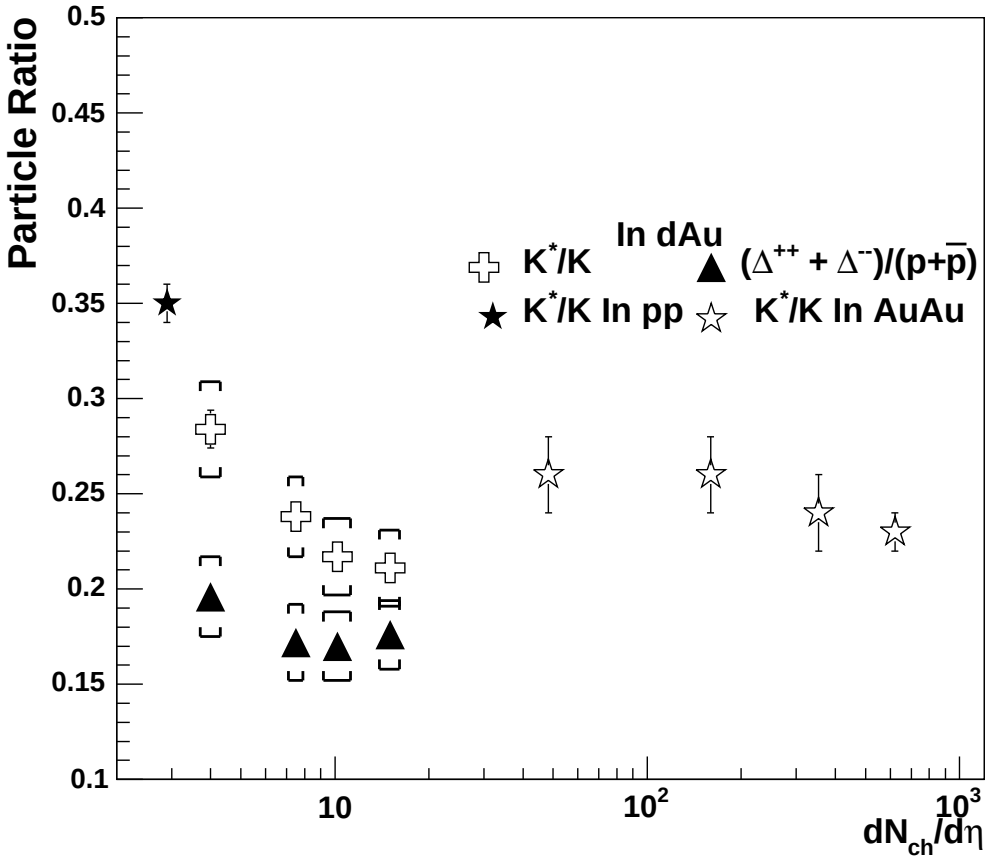

Figure 4.28: The K^*/K and Δ/p ratios as a function of charged hadrons

4.11 Nuclear Modification Factor

In order to study the nuclear modification factor the hadron p_T spectra in the d+Au collision needs to be compared with the same from p+p or $p+\overline{p}$ collisions at the same energy.

The above mentioned nuclear modification factor is defined as

$$R_{dAu}(p_T) = \frac{d^2N^{dAu}/dp_T d\eta}{T_{dAu} d^2\sigma^{NN}/dp_T d\eta} \tag{4.35}$$

where $T_{dAu} = < N_{bin} > /\sigma_{inel}^{NN}$ accounts for the collision geometry, averaged over the event centrality class. $< N_{bin} >$ is the equivalent number of binary NN collisions, which can be calculated using the Glauber model. It is expected that, at low p_T the value of $R_{dAu}(p_T)$ is less than unity. But the yield for hard process scales as $< N_{bin} >$. In the absence of nuclear modification effects $R_{dAu}(p_T) = 1$. The nuclear modification factor can also be also defined as:

$$R_{CP} = \frac{< N_{bin}^{peripheral} > d^2N^{central}/dp_T d\eta}{< N_{bin}^{central} > d^2N^{peripheral}/dp_T d\eta} \tag{4.36}$$

We have measured the Δ invariant yields as a function of p_T for seven p_T bins ($0.2< p_T < 1.6$ GeV/c) and K^* invariant yields for p_T range from 0.0 to 4.1 GeV/c for different centralities of d+Au collisions.

STAR has measured the K^* invariant yields as a function of p_T for minimum bias p+p collisions at 200 GeV. Since the p_T spectra in both d+Au and p+p collisions have the same rapidity and pseudo-rapidity ranges, we can calculate R_{dAu} for K^* from the ratio of the invariant yields in d+Au and p+p collisions. For the case of Δ, we don't have the invariant yield of Δ available for p+p collisions. Therefore, we cannot calculate the R_{dAu} for Δ.

Figure 4.29 shows the nuclear modification factors for Δ and K^*. The upper panel of the figure shows the ratio of central d+Au collision to the p+p collision (R_{dAu}) for K^{*0} and $K^{*\pm}$. The lower panel of the figure shows the central ($(0-20)\%$) to peripheral ($(40-100)\%$) yield ratios for Δ and K^* as a function of p_T. The ratio

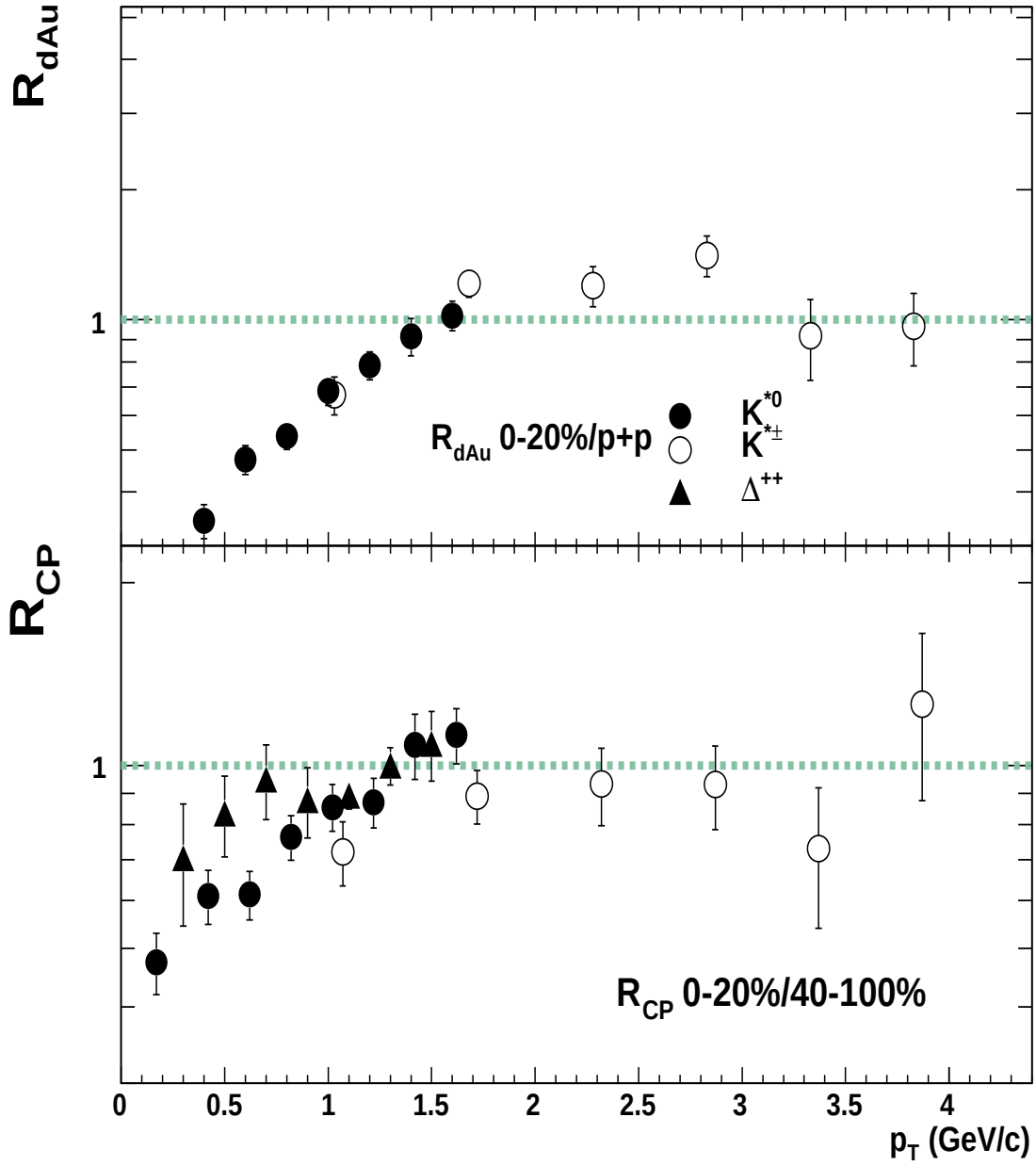

Figure 4.29: The Δ and K^* nuclear modification factor as function of p_T.

R_{CP} for Δ is seen to be lower than unity in the low p_T region. It seems R_{CP} is slightly larger than unity for $p_T > 1$ GeV/c, in line with Cronin effect in the intermediate p_T region [122]. Similarly, for neutral K^* the R_{dAu} and R_{CP} are both seen to increase with finally saturating at a value close to unity for $p_T > 1.4$ GeV/c. The lower value of R_{CP} for $p_T < 1$ GeV/c seems to be a result of re-scattering of daughter particles inside the medium.

Chapter 5

Conclusion

In the present thesis attempts have been made to study the multiplicity of photons and resonance production at RHIC.

The first part is regarding the fabrication and installation of a gas honeycomb proportional counter based preshower PMD for measurement of photon multiplicity, N_γ, and its pseudorapidity distribution in a forward rapidity region at RHIC. This detector was used for the first time to collect data in Run4 during 2003-2004, for Au+Au collisions at $\sqrt{s_{NN}}$=200 GeV. This run was the first RHIC run for the PMD and there were several teething problems with the functioning of the detector associated with the high multiplicity environment at RHIC. As can be seen from the data presented, some of the modules of the PMD were not functioning as well. This put a severe limitation on the present intended work.

The photon data presented in the thesis correspond to 40k "production high" trigger events. At present the results are strictly preliminary in nature without any estimation of the errors. It must be mentioned that in a later run, PMD took data on Au+Au at $\sqrt{s_{NN}}$=62.4 GeV. In that run the detector functioned rather well reporting N_γ for the first time with relatively better photon counting efficiency and better purity of photon sample. However, the estimated errors on the data are $\sim$ 14%. Based on this it is presumed that present errors could be as high as 20 %.

The pseudorapidity distribution, $dN_\gamma/d\eta$, within an η range from 2.3-3.8, seem to be in reasonable agreement with PHOBOS data on charged particles. This is really not surprising since the number of charged particles, N_{ch}, is almost the same as the number of charged pions which is twice that of neutral pions. Since each neutral pions decay leading to the production of two photons, the measured N_γ and N_{ch} distributions, over the same η coverage resemble each other.

The second part of the thesis revolves around the production of $\Delta(1232)$, $K^{*0}(896)$ and $K^{*\pm}(892)$ resonances in d+Au collision at $\sqrt{s_{NN}}$=200 GeV via their hadronic decay channels: $\Delta \rightarrow p\pi$, $K^{*0} \rightarrow K\pi$ and $K^{*\pm} \rightarrow K^0_s\pi^\pm$. The Δ^{++} and $K^{*0}, K^{*\pm}$ masses and widths have been studied as a function of p_T. The Δ^{++} and $K^{*0}, K^{*\pm}$ transverse momentum spectra have been studied for different centrality bins. The mid-rapidity yields, dN/dy, and the inverse slope parameters, which correspond to the effective temperatures, T, have been extracted through exponential fits to the Δ p_T-spectra and a Levy fits to the $K^{*0}, K^{*\pm}$ p_T-spectra. The particle ratios, Δ/p and K^*/K and the mean transverse momenta, $\langle p_T \rangle$, for both Δ and K^* have also been studied for different centrality bins. Effect of the nuclear modification factor, R_{dAu} has been studied for K^* as a function of p_T, by comparing the K^* yield in top 20% of d+Au and p+p collisions. In case of Δ, we could not look at R_{dAu} because of unavailability of p+p results. The same effect defined in terms of the central to peripheral yield ratio, R_{CP}, has also been studied for both Δ and K^* resonances as functions of p_T.

A significant downward shift in Δ^{++} mass $\sim$50 MeV, has been observed over a p_T range from 0.2-1.6 GeV/c. For the case of K^*, for p_T <0.9 GeV/c, there is also a downward mass shift of about 10 MeV. This agrees with the fact that resonances, with extremely short life times in a hot and dense medium, can interact with the surrounding hadrons resulting in observable effects such as changes in mass and width. The observed K^*/K ratio in d+Au collisions have also been found to be significantly smaller than that for p+p collisions. Between the chemical and the kinetic freeze-out stages, the daughter particles produced from K^* decay scatter off hadrons resulting

in a suppression in the primordial K^* yield. This re-scattering effect is p_T dependent. The K^*s produced with a higher p_T (> 1.2 MeV/c), have a greater chance to escape from any re-scattering in the medium. We do not see any mass shift in such a case. The fact that $< p_T >$ for K^* in d+Au collisions is much higher than the same as obtained from p+p collisions goes in agreement with the p_T dependence of daughter particles' re-scattering effect. On the other hand the Δ/p ratio has been found to be almost the same for all centrality classes considered which seems to suggest that the regeneration of Δ is comparable with the re-scattering of decay daughters resulting in a loss in Δ yield.

For both the resonances considered, results also indicate there is greater production of high p_T particles in central collisions than in peripheral collisions. In the low p_T region, relatively less high p_T particles are produced. This results in an observable increase in R_{CP} or R_{dAu} towards unity in the low p_T region. For $p_T >\sim 1.4$ GeV/c there is a saturation with the ratio remaining at unity.

Bibliography

[1] D. J. Gross and F. Wilczek, Phys. Rev. Lett. **30**, 1343 (1973); H. Politzer, Phys. Rev. Lett. **30,** 1346 (1973).

[2] Cheuk-Yin Wong, Introduction to High-Energy Heavy-Ion Collisions.

[3] J. Harris, three lectures given at the Lake Louise Winter Institute on Quantum Chromodynamics, 15-21 February, 1998, Lake Louise, Alberta, Canada, published in World Scientific, 1998.

[4] Technical Status Report Compressed Baryonic Matter (CBM) experiment.

[5] P. Braun-Munzinger, Nucl. Phys. A **681**, 119-123 (2001).

[6] J. D. Bjorken, Phys. Rev. D **27**, 140-151 (1983).

[7] R. J. Glauber, in Lectures in Theoretical Physics, edited by W. E. Brittin and L. G. Dunham (Interscience, N.Y., 1959), Vol. 1, p. 315.

[8] D. H. Rischke, Nucl. Phys. A **698**, 153-163 (2002).

[9] L. van Hove, Phys. Lett. B **118**, 138 (1982).

[10] L. D. Landau, Izv. Akad. Nauk SSSR Ser. Fiz. **17**, (1953) 51; Collected papers, Ed. D. Ter Haar (pergamon, Oxford, 1965) p.569.

[11] A. Bialas, M. Bleszynski and W. Czyz, Nucl. Phys. **B111**, 461 (1976).

[12] D. Kharzeev and M. Nardi, Phys. Lett. **B507**, 121 (2001).

[13] A. Poskanzer and S. Voloshin, Phys. Rev. C **58**, 1672 (1998).

[14] Introduction to Relativistic Heavy Ion Collisions, L. P. Csernai.

[15] N.S. Amelin, E. F. Staubo, L. P. Csernai, V. D. Toneev, K. K. Gudima and D. Strottman, Phys. Rev. Lett, **67**, 1523 (1992).

[16] L. P. Csernai and J. I. Kapusta, Phys. Rev. Lett, **69**, 737 (1992).

[17] STAR Collaboration, C. Adler *et al.*, Phys. Rev. Lett. **90**, 032301 (2003).

[18] STAR Collaboration, J. Adams *et al.*, Phys. Rev. Lett. **92**, 052302 (2004).

[19] PHENIX Collaboration, S.S. Adler *et al*, Phys. Rev. Lett, **94**, 082302 (2005).

[20] M. Gyulassy, I. Vitev and X-N Wand, Phys. Rev. Lett. **86**, 2537 (2001).

[21] P. Huovinen, P. F. Kolb, . W. Heinz, P. V. Ruuskanen, and S. A. Voloshin, Phys. Lett. B **503**, 58 (2001).

[22] D. Molnar and M. Gyulassy, Nucl. Phys. A **697**, 495 (2002).

[23] J. Rafelski, Phys. Rept. **88**, 331 (1982).

[24] P. Koch, B. Muller and J. Rafelski, Phys. Rept. **142**, 167 (1986).

[25] STAR Collaboration, C. Adler *et al.*, Phys. Lett. B **595**, 143 (2004).

[26] M. M. Aggarwal *et al.*, Phys. Rev. Lett. **85**, 3595 (2000).

[27] D. K. Srivastava, B. Sinha, M. Gyulassy and X. N. Wang, Phys. Lett. **B 276**, 285, (1992).

[28] S. Chakrabarty *et al.*, Phys. Rev. **D 46**, 3802(19192).

[29] G. Domokos and J. I. Goldman, Phys. Rev. **D 23**, 203 (1985).

[30] T. Matsui and H. Satz, Phys. Lett. **B 178**, 416 (1986).

[31] M. Gonin *et al.*, Nucl. Phys. **A 610**, 404c (1996).

[32] M.C. Abreu *et al.*, Nucl. Phys. **A 661**, 93 (1999).

[33] M.C. Abreu *et al.*, Phys. Lett. **B 477**, 28 (2000).

[34] A. Capella, E.G. Ferreiro, and A. B/ Kaidalov, Phys. Rev. Lett.**85**, 2080 (2000).

[35] NA50 Collaboration, H. Santosh *et. al*, hep-ex/0306004.

[36] L. Gerland *et al.*, J. Phys. **G27**, 695 (2001).

[37] J-P Blaizot *et at.*, Phys. Rev. Lett. **85**, 4012 (2000).

[38] X-N. Wang and M. Gyulassy, Phys. Rev. Lett. **68**, 1480 (1992).

[39] M. Gyulassy and M. Plumer, Phys. Lett. **B 243**, 432 (1990).

[40] M. gyulassy and X-N. Wang, Nucl. Phys. **A 590**, 511C (1995).

[41] M. Gyulassy, Nucl. Phys. **B571**, 197 (2000).

[42] M. Gyulassy, Nucl. Phys. **A661**, 637 (1999).

[43] C. Adler *et al.*, Phys. Rev. Lett. **89**, 202301 (2002).

[44] J.P. Blaizot and A. Krzywcki, Phys. Rev. **D46**, 246 (1992).

[45] K.Rajgopal and F. Wilczek, Nucl. Phys. **B399**, 395 (1993).

[46] M. Asakawa, Z. Huang and X-N. Wang, Phys. Rev. Lett. **74**, 3126, (1995).

[47] A.A. Anselm, M.G. Ryskin, Phys. Lett. **B266**, 482 (1991).

[48] C.M.G. Lates, Y. Fujimoto and S. Hasegawa, Phys. Rep. **65**, 151 (1980).

[49] MiniMax Collab., T.C. Brroks *et al.*, Phys. Rev **D61**, 032003 (2000).

[50] WA98 Collab., M.M. Aggarwal *et al.*, Phys. Rev. **C64**, 011901 (2001).

[51] David Park, *Introduction to the Quantum Theory*, Second edition (1974).

[52] J.W.Harris, C.Beckmann, J. Gans and K.H. Gulbrandsen, RHIC physics overview, AIP Conference Proceedings Vol. **631**, 533 (2002).

[53] L. W. Alvarez, Nobel Lecture, December 11, 1968.

[54] Donald H. Perkins, Introduction to High Energy Physics, Third Edition,1987.

[55] D.E. Groom *et. al.*, Eur. Phys. J. **C15**, 1 (2000).

[56] Particle Data Group, Eur. Phys. J **C3**, 1-794 (1998).

[57] R. Rapp, Phys. Rev. **C 63**, 054907 (2001).

[58] R. Rapp, G. Chanfray and J. Wambach, Nucl. Phys. **A617**, 472 (1997).

[59] T. Ullrich *et al.*, Nucl. Phys. **A610**, 317c (1996).

[60] A. Drees, Nucl. Phys. **A610**, 536c (1996).

[61] Zhangbu Xu, nucl-ex/0307014.

[62] E.V. Shuryak, G.E. Brown, *Nucl.Phys.* **A 715**, 462c (2003).

[63] P. F. Kolb and M. Prakash, Phys. Rev. **C67**, 044902 (2003).

[64] R.S. Longacrre, nucl-th/0303068.

[65] M. Bleicher, J. Aichelin, Phys. Lett. **B530**, 81 (2002).

[66] STAR Collaboration, C. Adler *et al.*, Phys. Rev. **C71**, 064902 (2005).

[67] R. Rapp and J. Wambach, Adv. Nucl. Phys. **25**, 1 (2000).

[68] E.V. Shuryak and G.E. Brown, *Nucle.Phys.* **A717**, 322 (2003).

[69] G. Torrieri and J. Rafelski, Phys. Lett. **B509**, 239 (2001).

[70] W. Broniowski and W. Florkowski, Phys. Rev. Lett. **87**, 272302 (2001).

[71] M. Bleicher, J. Aichelin, hep-ph/0201123., G. Torrieri and J. Rafelski, hep-ph/0112195.

[72] U.W. Hienz, Nucl.Phys. **A661**, 140-149 (1999).

[73] W. Florkowski and W. Broniowski, nucl-th/0212052.

[74] K. Werner, Phys. Rep. C **232**, 87 (1993).

[75] M. Gyulassy and X. N. Wang, Comput. Phys. Commun. **83**, 307 (1994).

[76] B. Anderson *etal*. Phys. Rep. **97**, 13 (1983).

[77] C. Adler, Phy. Rev. **C66**, 061901(R) (2002).

[78] W. Broniowski, A. Baran and W. Florkowski, Acta. Phys. Polon. **B33**, 4235 (2002).

[79] Braun-Munzinger, P. Magestro, D. Relich and J. Stachel, Phys. Lett. **B518**, 41 (2001).

[80] *Introduction on RHIC at* "http://www.bnl.gov/RHIC", "http://www.bnl.gov/rhic/experiments.htm"

[81] STAR Collaboration (K.H. Ackermann et al.) Nucl.Instrum.Meth. **A499**, 624 (2003).

[82] 'Conceptual Design Report for the Solenoidal Tracker At RHIC', The STAR Collaboration, PUB-5347 (1992); J. W. Harris *et.al.*, Nucl. Phys. **A 566**, 277c (1994).

[83] R. L. Brown *et.al.*, Proc. 1997 IEEE Particle Accelerator Conf., 3230 (1998) *and* F. Bergsma *et.al.*, Nucl.Instrum.Meth.**A 499**, 633-639 (2003).

[84] M. Anderson *et.al.*, Nucl.Instrum.Meth.**A 499**, 659-678 (2003).

[85] R. Bellwied *et.al.*, Nucl.Instrum.Meth.**A 499**, 640-651 (2003).

[86] K. H. Ackermann *et.al* Nucl.Instrum.Meth.**A 499**, 713-719 (2003).

[87] 'A Ring Imaging Cherenkov Detector for STAR', STARnote 349, STAR/ALICE RICH Collaboration.

[88] A. Braem *et.al*, Nucl. Instrum. Meth.**A 499**, 720 (2003).

[89] W.J.Llope *et.al.*, Nucl.Instrum.Meth.**A 522**, 252 (2004).

[90] B. Bonner *et.al.*, Nucl.Instrum.Meth.**A 508**, 181-184 (2003).

[91] M. Beddo *et.al.*, Nucl.Instrum.Meth.**A 499**, 725-739 (2003).

[92] C. E. Allgower *et.al.*, Nucl.Instrum.Meth.**A 499**, 740-750 (2003).

[93] M. M. Aggarwal *et.al.* Nucl.Instrum.Meth.**A 499**, 751-761 (2003).

[94] L. Kotchenda *et.al.* Nucl.Instrum.Meth.**A 499**,703-712 (2003).

[95] . M. Landgraf *et.al.* Nucl.Instrum.Meth.**A 499**, 762-765, (2003) and A. Ljubicic *et.al.*, IEEE Trans. Nucl. Sci. **47**, 99 (2000).

[96] F. S. Bieser *et.al.* Nucl.Instrum.Meth.**A 499**, 766-777 (2003).

[97] C. Adler *et.al.* Nucl.Instrum.Meth.**A 499**,778-791 (2003) and J.S. Lange *et.al.*, IEEE Trans. Nucl. Sci. **48**, 3 (2000).

[98] H. Zhang, Ph.D. thesis, Yale University, 2003.

[99] H. Bichsel, "Enegry loss in thin layer of argon", STAR note 418.

[100] L. Arnord *et.al.* Nucl.Instrum.Meth.**A 499**, 652-658 (2003).

[101] *STAR SSD − Technical Info, General Overview*, "http://star.in2p3.fr/STAR/technique2.html Overview".

[102] *Proposal to Install a Forward Pion Detector in STAR*, "http://www.star.bnl.gov/STAR/html/fpdl/index.html"

[103] Photon Multiplicity Detector Techinical Design Report (2000).

[104] M. M. Aggarwal *et.al.*, WA93 collaboration, NIM **A 372**, 143 (1996).

[105] M. M. Aggarwal *et.al.*, WA93 collaboration, NIM **A 421**, 558 (1999).

[106] Anand. K. Dubey, Ph.D Thesis, Utkal University, 2003.

[107] ALICE HMPID Technical Design Report, CERN/LHCC98-19 (1998).

[108] PHOBOS collaboration, B. B. Back *et.al.*, Phys. Rev. Lett. **91**, 052303 (2003).

[109] STAR Collaboration, J. Adams *et.al.*, Phys. Rev. Lett. **91**, 072304 (2003).

[110] R. Arndt *etal.*, Phys. Rev. D **32**, 1085 (1985).

[111] R. Brun *etal.*, GEANT3 user's guide, CERN/DD/EE/84-1 (1984).

[112] J. Hamilton, Pion-Nucleon scattering in High Energy Physics, Vol. I, p.193, ed. E. Burhop, (Academic Press,1967).

[113] W. Broniowski *et.al*, Phys.Rev.C **68**, 034911 (2003).

[114] G. Wilk and Z. Wlodarczyk, Phys. Rev. Lett. **84**, 2270 (2000).

[115] S. A. Bass *et.al.* Phys. Lett. B **335**, 289 (1994).

[116] W. Ehehalt *et.al.* Phys. Rev. C **47**, R2467 (1993).

[117] M. Bourquin and J.-M. Gaillard, Nucl. Phys. B **114**, 334 (1974).

[118] STAR Collaboration, J. Adams *et al.*, Phys. Lett. **B 616**, 8 (2005).

[119] J. Cleymans *et. al* J.Phys.G **25**, 281-285 (1999).

[120] M. Bleicher and H. Stocker, J. Phys. G **30**, 111 (2004).

[121] D. Kharzeev *et. al.* Phys. Lett. B **561**, 93 (2003); J.L. Albacete *et. al.*, Phys. Rev. Lett. **92**, 082001 (2004); R. Baier *et. al.*, Phys. Rev. D **68**, 054009 (2003).

[122] D. Kharzeev *etal.*, Phys. Lett. B**561**, 93 (2003); J. L. Albacete *etal.*, Phys. Rev. Lett. **92**, 082001 (2004); D. Kharzeev *etal.*, Phys. Rev. D **68**, 094013 (2003); R. Baier *etal.*, Phys. Rev. D **68**, 054009 (2003).